# NOTICE

# AVIS

The quality of this microform is heavily dependent upon the quality of the original thesis submitted for microfilming. Every effort has been made to ensure the highest quality of reproduction possible.

If pages are missing, contact the university which granted the degree.

Some pages may have indistinct print especially if the original pages were typed with a poor typewriter ribbon or if the university sent us an inferior photocopy.

La qualité de cette microforme dépend grandement de la qualité de la thèse soumise au microfilmage. Nous avons tout fait pour assurer une qualité supérieure de reproduction.

S'il manque des pages, veuillez communiquer avec l'université qui a conféré le grade.

La qualité d'impression de certaines pages peut laisser à désirer, surtout si les pages originales ont été dactylographiées à l'aide d'un ruban usé ou si l'université nous a fait parvenir une photocopie de qualité inférieure.

Canada

UNIVERSITY OF ALBERTA

# AN OPTOELECTRONIC MIXER FOR FIBER-RADIO MICROCELL SYSTEMS

BY

## RAJENDRA PRASAD KODAYPAK  ©

A thesis submitted to the Faculty of Graduate Studies and Research in partial fulfillment of the requirements for the degree of **MASTER OF SCIENCE.**

DEPARTMENT OF ELECTRICAL ENGINEERING

EDMONTON, ALBERTA

SPRING 1996

The author has granted an irrevocable non-exclusive licence allowing the National Library of Canada to reproduce, loan, distribute or sell copies of his/her thesis by any means and in any form or format, making this thesis available to interested persons.

L'auteur a accordé une licence irrévocable et non exclusive permettant à la Bibliothèque nationale du Canada de reproduire, prêter, distribuer ou vendre des copies de sa thèse de quelque manière et sous quelque forme que ce soit pour mettre des exemplaires de cette thèse à la disposition des personnes intéressées.

The author retains ownership of the copyright in his/her thesis. Neither the thesis nor substantial extracts from it may be printed or otherwise reproduced without his/her permission.

L'auteur conserve la propriété du droit d'auteur qui protège sa thèse. Ni la thèse ni des extraits substantiels de celle-ci ne doivent être imprimés ou autrement reproduits sans son autorisation.

Canada

UNIVERSITY OF ALBERTA

LIBRARY RELEASE FORM

NAME OF AUTHOR: **RAJENDRA PRASAD KODAYPAK**

TITLE OF THESIS: **AN OPTOELECTRONIC MIXER FOR FIBER-RADIO MICROCELL SYSTEMS**

DEGREE: **MASTER OF SCIENCE**

YEAR THIS DEGREE GRANTED: **1996**

RAJENDRA PRASAD KODAYPAK
544 L.I.G.H, K.P.H.B COLONY
HYDERABAD-500872
INDIA
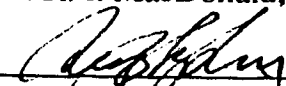
DATE: 30 January 1996

UNIVERSITY OF ALBERTA
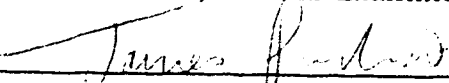
FACULTY OF GRADUATE STUDIES AND RESEARCH

The undersigned certify that they have read, and recommended to the Faculty of Graduate Studies and Research for acceptance, a thesis entitled **AN OPTOELECTRONIC MIXER FOR FIBER-RADIO MICROCELL SYSTEMS** submitted by **RAJENDRA PRASAD KODAYPAK** in partial fulfilment of the requirements for the degree of **MASTER OF SCIENCE.**

Dr. R. I. MacDonald, Supervisor

Dr. Q. Z. Liu, Co-Supervisor

Dr. P. A. Goud, Internal Examiner

Dr. J. Pinfold, External Examiner

DATE: 29 January 1996

# ABSTRACT

Microcellular radio communication systems based on optical fiber feeders provide flexible telephony services for futuristic wireless personal communications. They may offer the benefit of concentrating expensive RF components at a central station and delivering RF signals to inexpensive multiple remote antennas. The difficulty of generating and transmitting high frequency optical signals is overcome in this work by optoelectronic mixing (OEM). By using simple diode based GaAs metal-semiconductor-metal photodetector (MSM-PD) as an OEM, the incoming optical information signal from the central station is directly upconverted to the desired electrical frequency at the remote radio base station.

The high-speed properties of the MSM-PD were studied and found to have a wide bandwidth of about 3 GHz which facilitated mixing in the high frequency region. The detector was also characterized in terms of its dc responsivity and an analytical function was obtained to further analyse the OEM properties in terms of its conversion loss and noise figure. Based on analytical expressions, the optical link quality was estimated in terms of the carrier-to-noise ratio, which was found to be limited by the laser diode in a multichannel system. Theoretical analysis was well supported by experimental results based on single channel and subcarrier multiplexed transmission.

Finally, the OEM performance was tested in a hybrid fiber-radio link which was used to transport low bit rate digital signals using $\pi/4$-DQPSK modulation. The measured signal constellations in the back-to-back and RF channel configurations gave satisfactory results indicating that the link linearity was transparent to the integrated optoelectronic devices. Thus the OEM may find interesting applications in hybrid fiber-radio microcell systems.

# ACKNOWLEDGEMENTS

# Table of Contents

# List of Tables

# List of Figures

# Glossary

| | |
|---|---|
| AlGaAs | Aluminium Gallium Arsenide |
| AFG | Arbitrary Function Generator |
| ARU | Antenna Remote Unit |
| B | Bandwidth |
| BER | Bit Error Rate |
| BS | Base Station |
| CIR | Carrier to Intermodulation noise Ratio |
| CL | Conversion Loss |
| CNR | Carrier to Noise Ratio |
| CS | Central Station |
| EOM | External Optical Modulator |
| FO | Fiber Optic |
| GaAs | Gallium Arsenide |
| HBT | Heterojunction Bipolar Transistor |
| HEMT | High Electron Mobility Transistor |
| HIC | Hybrid Integrated Circuit |
| IF | Intermediate Frequency |
| IMD | Intermodulation Distortion |
| IRIS | Impulse Response Identification System |
| LED | Light Emitting Diode |
| LD | Laser Diode |
| LO | Local Oscillator |

| | |
|---|---|
| MESFET | Metal Semiconductor Field Effect Transistor |
| MMIC | Monolithic Millimeter-wave Integrated Circuits |
| MMW | Millimeter wave |
| MS | Mobile Station |
| MSM-PD | Metal Semiconductor Metal Photodetector |
| NF | Noise Figure |
| OEIC | Opto Electronic Integrated Circuit |
| OEM | Opto Electronic Mixer |
| OMI | Optical Modulation Index |
| PCD | Photo Conductor |
| $\pi/4$-DQPSK | $\pi/4$ shifted Differentially Encoded Quadrature Phase Shift Keying |
| PRBS | Pseudo Random Binary Sequence |
| PS | Personal Station |
| RF | Radio Frequency |
| RIN | Relative Intensity Noise |
| SBD | Schottky Barrier Diode |
| SCM | Sub Carrier Multiplexing |
| WDM | Wavelength Division Multiplexing |

# List of Symbols

$f_1, f_2$ — Subcarrier frequencies

$f_{LO}$ — LO frequency

$I_o$ — Laser dc bias current

$I_{th}$ — Laser threshold current

$m$ — Optical modulation index

$P$ — LD Optical power

$P_{in}$ — RF input power

$R_{ld}$ — Laser diode input impedance

$P_f$ — Average received optical power

$R$ — MSM-PD responsivity

$R_{Vdc}$ — DC responsivity

$V_{dc}$ — DC bias voltage

$V_{lo}$ — LO voltage

$R_b$ — MSM-PD bias resistance

$IM_3$ — LD third-order intermodulation distortion

# 1. INTRODUCTION

Fiber based microcellular communication systems have experienced a tremendous growth in the past few years. Such systems exploit the advantages of both microwave/millimeter-waves and optical fibers to service personal communication terminals.

## 1.1 Cellular radio systems

Cellular systems are very high capacity communication systems. In order to meet the demands of an ever increasing number of subscribers, microcellular or picocellular network architectures have been proposed [1].The cell size in these systems lies within about 300 meters diameter communication range. The reduced cells (microcells) are provided with antenna remote units (ARUs) connected to a central cellular base station (BS) as shown in Fig. 1.1(a). For the indoor office environment, the cell size is determined by floor or office separations and, when the antenna separation is less than 10-20 meters, the cells can be termed "picocells" [2]. A macrocell constitutes the union of micro/pico-cells. Spectrum reuse can be employed more extensively in a given area when the cell size is small. Microcells can also eliminate antenna dead zones which are encountered in macrocell systems. This is not only because of the smaller and more focused coverage area, but also because of the reduced antenna height which results in lower power consumption in an ARU than that in a conventional base station. Though this approach can be used to accommodate more users within a given spectrum allocation, significantly more ARUs are required and thus the access of cell-site space becomes a serious problem.

1
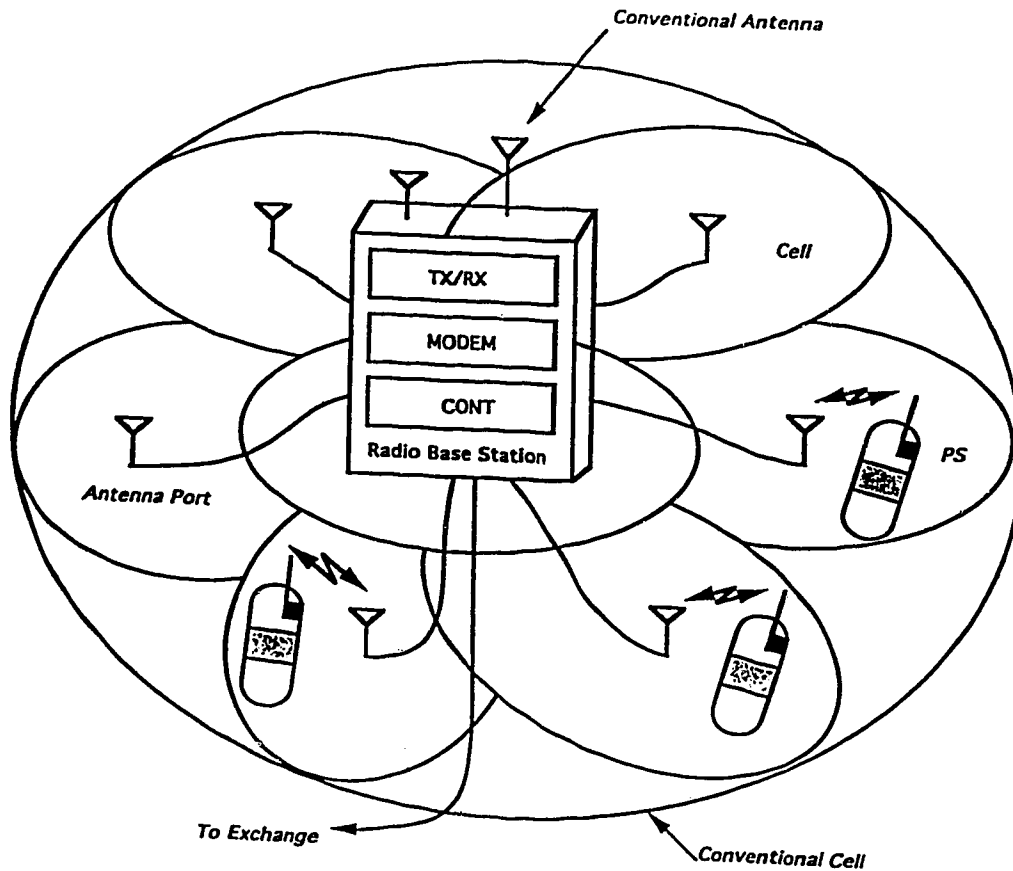
**Fig. 1.1(a) Central radio base station with extended antennas**

Subcarrier multiplexing (SCM) signals over optical fibers is very attractive and finds wide spread applications in signal distribution because of its simplicity and cost-effectiveness [3]. SCM is based on the principle of direct intensity modulation of an E/O device (a laser diode or an external modulator) at the wireless system carrier frequencies as shown in Fig. 1.1(b). Thus the multiplexed radio subcarriers can be simultaneously transmitted along the optical fiber. At the receiver side, a photodiode in the receiver converts the received optical power into electric power with a linear response. The desired channel is selected by an electric mixer after photodetection for further amplification and signal processing.

2
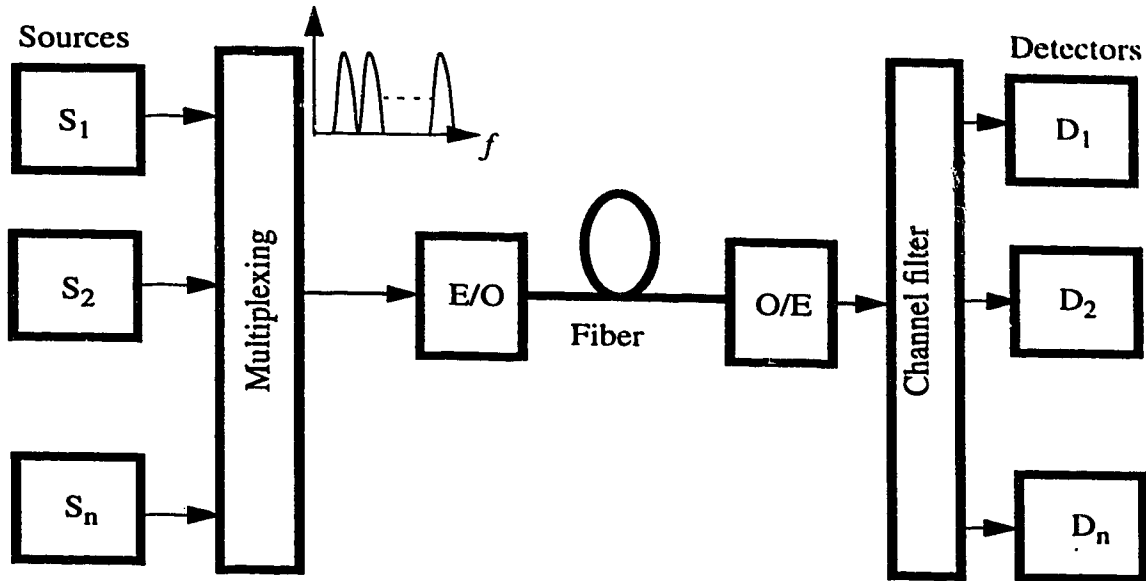
**Fig. 1.1(b) Fiber-radio SCM transmission**

## 1.2 Fiber-Radio Technology

With the reduced cell size in a micro/pico-cellular environment, a large number of remote radio-base stations (Micro-BSs) are required for effective signal distribution in a given area. Therefore, it is important to develop cost-effective techniques for the minimization of BS hardware and the signal distribution paths which will feed into them. The radio transmission performance between the ARU and the portable handset, which depends upon the ARU location, has to be taken into consideration. Though the radio signals from the Micro-BS to the antenna port can be delivered by various transmission media including coaxial, waveguide, and free space, fiber optic signal feeds have become promising because of their low loss, wider frequency response, and ease of installation.

The optical fiber feeder can drastically reduce the cost and size of the Micro-BSs. By using

3

the optical feeder, very compact Micro-BSs is possible, since it is basically mere opto/electronic converters. Furthermore, various radio channel controls such as hand-off control, macro-diversity or dynamic channel assignment can be done at the central-BS. In addition, the microcellular system with the optical feeder is highly flexible for changes in modulation schemes or carrier frequency assignments for individual cells, as the feeder is transparent for all radio signals.

In order to save the cell site space, hybrid fiber radio systems based on SCM and the associated technologies have been studied [4]. Fiber optic microwave subcarrier transmission links have received wide attention since they may be capable of effectively using the millimeter-wave (mm-wave) band, both for wideband personal radio communications and for broad-band local access. With improvements in device technologies, realization of compact and economical RF system designs is made possible by interconnecting various microwave and optical devices, circuits and subsystems with optical fibers.

Fig. 1.2 shows the schematic of a more general optical fiber feeder based microcellular system. In the uplink configuration, the radio signal received at the Micro-BS is converted into an optical signal and transmitted back to the central-BS through the optical fiber. In a similar way, the radio signal is transmitted from the Central-BS to the Micro-BS in the downlink for radiation.

For mobile radio applications, the radio signal power received at the Micro-BS fluctuates greatly, due to fading, shadowing or changes in distance between the Micro-BS and the mobile station (MS). Therefore, the optical feeder that links the Micro-BSs to the Central-BS requires high dynamic range, very low noise and distortion characteristics to cover the

4

Central-BS

Micro-BS

MOD
MOD
MOD

Transcoder

E/O

DEM
DEM
DEM

O/E

S/N Det.

Optical
fiber

O/E

HPA

E/O

LNA
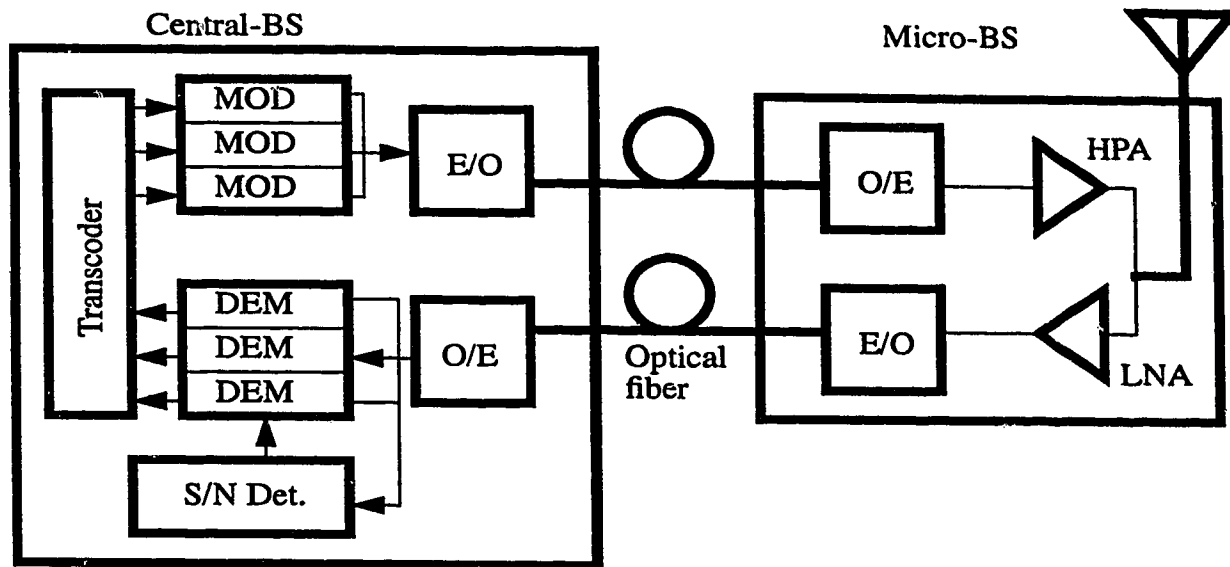
**Fig. 1.2 Optical fiber feeder microcellular system**

received signal power fluctuation. However the existing optoelectronic transducers place a limitation on the available optical power, bandwidth and linearity which directly affects the system performance. These factors essentially limit when the intermodulation and noise from the laser diode places a constraint on the bandwidth and carrier-to-noise ratio which can be achieved. In such cases, a highly linearized laser source [5] or many such lasers multiplexed together [6] have to be used in order to meet the wide dynamic range requirements of the overall link. Also, dynamic channel assignment techniques [7], can be made use of in such a way that intermodulation products among carriers can be minimized. Thus the hybrid fiber-radio technology can be considered to be an attractive alternative to the conventional coaxial cable medium in the delivery of broad-band signals to personal communication terminals.

## 1.3 OEM based fiber-radio systems

In systems that employ subcarrier multiplexed signal distribution, the entire signal set on the optical carrier is detected and amplified by using a wideband optical receiver. An electronic mixer down-converts the signal output from the receiver to an intermediate frequency (IF) for further signal processing. The complex hardware associated with the receiver subsystem can be made simpler by means of optoelectronic mixing [8]. The mixing process is achieved with simple photodetectors which can be realized in the form of a monolithic integrated circuit.

Three terminal devices like metal semiconductor field effect transistor (MESFET), high electron mobility transistor (HEMT) and heterojunction bipolar transistor (HBT), which form the basic building blocks of monolithic millimeter-wave integrated circuits (MMICs) have been demonstrated as optoelectronic mixers (OEM) [9]. A prime advantage of using a three terminal device is the good isolation that can be achieved between the electrical local oscillator (LO) and the IF ports. Presently, planar photodiodes have become very attractive for OEM applications [10] owing to their simplicity in structure, high frequency response and process compatibility with active components such as MESFET and HEMTs. Of the general class of photodiodes that have been considered as OEMs, much interest has grown in the interdigiated metal-semiconductor-metal photodetector (MSM-PD) due to its ease of integration with either MESFET or HEMT, its very low capacitance and high-speed with applications in optical signal distribution and detection.

With the OEM, the information signal carried by the optical carrier is converted directly to the electronic IF in the process of detection. Thus the wideband receiver amplifier can be

6

replaced by a low cost narrow bandwidth IF amplifier which effectively improves the noise floor of the overall system. OEM based transceivers are simple, compact and easy to construct. Such systems considerably simplify the radio-BS hardware and hence are a vital source of components in fiber-to-the-cell technology. Recently, a monolithic integrated OEM based on MSM-PD has been demonstrated in a fiber optic microwave link [11][12].

## 1.4 Thesis Outline

The purpose of this project was to study the properties of OEM for fiber optic links that find typical applications in microcellular communication networks.

Chapter 2 reviews various subcarrier mm-wave fiber optic links based on hybrid fiber radio techniques. Their relative advantages and disadvantages are described in the light of fiber-to-microcell technology and the relevance of OEM based hybrid fiber-radio links is discussed for simple and cost-effective network design. Chapter 3 describes the analysis of MSM-PD as an OEM. A model is obtained for the nonlinear optical output power of a laser diode in terms of the total injected current and also for the dc responsivity of the MSM-PD in terms of its applied bias. Thus the OEM is characterised in terms of its conversion loss and noise figure. Numerical results based on the above analysis are presented to estimate the overall link performance. Chapter 4 reports the experimental results for both single tone and two-tone subcarrier transmission in an analog fiber optic link. Results based on $\pi/4$-DQPSK modulated digital signal transmission over the fiber-radio link are presented. A detailed discussion on the OEM's suitability in hybrid fiber-radio links is presented. Chapter 5 concludes the thesis with a summary of the research results, and indicates possible areas of future research in this field.

7

# 2. MICROWAVE FIBER OPTIC LINKS

Microwave and millimeter-wave subcarrier transmission over fiber optic links has been attempted using laser diode direct modulation, external modulation, and heterodyne techniques based on laser diode, and photodiode nonlinearities. Direct modulation of high speed commercial laser diodes in practice, is limited to about 30 GHz [13]. On the contrary, external optical modulators, such as $LiNbO_3$ integrated devices, are capable of modulation into the mm-wave bands. Their disadvantages are high drive in voltages and optical insertion losses [14]. At the receiver end, three terminal devices like MESFET, HEMT and HBTs have been demonstrated as OEMs [9]. Recently much interest has grown in the use of interdigitated MSM-PD as OEMs for their speed of operation, planar structure and ease of integration with MESFET/HEMTs [11]. The MSM-PD could be used as an integrated transceiver which considerably simplifies the complexity and cost of the receiver [12].

This chapter reviews fiber optic mm-wave subcarrier transmission links which are based on intensity modulation direct detection schemes. A GaAs MSM-PD mixing link is proposed for the frequency upconversion of RF signals transmitted over the fiber optic link in a hybrid optical-radio environment. Such a system finds wide applications in microcellular mobile communication systems.

## 2.1 Directly Modulated Fiber Optic Links

Fiber optic link configurations are divided into two types. One is the directly modulated fiber optic link and the other the externally modulated fiber optic link. The directly modu-
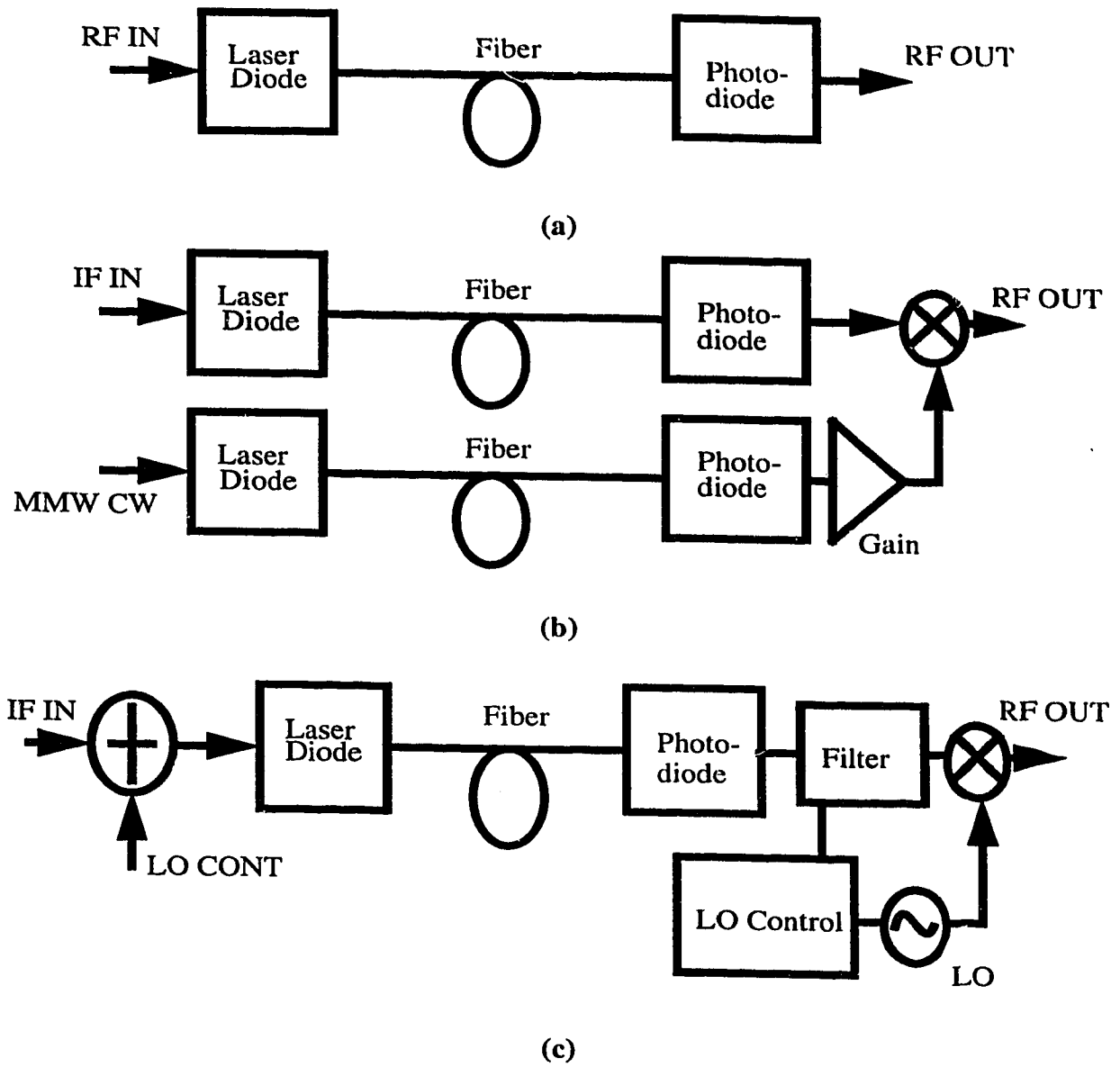
**Fig. 2.1 Fiber optic link architectures for microwave transmission**

(a) Direct modulation link. (b) Direct modulation twin link

(c) Frequency multiplexed direct modulation link

9

lated fiber optic link consists of a laser diode, a photodiode and a fiber transmission medium as shown in Fig. 2.1(a). The transmission bandwidth of such a link is determined by the frequency response of the laser diode, usually limited to frequencies below its relaxation oscillation frequency. Despite the advantages of potentially higher link gain and reduced number of components, the frequency transmission performance is limited by the laser diode. An alternative configuration to the link of Fig. 2.1(a) is shown in Fig. 2.1(b).

In this case the performance of each link can be optimized for each particular frequency and bandwidth by transmitting the IF signal (data) and MMW carrier separately over different FO links. The carrier link provides essentially a high frequency but very narrow bandwidth microwave signal. Since this link does not carry data or information, the laser nonlinearities could be exploited to extend the operating frequency well beyond the laser relaxation frequency [15][16]. Narrow band reactive matching circuits to the laser and photodetector can be used to reduce the system losses. Since the data link in this configuration operates at a lower frequency as compared to that in Fig. 2.1(a), the RIN in this scheme will be lower and the dynamic range will be higher accordingly.

A third variety of direct modulated link is shown in Fig. 2.1(c) and is unique in the sense that no microwave/mm-wave signals need to be transmitted by fiber. This eliminates the need for high-speed laser diodes and photodetectors, but an electrical LO is required to obtain the RF signal. Using the LO as a frequency synthesizer, the controlled signal can be transmitted over the fiber and RF frequencies can be adjusted at the optical transmitter end. This configuration is beneficial for microcellular distribution and antenna remoting applications and has high-frequency potential unlimited by the link properties.

## 2.2 Externally Modulated Fiber Optic Links

A typical schematic of the externally modulated link which consists of a laser source, an external modulator, a photodiode and a fiber medium is shown in Fig. 2.2(a). The link performance depends to a greater extent on the optical insertion loss and drive in voltage for 100 percent modulation of the external modulator. MM-wave subcarrier frequencies are optically generated by using a Mach-Zehnder interferometer realized in LiNbO$_3$. Mach-Zehnder modulators are typically expensive and somewhat lossy. The configuration shown in Fig. 2.2(b) improves the loss performance of the overall system by optimizing the two separate links, but results in an increase in components, complexity and cost. To eliminate the second fiber cable and photodiode, the link shown in Fig. 2.2(c) can be used. This link utilizes only a single photodiode and fiber with a filter to separate the MMW carrier and IF signal at the detector output and is suitable for wavelength division multiplexed (WDM) systems. The carrier signal at the filter output is suitably amplified before it is upconverted alongwith the incoming data to a higher frequency signal suitable for radiation. The bandwidth of the external modulator in Figs. 2.2(b) and 2.2(c) can be as narrow as possible, thus reducing the driving voltage and improving the gain of the overall link.

## 2.3 Fiber Optic Mixing Links

Optical devices such as laser diodes, photodiodes and external modulators exhibit inherent nonlinearities even when biased properly [17][18]. Figs. 2.3(a)-(c), show fiber optic mixing link configurations based on laser diode mixing, photodiode mixing and dual mixing respectively. These architectures utilize the nonlinearity to up-convert the IF signal to the microwave frequencies thereby making the links simple and easy to implement [19][20].
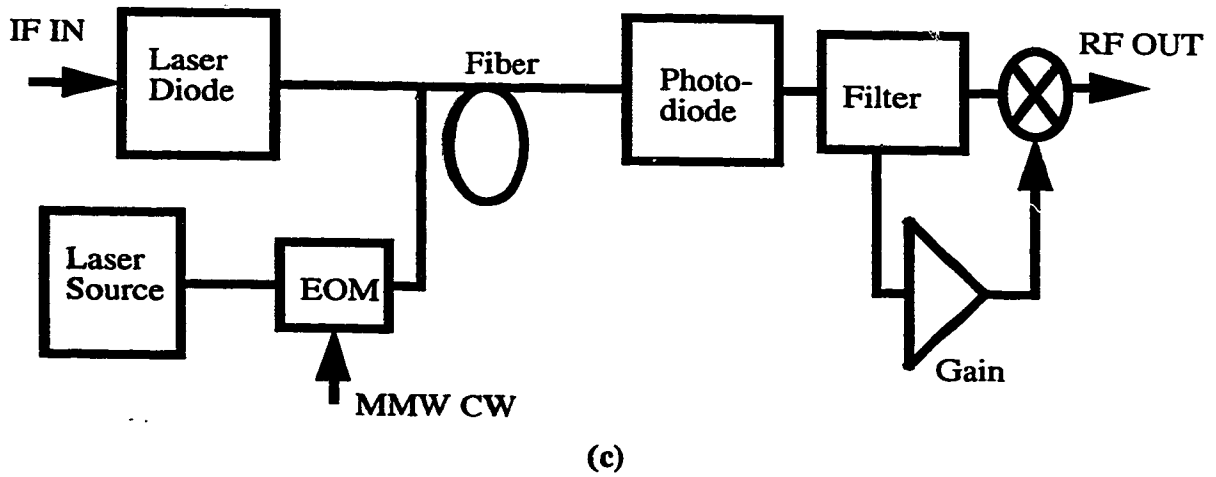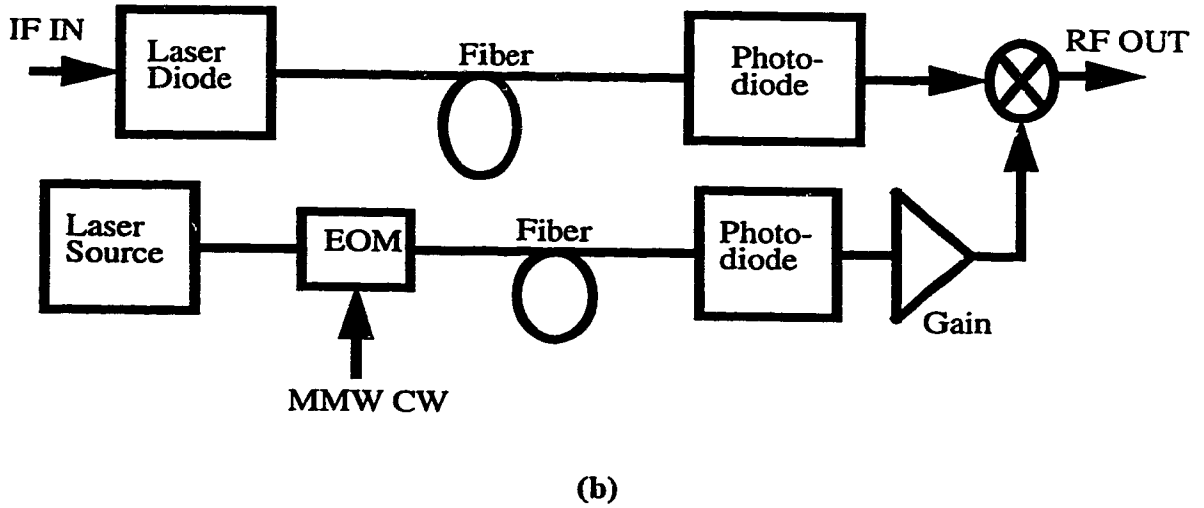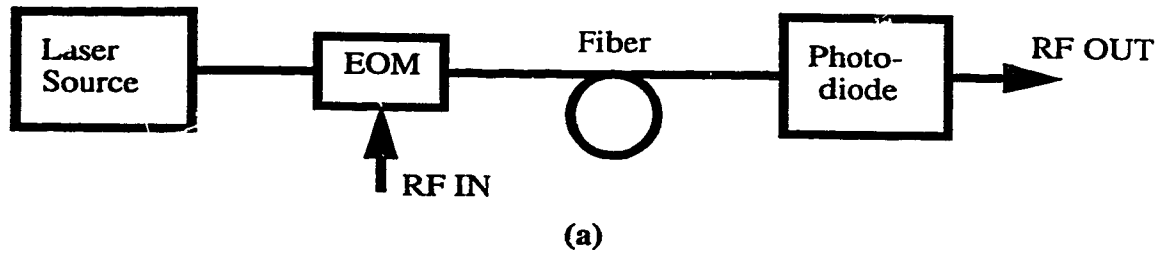
**Fig. 2.2 Fiber optic link architectures for microwave transmission**
**(a) External modulation link. (b) External modulation twin link**
**(c) Combined direct and external modulation link**

The laser diode can be operated as an optical source and a microwave mixer simultaneously if the electrical LO power is supplied to it. Similarly, the photodiode can operate as optical detector as well as a microwave mixer if electrical LO power is supplied to the photodiode bias. Since the photodiode mixing receiver eliminates the need for an electrical mixer, the receiver hardware can be simplified. Additionally, the photodiode mixing link only carries the information. The carrier is generated at the remote BS. All of these optical devices must be fully characterized to obtain the optimum operating points where most efficient mixing occurs without substantial signal distortion.

The MMW carrier link in Fig. 2.3(b) can be replaced by a stable LO. Figs. 2.3(a) and 2.3(c) are advantageous in terms of reduction of the requirements for photodiode and fiber. Fig. 2.3(c) presents a beneficial compromise between performance and system complexity. This link combines the simplicity of single laser/fiber/detector transmission. Although there is loss in the laser generated IF signal due to the external modulator insertion loss, the performance is not significantly deteriorated if high output power laser diodes are utilized for the modulator source. The EOM is a key component in this link for realizing mm-wave transmission. In this configuration, the IF signal can be used to modulate the laser diode, while a single frequency subcarrier can modulate the EOM. Thus the design of EOM is simplified in terms of its operating bandwidth. Conversely, in the case where the subcarrier multiplexed signal directly modulates the EOM, the EOM design becomes more complex, in terms of meeting the bandwidth requirements for adequate signal transmission. Thus a single source is required to produce a subcarrier-frequency modulated optical carrier for an economical and compact optical transmitter. This configuration finds typical applications in high capacity wavelength multiplexed systems.
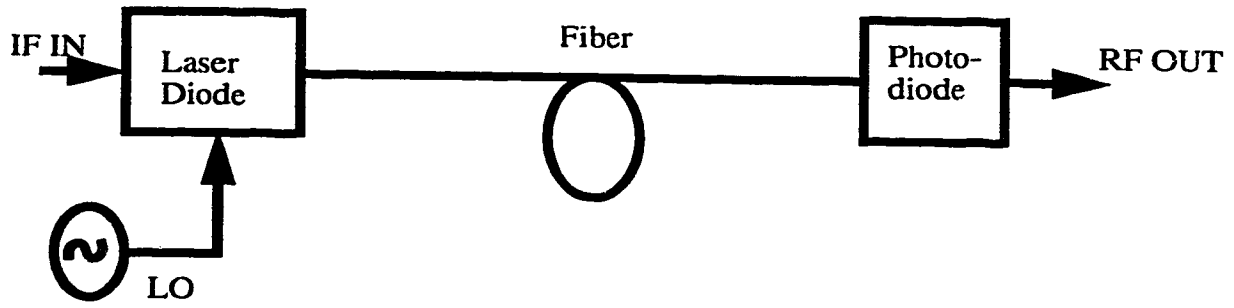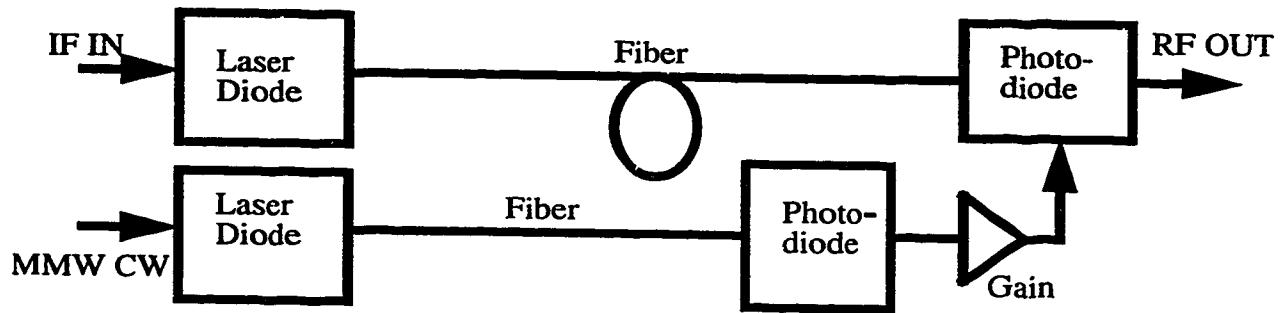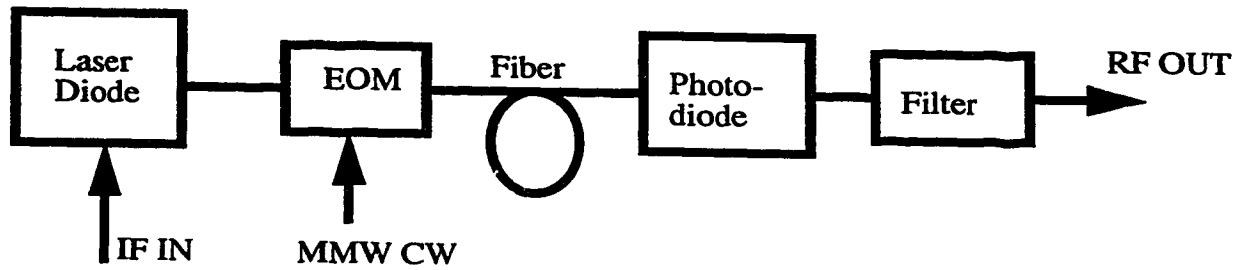
**Fig. 2.3 Fiber optic mixing links for microwave transmission**
**(a) Laser diode mixing. (b) Photodiode mixing link**
**(c) Dual mixing link**

14

## 2.4 Novel Fiber Optic Link Architectures

In the recent few years, the nonlinearities inherent in the optical sources and detectors have been exploited with simple configurations to demonstrate the mm-wave signal transmission over optical fibers thereby extending the link bandwidth considerably [16][18]. There has also been a great deal of interest in studies related to the suppression of the undesired frequencies resulting from the device nonlinearities [21-24]. A variety of schemes including balanced laser harmonic generation, image cancellation laser and photodiode mixing, laser receiver and balanced laser receiver mixing, external modulator mixing and image cancellation external modulator mixing links etc. have been reported in literature [22]. Of these, the most important schemes based on the laser diode and photodiode nonlinearities will be discussed in this section. These configurations can be efficiently made use of to service broadband personal communication systems.

### 2.4.1 Balanced Laser Mixing Link

This particular scheme is illustrated in Fig. 2.4.1(a). The laser diode in this case acts as a microwave mixer and generates frequency up-/down converted signals in response to two input frequencies (LO and IF/RF signals). The output power level of the LO is much larger than that of the upper and lower side band signals if the IF signal level is low [18]. The LO power can be suppressed by a microwave filter placed at the detector output. An alternative approach to suppress the LO frequency without using the filters is shown in Fig. 2.4.1(b). Two out-of-phase dividers and two in-phase combiners are required to supply the out-of-phase local frequencies and out-of-phase IF signals to the laser diodes. Since the two detected local frequencies have a phase difference of $180^{\circ}$, they are cancell-
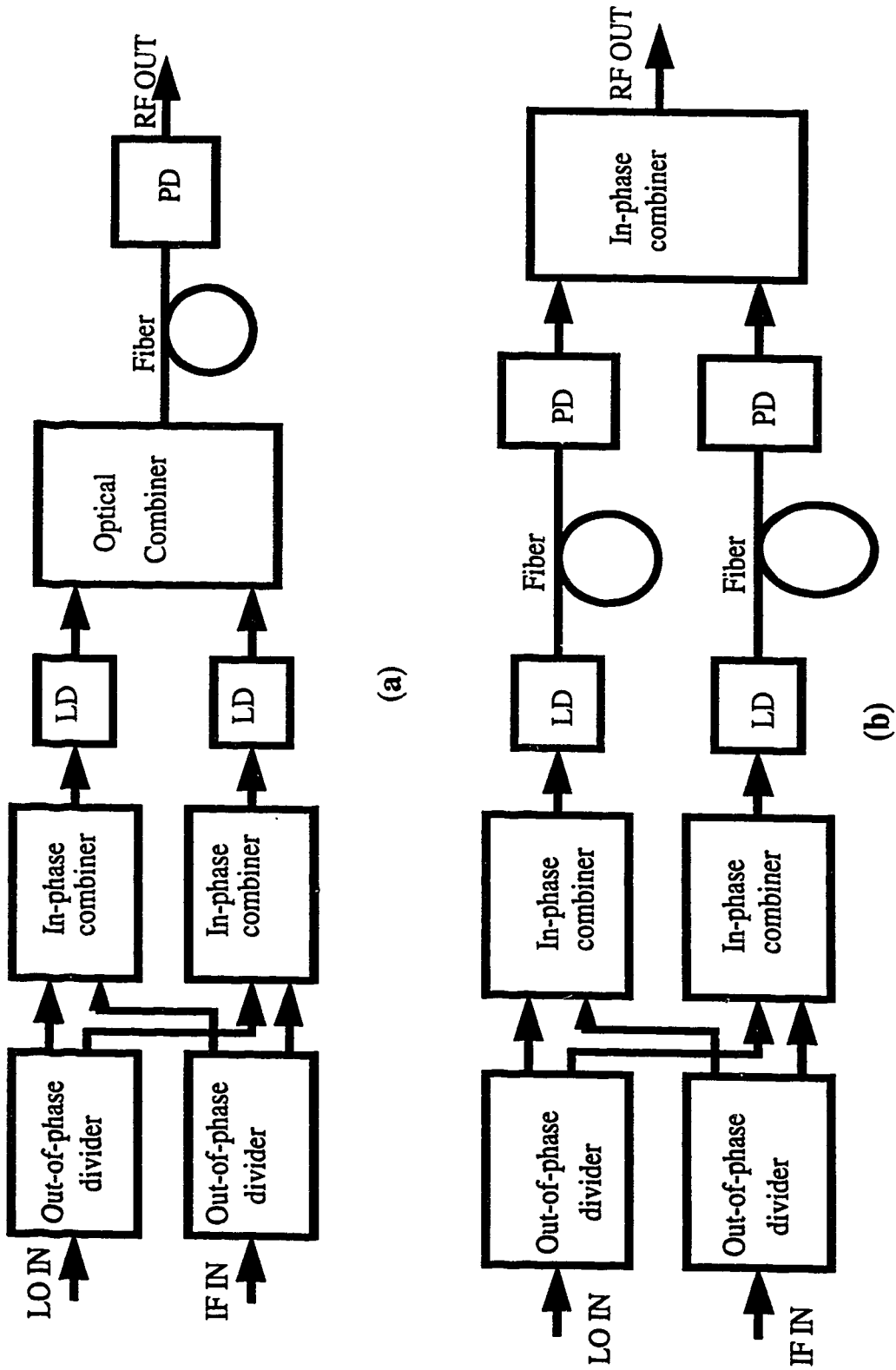
Fig. 2.4.1 Link architectures based on balanced laser mixing
(a) Single-fiber link. (b) Twin-fiber link

ed at the detector output leaving the up-/down converted signals. For short distances, the loss due to link lengths in Fig. 2.4.1(b) can be assumed to be nearly zero. The phase noise due to the LO component might be a serious parameter for long distance transmission.

## 2.4.2 Balanced Photodiode Mixing Link

Fig. 2.4.2 shows the configuration of the balanced photodiode mixing link. This link can be used to suppress the LO frequency without using filters with the help of two out-of-phase dividers that supply the out-of-phase IF frequencies and local frequencies to the laser diodes and the photodiodes respectively. Although the phase difference of the detected IF signals at each photodiode remains out-of-phase, the up-/down converted signals become in-phase upon mixing with the out-of-phase local signals whereas the phase difference of the reflected local frequencies remains out-of-phase. Thus, in principle, the output contains only the up-/down converted signals by combining each of two output signals in-phase. The hybrid circuits attached to the photodiodes can be utilized to separate the incident local signals and reflected signals.
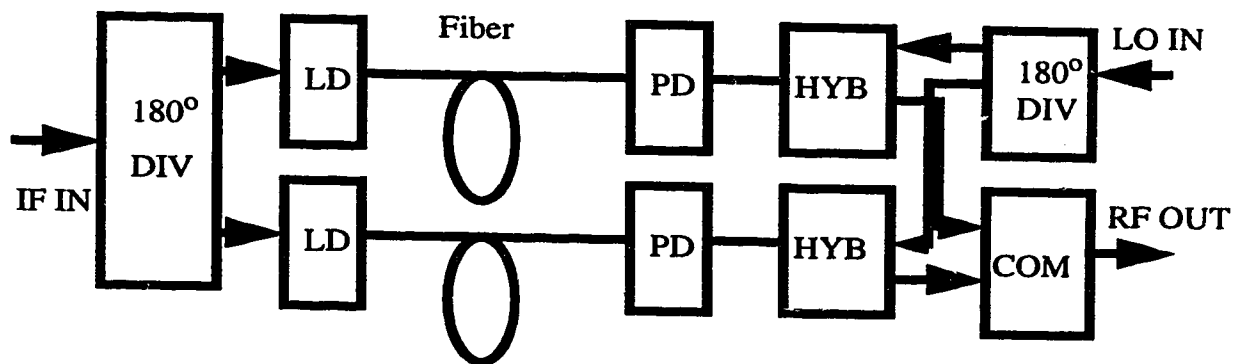


**Fig. 2.4.2 Link architecture of balanced photodiode mixing**

## 2.5 Optical/Microwave Monolithic Integrated Circuits

Optoelectronic Integrated Circuits (OEICs) have received wide attention since monolithic integration offers significant advantages in cost reduction, compactness and performance improvement [25][26]. A variety of OEICs which use different devices and fabrication processes have been proposed whose performance is comparable to that of hybrid integrated circuits (HICs). Despite many advantages, monolithic integration of OEICs has yet to outperform hybrid integrated circuits due to their complicated fabrication processes. This section discusses in brief the various electronic devices that are used as photodetectors which are made by monolithic millimeter-wave integrated circuit (MMIC) process.

MMIC technology has the potential to reduce the size and cost of electrical transceivers [27]. With many microwave circuit functions being realized by MMICs, design, fabrication and measurement technologies for MMICs are becoming mature. These components are being utilized to configure not only transceivers for radio but also optical/RF transducers for fiber optic subcarrier transmission links [28][29]. Alternatively, OEICs can be used in place of optical/RF transducers. To extend the frequency range of circuits using these devices, high-speed photodetectors [30], can be integrated with RF components in hybrid integrated circuits (HIC). Despite the performance improvement by HIC over discrete component technologies, they have cost, size and performance limitations due to the essential differences between the MMIC and discrete device fabrication process. Thus, if the photodetection circuits can be fabricated by the current MMIC process, this technology is most promising to realize compact and cost-effective optical/RF transducers.

The high-speed photodetector devices are classified into two groups, i.e. two terminal

devices (diode) and three terminal devices (transistor). Two terminal devices including

PIN diodes [31], Avalanche photodiodes (APD) [32], Schottky barrier diodes (SBD) [30],

photoconductors (PCD) [33] and metal-semiconductor-metal photodiodes (MSM-PD)

[34], have been reported. Since PIN diodes are basically vertical structural devices, the

fabrication process becomes more complicated than planar structural devices such as

SBDs, PCDs and MSM-PDs [35]. Although the PCDs have a large photocurrent gain, the

available bandwidth is lower than that of other SBDs and MSM-PDs [36-38]. The link

that is proposed in this project will be based on a MSM-PD that performs simultaneous

photodetection and frequency conversion.

As for three terminal devices, MESFET [39], HEMT [40] and HBT [41] have been stud-

ied for photodetectors. These devices can realize not only photodetection functions but

also RF amplification and frequency mixing. Due to their bandwidth and process compati-

bility limitations, phototransistors cannot be realized as MMICs. Since MSM devices are

process compatible with MESFET and HEMTs, monolithic integration of compact and

cost-effective optical/RF transducers is possible.

## 2.6 Proposed OEM link for cellular communications

The fiber optic link discussed in this project is based on the MSM-PD OEM. The intensity

modulation direct detection link consists of a laser diode transmitter in the central station

and an optoelectronic mixer (OEM) based transceiver in the base station. This particular

configuration is well suited to cellular communication systems because it considerably

reduces the radio base station hardware by eliminating the need for an electric mixer and

further signal processing.

Low frequency modulation of the laser diode eliminates the need for a high-speed expensive laser transmitter. In some situations, a low-cost LED with linear transfer characteristics and suitable IF bandwidth could be utilized in place of a laser diode in the central station. The IF modulated signal can be upconverted to a desired frequency at the receiving end with the help of an OEM along with an input electrical LO signal. The LO frequency and its harmonics at the mixer output can be eliminated by using a passive filter. Thus the detected output consists of only the IF signals upconverted to RF carriers which can be suitably amplified before being radiated from the base station to serve the mobile users. The downlink from the central station to the base station performs the opposite function, downconverts the radio signals received by the receiving antenna, using an electronic mixer, for transmission to the central station over the fiber link [42].

### 2.6.1 GaAs MSM Photodetectors

A monolithic integrated GaAs MSM-PD is used as an OEM in this experiment. The MSM-PD can be modelled by a photocurrent source and a very small capacitance, typically a few tenths of a picofarad, formed by the metal contacts and semiconductor dielectric of these devices. The structure of an MSM-PD and its circuit symbol is shown in Fig. 2.5. The construction and operation principles are discussed in brief here as follows.

An epitaxially-grown buffer layer of GaAs is deposited on top of a semi-insulating GaAs substrate. Then, an intrinsic layer of GaAs, about 1 $\mu$m thick is grown on top of the buffer layer. Finally, thin, interdigital metal fingers, usually layers of titanium, tungsten and gold,
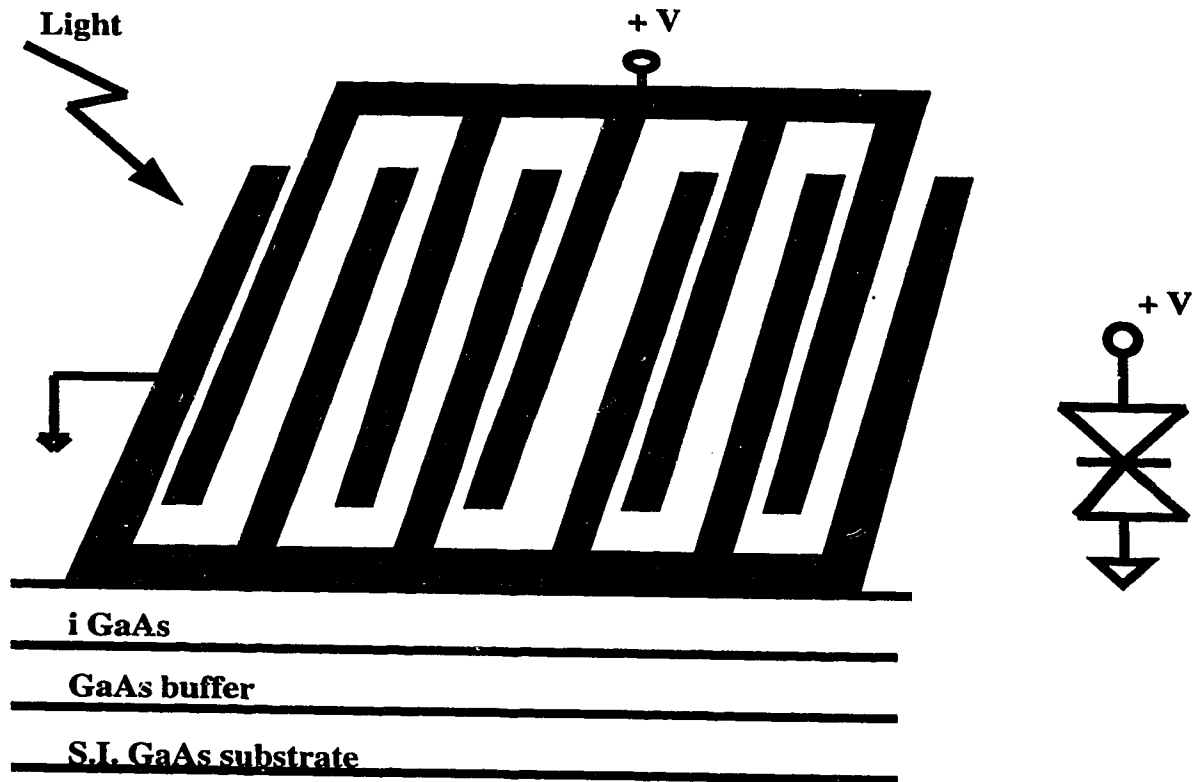
**Fig. 2.5 Structure of GaAs MSM-PD**

are laid down in the pattern depicted in Fig. 2.5. Typical finger width and finger spacing is on the order of a few μm. The area immediately surrounding the MSM structure is etched down to the substrate, isolating the MSM region on a mesa, thus preventing photogenerated charge carriers in the active layer from migrating into it, thereby slowing down the response. The processing steps involved here are similar to those in the fabrication of MESFETs and HEMTs, which lend simultaneous monolithic integration of MSM and MESFET or HEMT devices to create monolithically integrated, wide band optical receivers [43][44].

When a bias voltage is applied across the two sets of interleaved fingers of an MSM, an electric field is formed in the GaAs active layer beneath the fingers. When light of an appropriate wavelength light strikes the top of the MSM, some is reflected by the fingers, and the rest enters the GaAs active layer, creating electron hole pairs which are then very quickly swept to the fingers on the MSM by the electric field. MSM PDs are well suited for very high speed photodetection due to the very low capacitance between the metal fingers. Typical MSMs with areas of about 100x100 $\mu m^2$ and 1 $\mu m$ finger spacing and finger width can have an internal capacitance of tens to a hundred or so fF.

The GaAs based MSM-PD requires operation wavelength of about 850 nm due to the availability of the laser sources operating at similar wavelengths. For longer wavelengths, InGaAs based devices have to be used due to their low dark currents. Also, since lasers in the long wavelengths have stringent linearity and stability requirements besides being very expensive, it is possible to use cheap laser sources that are readily available in the low wavelength region. Thus the RF signals could be used to modulate the laser sources and upconvert to the desired frequency using photodiode mixing techniques in the remote base stations. This simplifies the overall system complexity and cost.

### 2.6.2 π/4-DQPSK signal transmission

The IS-54 cellular standard specifies π/4 shifted, differentially encoded Quadrature Phase Shift keying (π/4-DQPSK) modulation. A π/4-DQPSK signal constellation has 8 states. These states can be considered to be formed by the superposition of two Quadrature Phase Shift keying (QPSK) constellations, offset by 45° relative to each other, as shown in Fig. 2.6. The two constellations are used alternately to transmit each symbol, and thus the suc-

cessive symbols have a relative phase difference of 45° or 135°. The maximum phase change for $\pi$/4-DQPSK is 135°, as compared to a maximum phase change of 180° for QPSK. Therefore, a $\pi$/4-DQPSK modulated signal has less envelope fluctuation than a QPSK modulated signal and can be detected using differential or coherent detection. Differential or discriminator detection is a simple and straight forward approach for directly modulated links whereas coherent detection requires complex receiver circuitry. In a fast fading environment, coherent detection results in a higher bit error rate (BER) than differential detection and hence will be made use of in the experimental investigations.

This project is aimed at the analysis and experimental characterization of the OEM in a fiber optic link. The detailed analysis of this link will be presented in the next chapter and the experimental results based on analog and $\pi$/4-DQPSK digital signal transmission will be discussed in chapter 4.
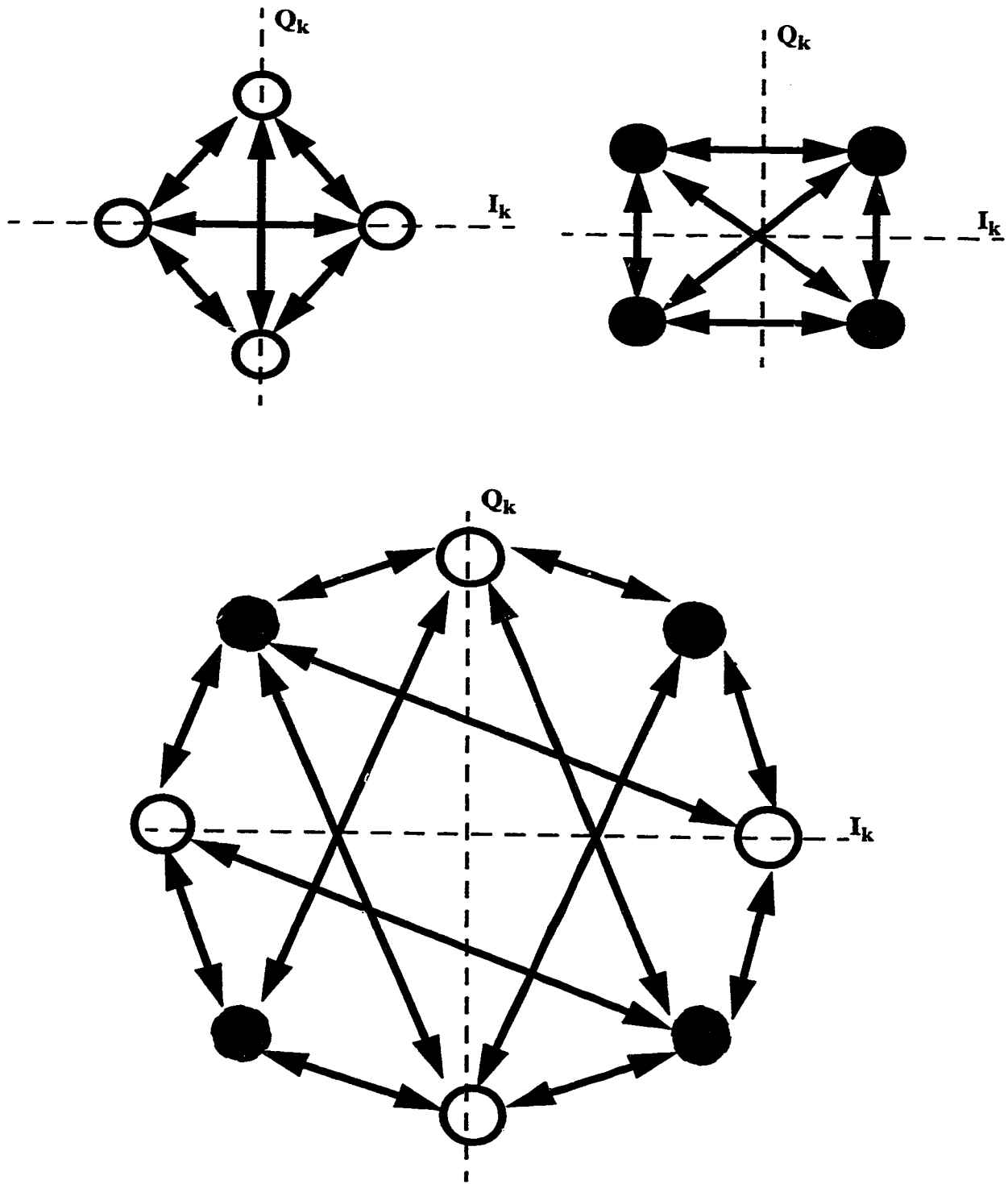
Fig. 2.6 Illustration of π/4-DQPSK signal constellation

# 3. THEORETICAL ANALYSIS

This chapter describes the OEM based fiber optic microwave SCM link for microcellular communication systems. The laser diode transfer characteristics are examined in terms of its optical output power as a function of the injected current. The linearity of the laser diode is discussed in terms of its intermodulation distortion. The analysis of an OEM based on a MSM-PD is presented and the overall link performance evaluated in terms of the carrier-to-noise ratio. Numerical results based on computer simulations are presented to supplement the above analyses.

## 3.1 OEM based fiber-radio link

The schematic block diagram of the OEM based fiber optic link is shown in Fig. 3.1.
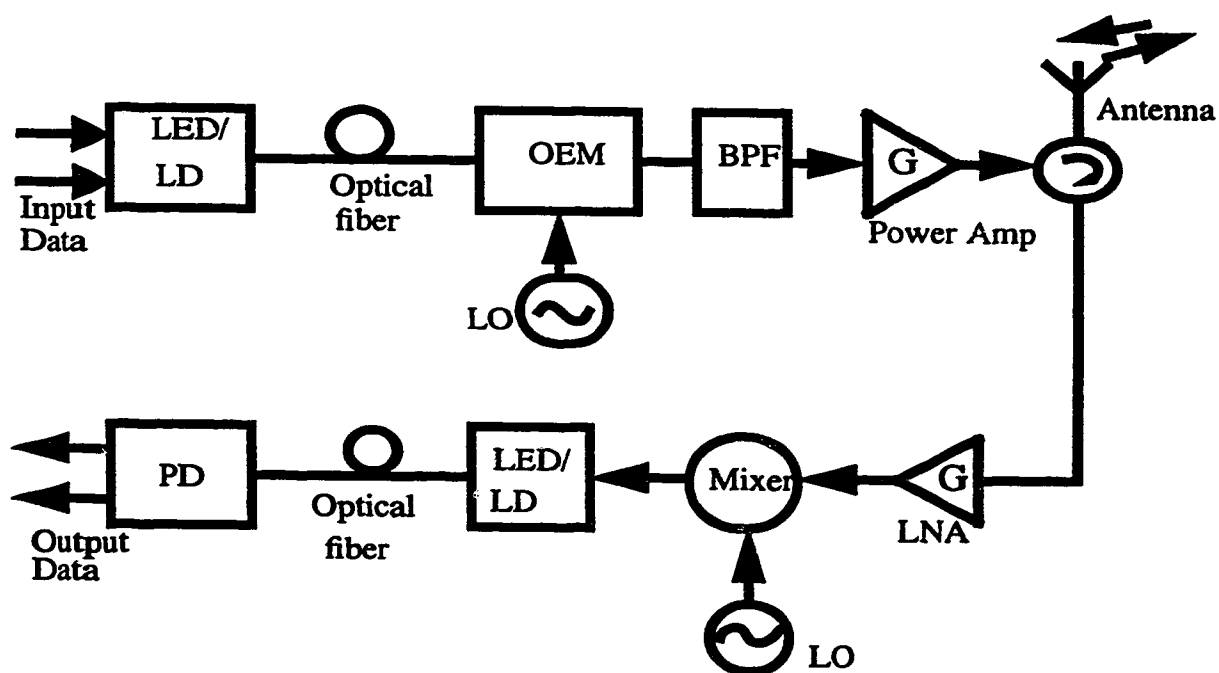


**Fig. 3.1 Schematic of the fiber optic microwave link**

The transmitter in the central station consists of a laser diode whose intensity is directly modulated by the microwave subcarrier signals. After transmission the modulated optical signals are converted to electrical signals in the BS with the help of an OEM that acts as a photodetector and upconverter. In the analysis of the system the fiber is assumed to be lossless and non-dispersive. Our experimental link used a short length of multimode optical fiber. With the OEM, the signal carried by the optical carrier is upconverted directly to a carrier frequency in the process of detection thereby eliminating the need for an electric mixer as in a conventional receiver. Thus the OEM performs photodetection and frequency conversion simultaneously and is therefore a key component in the performance evaluation of this link. The advantage is that narrow bandwidth amplifiers can be employed at the OEM output to raise the desired signal to a suitable level before radiation. Also, with the baseband signal transmission, the requirement of a high speed laser diode or an external optical modulator is avoided and the subcarrier can be generated locally in the BS for efficient radiation. This approach considerably simplifies the system design and reduces the cost.

Amplitude

$\Delta f$

$f_1$  $f_2$    $f_{LO}$   Frequency
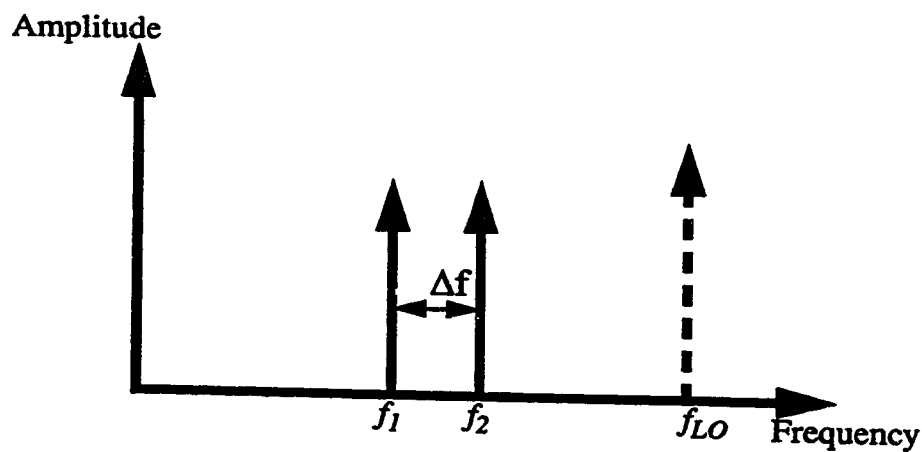
**Fig. 3.2 Spectrum of a 2-channel SCM system**

Here, analysis of SCM optical transmission system is restricted to two RF channels in order to supplement the theory with experimental results in chapter 4. The frequency spectrum of such a configuration is shown in Fig. 3.2. Frequencies $f_1$ and $f_2$ represent the carrier frequencies of two subcarriers which are closely spaced and the local oscillator, $f_{LO}$, is shown by a dashed line. The local oscillator frequency is larger than the signal bandwidth of each of the subcarriers being transmitted.

## 3.2 Non-linear Laser Diode

In this section, we obtain expressions for the nonlinear optical output power of the laser diode as a function of its total injection current. The non-linear laser source produces light output that has frequency components at signal frequencies, as well as their harmonics and intermodulation products and they will be discussed in the next section.

The output power $P(t)$ of a laser diode is generally a non-linear function of the total injection current $I(t)$ which can be idealized as shown in Fig. 3.3.
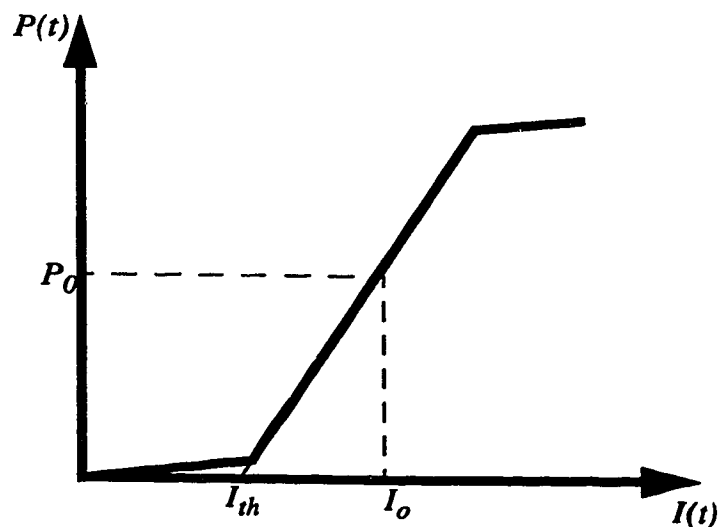
**Fig. 3.3 Output power vs injected current in a typical laser diode**

For the two subcarrier case, the modulation current applied to the laser is given by

$$I(t) = I_o + (I_o - I_{th}) \{m_1 \cos(\omega_1 t + \phi_1) + m_2 \cos(\omega_2 t + \phi_2)\} \tag{3.1}$$

where $I_o$ is the dc bias current, $I_{th}$ is the threshold current of the laser, $m_i (i=1,2)$ are the optical modulation indices (OMI) and $\phi_i (i=1,2)$ are the associated phase values, of the two carriers respectively. The modulation depths can be assumed to be identical for both channels but this restriction may not always be necessary. The light output $P(t)$, in response to the modulation current can be expressed as a Taylor series about $I_o$ as follows [45]:

$$P(t) = P_0 + \sum_{n=1}^{N} \frac{\left\{\frac{d^n P}{dI^n}\right\}}{n!} [I(t) - I_o]^n \tag{3.2}$$

where $P_0$ is the power at the dc bias current. The value of $N$ is chosen to be equal to 3 assuming that the higher order terms in the series expansion of Eqn. (3.2) are negligible. From Eqn. (3.1), it follows that

$$I(t) - I_o = I_1 \cos(\omega_1 t + \phi_1) + I_2 \cos(\omega_2 t + \phi_2) \tag{3.3}$$

where $I_1$, and $I_2$ are the peak currents in the two channels given by $I_1 = m_1 (I_o - I_{th})$, $I_2 = m_2 (I_o - I_{th})$ respectively.

Let $I(t) - I_o = (I_o - I_{th})I$, where $I = m_1 \cos(\omega_1 t + \phi_1) + m_2 \cos(\omega_2 t + \phi_2)$.

Thus the ouput power in Eqn. (3.2) can be expressed as

$$P(t) = P_0 + c_1 (I(t) - I_o) + c_2 (I(t) - I_o)^2 + c_3 (I(t) - I_o)^3 \qquad (3.4)$$

where the coefficients $c_1$, $c_2$ and $c_3$ can be interpreted as the slope efficiencies(W/A, W/A$^2$, W/A$^3$) of the transfer characteristic, in their increasing order. Thus the optical power $P(t)$ can be simplified and expressed as:

$$P(t) = P_0 \left( 1 + \frac{c_1}{P_0}(I_o - I_{th})I + \frac{c_2}{P_0}(I_o - I_{th})^2 I^2 + \frac{c_3}{P_0}(I_o - I_{th})^3 I^3 \right) \qquad (3.5)$$

Therefore the output optical power of the laser diode can be expressed as

$$P = P_0 \left( 1 + a_1 I + a_2 I^2 + a_3 I^3 \right) \qquad (3.6)$$

where the constants $a_1$, $a_2$ and $a_3$ depend on a specific laser diode model and in our case they are assumed to be 1 A$^{-1}$, 0.1 A$^{-2}$ and 0.01 A$^{-3}$, respectively [46]. The detailed analytical expression (refer to Appendix A) for the power output in terms of the various mixing components that contribute to the intermodulation distortion can be obtained from the expansion of Eq. (3.6) as:

29

$$P(t) = P_0\left( 1 + m_1 \cos(\omega_1 t) + m_2 \cos(\omega_2 t) + a_2\left[\frac{m_1^2 + m_2^2}{2}\right] \right. \tag{3.7}$$

$$+ a_2\left\{\frac{m_1^2 \cos(2\omega_1 t) + m_2^2 \cos(2\omega_2 t)}{2} + m_1 m_2 \cos(\omega_1 + \omega_2)t + m_1 m_2 \cos(\omega_1 - \omega_2)t\right\}$$

$$+ a_3\left(\frac{3\left[m_1^3 \cos(\omega_1 t) + m_2^3 \cos(\omega_2 t)\right]}{4} + \frac{m_1^3 \cos(3\omega_1 t) + m_2^3 \cos(3\omega_2 t)}{4}\right.$$

$$+ \frac{3}{2}m_1^2 m_2 \cos(\omega_2 t) + \frac{3}{4}m_1^2 m_2\left[\cos(2\omega_1 + \omega_2)t + \cos(2\omega_1 - \omega_2)t\right]$$

$$\left.\left. + \frac{3}{2}m_2^2 m_1 \cos(\omega_1 t) + \frac{3}{4}m_2^2 m_1\left[\cos((2\omega_2 + \omega_1)t + \cos(2\omega_2 - \omega_1)t)\right]\right)\right)$$

## 3.2.1 Harmonic and Intermodulation Distortion

In a directly modulated link, the nonlinearity of the relation between laser diode optical power and drive current can generate higher harmonics and intermodulation distortion (IMD) products. The bandwidth of such a link is determined by the low and high frequency limits of the transmitter frequency response [47]. The low frequency limit is set by the cut-off frequency of the low-pass filter (capacitor) in the bias tee. The high frequency limit is set by the roll off in the frequency response of the laser diode, which has a typical slope of 40 dB/decade beyond the relaxation oscillation frequency. Since most fiber optic links for microwave applications require a narrow bandwidth [47], the higher harmonics and second-order IMD products fall outside the passband and can be neglected as they do not pose a problem. However the third-order IMD ($IM_3$) product frequency components fall within the link passband and are therefore responsible for the spurious response. Thus, the link linearity is determined by the level of $IM_3$ products.

The $IM_3$ occurs mainly in the LD modulation process and originates from:

(1) Injection current versus output light (I-L) curve nonlinearity.

(2) Dynamic nonlinearity due to intrinsic photon-electron nonlinear interaction.

(3) Non-symmetrical threshold clipping (over-modulation distortion).

$IM_3$ due to I-L curve nonlinearity and over-modulation is independent of modulation frequency, whereas $IM_3$ due to dynamic nonlinearity increases with an increase in the modulation frequency. The IM distortion due to dynamic nonlinearity and over-modulation are not considered in this analysis.

The $IM_3$ is mea $\cdots$ red by combining two equal power RF signals $P_{in}$ at closely spaced frequencies $f_1$ and $f_2$, $(f_2 > f_1)$ in a power combiner, and applying the composite signal to modulate the laser diode. Because of the laser diode nonlinear characteristic, second-order intermodulation tones will appear at $f_1 + f_2$ and $f_2 - f_1$, third-order intermodulation tones will appear at $2f_1 - f_2$, $2f_2 - f_1$, and the harmonics at $2f_1, 2f_2, 3f_1, 3f_2$, and so forth. Assuming identical modulation indices $m_1 = m_2 = m$ in Eqn. (3.3), the $IM_3$ for a 2 - channel case can be calculated (refer to Appendix A) as the laser diode third-order transfer function from Eqn. (3.7) as

$$IM_3\,(dB) = 10\log\left[\frac{9m^4 a_3^2}{16\left(1 + \frac{3}{4}a_3 m^2\right)^2}\right] \tag{3.8}$$

where $m$ is related to $P_{in}$ as

$$m = \frac{\sqrt{\dfrac{2P_{in}}{R_{ld}}}}{I_o - I_{th}}$$

where $R_{ld}$ is the laser diode input impedance, $I_o$ and $I_{th}$ are the laser bias and threshold currents respectively. In order to avoid the overmodulation distortion, the maximum value of $m$ in the 2-carrier modulation is suppressed to less than 50%. When total $OMI$ is less than 100%, $IM_3$ is generated by I-L curve nonlinearity and dynamic nonlinearity of the LD. In this case $IM_3$ is strongly dependent upon $OMI$ and is in proportion to $m^4$ as given by Eqn. (3.8). Since $m$ is inversely proportional to the laser bias current, $IM_3$ decreases with increasing bias at a fixed $P_{in}$ and is illustrated in Fig. 3.4.
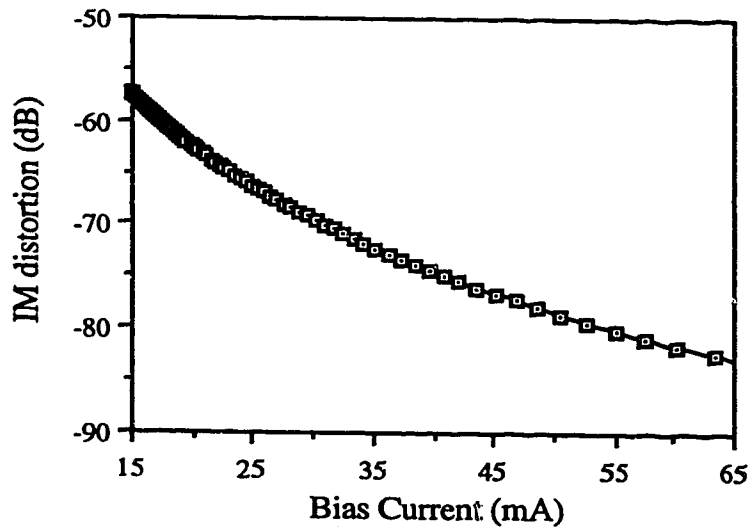


**Fig. 3.4 IM distortion as a function of laser bias current**

The laser diode transfer function is defined as the ratio of the output amplitude to the input amplitude. Plotted on a log-log scale, the fundamental transfer function is a line with a

32

slope of unity, the second-order transfer function is a line with a slope of two, and the third-order transfer function is a line with a slope of three. Both the second- and third-order transfer functions intersect the fundamental transfer function line and these intersections are called the second- and third-order intercept points, respectively. The second-order output intercept point ($IP_2$) and the third-order output intercept point ($IP_3$) can be calculated by knowing the power in each of the components as [48]:

$$IP_2 = 2P_f - P_2$$

$$IP_3 = \frac{3P_f - P_3}{2} \tag{3.9}$$

where

$P_f$ = output power of each of the two fundamental tones in dBm,

$P_2$ = output power in each of the second-order IMD products in dBm,

$P_3$ = output power in each of the third-order IMD products in dBm.

The nonlinear effects of saturation due to the rapid change in distortion resulting from the increase in the input signal power are best represented by the 1 dB compression point. It is defined as a measure of the output power level, when the input power has been raised to a point on the transfer characteristic that results in a 1 dB reduction in output power and can be obtained experimentally from the transfer characteristics which will be discussed in chapter 4.

## 3.3 MSM Photodetector as an OEM

Due to their simple planar geometry, high bandwidth, very low capacitance and process compatibility with MESFETs and HEMTs, MSM-PD's have become attractive for frequency conversion and mixing applications. The performance of the MSM-PD as an OEM is described in terms of its mixing responsivity.

### 3.3.1 Mixing Responsivity

The mixing responsivity $R$ is defined as the ratio of the root mean square current in the mixing detector to the root mean square variation in the incident optical signal [49]:

$$R = \frac{I_{rms}}{P_{rms}}$$

(3.10)

Efficient mixing occurs at the photodetector because the responsivity $R$ of the MSM-PD can be controlled by an applied voltage [49]. For a MSM-PD, $R$ depends on the voltage applied to the device, wavelength of operation, the size of the active area of the device, finger width, length and spacing, etc. [50]. For an intensity modulated optical signal $P(t)$ and a LO signal $V(t)$ applied as the bias, the responsivity can be written as $R(t) = K[V(t)]$, and the output photocurrent is given by

$$I_{ph}(t) = K[V(t)]P(t)$$

(3.11)

The mixing efficiency of the MSM-PD depends on the function $K[V(t)]$. The photocurrent generated at the mixer output contains signal, LO, harmonics, intermodulation and IF components. RF channel selection can be done using a filter and the signal is further

34

amplified by a narrow band IF amplifier before it undergoes further signal processing.

## 3.3.2 Responsivity based on Polynomial Approximation
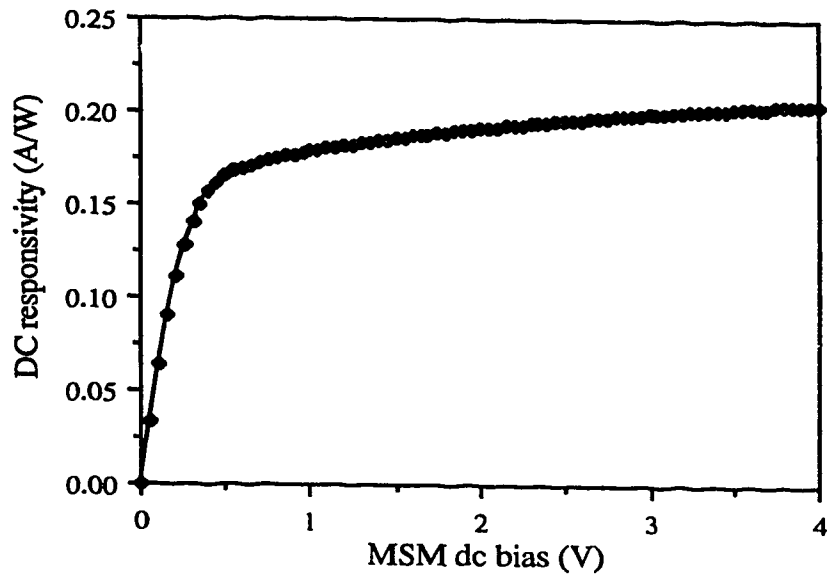


**Fig. 3.5 DC responsivity of the MSM-PD as a function of its bias**

In order to obtain a better understanding of the mixing behavior of the MSM-PD, $R_{V_{dc}}$ is modeled in terms of the applied voltage by an analytical function which is given by:

$$R_{V_{dc}} = \left( A_0 + A_1 V_{dc} + A_2 V_{dc}^2 + A_3 V_{dc}^3 \right) Tanh \left( \alpha V_{dc} \right) \qquad (3.12)$$

where the integral constants $A_0$, $A_1$, $A_2$, and $A_3$ are obtained from a curve fitting model of the experimental data and are listed in Table 1 (p. 106). The dc responsivity of the MSM-PD as a function of bias obtained from Eqn. (3.12) is shown in Fig. 3.5. It can be seen from Eqn. (3.12) that the responsivity is linearly related to the bias at low biasing voltages,

35

where the responsivity is also low. This can be physically attributed to the carrier transit time being long when compared with the carrier lifetime. On the contrary, when the MSM-PD is highly biased, the responsivity becomes independent of the applied voltage.

For mixing operation, the MSM-PD bias is modulated by a local oscillator voltage $V_{lo}$ and the resulting responsivity $R$ is obtained as

$$R = \sum_{n=0}^{N} \{A_n (V_{dc} + V_{lo}\cos(\omega_{lo}t))^N\} \, Tanh\,[\alpha\,(V_{dc} + V_{lo}\cos(\omega_{lo}t))] \quad (3.13)$$

where $N=3$ yields a good agreement with the measured results. In the series expansion of Eqn. (3.13), it is assumed that the hyperbolic tangent shaping function $(Tanh)$ is unity for bias voltages $(V_{dc}: 0 -4 \, V)$ considered here. After expansion (refer to Appendix B), Eqn. (3.13) can be written in terms of the LO frequency component and its harmonics as follows:

$$R = K_0 + K_1\cos(\omega_{lo}t) + K_2\cos(2\omega_{lo}t) + K_3\cos(3\omega_{lo}t) \qquad (3.14)$$

where the $K_n$ $(n=0,1,2,3)$ coefficients depend on $A_n$ $(n=0,1,2,3)$, $V_{dc}$ and $V_{lo}$ as follows:

$$K_0 = A_3 V_{dc}^3 + A_2 V_{dc}^2 + \left(A_1 + \frac{3}{2}A_3 V_{lo}^2\right)V_{dc} + A_0 + \frac{A_2 V_{LO}^2}{2}$$

$$K_1 = 3A_3 V_{lo}V_{dc}^2 + 2A_2 V_{lo}V_{dc} + \frac{3}{4}A_3 V_{lo}^3 + A_1 V_{lo}$$

$$K_2 = \frac{3}{2}A_3 V_{lo}^2 V_{dc} + \frac{1}{2}A_2 V_{lo}^2, \quad K_3 = \frac{1}{4}A_3 V_{lo}^3$$

The coefficients $K_n$ in the above expression are strongly dependent upon $V_{lo}$ in their increasing order and become less dependent on $V_{dc}$. It can be seen from Eqn. (3.14) that in the absence of LO modulation, $R$ turns out to be its dc equivalent value $R_{Vdc}$. The dynamic responsivity of the MSM-PD can be obtained from Eqn. (3.13) by taking the derivative of $R$ with respect to $V_{dc}$ and is given by

$$R_d = \{K_0' + K_1' \cos(\omega_{lo}t) + K_2' \cos(2\omega_{lo}t)\} \, Tanh \, [\alpha(V_{dc} + V_{lo}\cos(\omega_{lo}t))]$$
$$+ R\alpha \, sech \, (\alpha(V_{dc} + V_{lo}\cos(\omega_{lo}t)))^2$$

(3.15)

where the coefficients $K_n'$ $(n = 0, 1, 2)$ are the first derivatives of the coefficients $K_0, K_1, K_2$ with respect to $V_{dc}$ in Eqn. (3.14) and are given by

$$K_0' = 3A_3V_{dc}^2 + 2A_2V_{dc} + \left(A_1 + \frac{3}{2}A_3V_{lo}^2\right)$$

$$K_1' = 6A_3V_{lo}V_{dc} + 2A_2V_{lo}$$

$$K_2' = \frac{3}{2}A_3V_{lo}^2$$

The dynamic responsivity of the MSM-PD as shown in Fig. 3.6 can be used to explain the conversion loss and signal variations with respect to changes in its bias, which will be discussed in Section 3.5.

Based on the above model, the mixer can be further analysed in terms of its conversion loss and noise figure. The overall link quality can be described by its carrier-to-noise ratio.
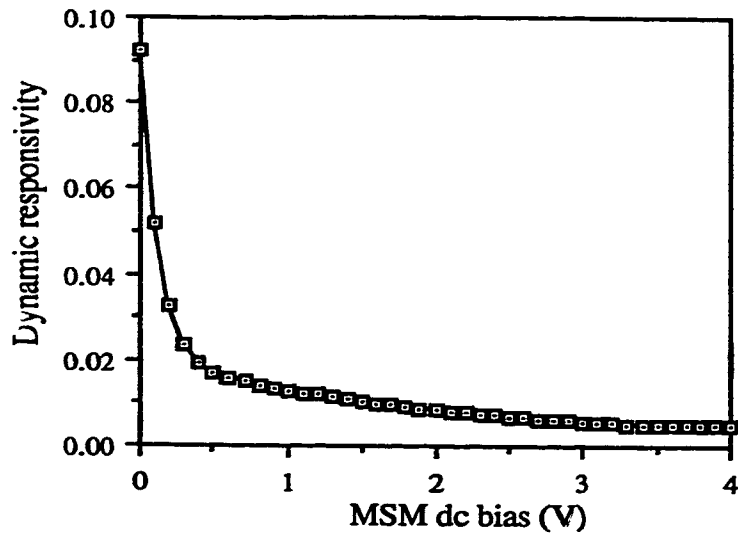
**Fig. 3.6 Dynamic responsivity of the MSM-PD vs dc bias**

## 3.4 System Performance

The overall system performance can be examined in terms of the carrier-to-noise ratio depending on the optical modulation index (*OMI*) which is restricted by the number of carriers being transmitted. In the present case, the *OMI* per channel can have a maximum depth of 50%. The overall link noise is mostly influenced by the laser relative intensity noise (*RIN*), intermodulation noise, the receiver shot noise and thermal noise. Various noises in the system can degrade the signal to noise ratio at the receiver and thus the link quality. The optical link must satisfy the dynamic range required by the overall system which is in turn dependent on the third order intermodulation distortion noise. Hence, it is necessary to examine the various sources of noise that influence the link carrier-to-noise ratio (*CNR*). The following noise components which are of relevance to our system analysis can be classified and considered.

## 3.4.1 Thermal Noise

Thermal noise is associated with the bias resistor in the photodetector and is due to the spontaneous fluctuations of the currents or voltages in the bias circuit. The mean square value of this noise current in a noise equivalent bandwidth $B$ is given by

$$< I_{th}^2 > \quad = \frac{4kTB}{R_b} \tag{3.16}$$

where $k$ is the Boltzmann's constant, $T$ is the absolute temperature and $R_b$ is the resistance in the bias circuit of MSM-PD, which are listed in Table 2 (p. 106).

## 3.4.2 Shot Noise

Shot noise is a result of the random arrival of the signal photons and also the dark current in the detector. It is proportional to the total detected photocurrent. Its mean square value is given by

$$< I_{sh}^2 > \quad = 2qI_{dc}B \tag{3.17}$$

$$I_{dc} = RP_f = R\beta P_o \tag{3.18}$$

where $P_f$ is the time invariant term of the received optical power at the input of the MSM-PD, $\beta$ is the link loss, $P_0$ is the optical power at the laser output and $q$ is the electron charge. The term $R$ in Eqn. (3.18) corresponds to $R_{Vdc}$ or $K_1$ in the absence and presence of LO modulation of the bias respectively.

## 3.4.3 Relative Intensity Noise

The apparent intensity noise at the receiver consists of noise intrinsic to the laser due to

39

quantum effects in electron to photon conversion, mode partitioning, and extrinsic effects such as reflection, scattering and dispersion. Reflection effects are more predominant when highly stabilized lasers are used in the long wavelength windows. In our case, the extrinsic effects are considered to be negligible. The mean square value of the equivalent intensity noise current is given by

$$< I_{RIN}^2 > \;=\; RINI_{dc}^2B \qquad\qquad (3.19)$$

where *RIN* is the relative intensity noise factor which takes into account the overall noise variations that occur at the transmitter end and $I_{dc}$ is as defined in Eqn. (3.18).

## 3.4.4 Intermodulation Noise

The nonlinearity of the laser diode characteristic can generate higher harmonic distortion signals as well as second and third order IMD products as explained in Sec. 3.2.1. When the two subcarrier frequencies $f_1$ and $f_2$ are closely spaced, the total currents due to inter-modulation noise can be calculated from the expression for the optical power *P*. The most important contributions to this noise result from the third-order IMD products. Since the second-order IMD products fall outside of the occupied frequency bands and can be filtered out by the harmonic rejection filter, they are not taken into consideration; hence we consider only third-order IMD into account. With the two carriers being spaced closely with respect to one another, the third order IMD noise generated by the $I^3$ term in Eqn. (3.7) degrades the system performance by limiting the overall link *CNR*. Thus the mean square value of the current associated with the IMD noise can be obtained from Eqns. (3.7) and (3.14) as:

40

$$<I_{im}^2> = \frac{1}{2}\left[\frac{9}{32}a_3^2 m^6\right] K_1^2 P_f^2 \qquad (3.20)$$

It can be seen from Eqn. (3.20) that the level of IM noise can be controlled by the variation of *OMI* per channel which is in turn dependent upon the RF source input power $P_{in}$.

## 3.5 Conversion Loss, CNR and Noise Figure

The MSM-PD optoelectronic mixer performance can be best described in terms of its conversion loss, and noise figure based on link $CNR$. The $CNR$ is defined as the figure of merit for the optical link and its variation with various receiver parameters is dealt with in detail in order to obtain optimized performance. Also, the OEM conversion loss is a significant parameter which enables us to estimate the level of the up-converted signal with respect to the incoming optical signal. The noise figure of the OEM is another important parameter which is defined in terms of the link $CNR$. These issues are examined in detail to obtain an insight into the system characteristics with respect to parametric variations. The following analysis will be supplemented with experimental investigations in Chapter 4 to understand the physical significance and limitations of the proposed system.

## 3.5.1 Conversion Loss

In order to obtain the OEM conversion loss, the signal variations need to be analysed taking into account the LO modulation of the dc bias. The photocurrent at the detector output with two RF subcarriers on the optical signal is given by

$$I_{ph} = RP_f(1 + m[\cos(\omega_1 t) + \cos(\omega_2 t)]) \qquad (3.21)$$

where the parameters are defined as earlier. The conversion loss of the mixer is defined as the ratio of the mean square variances of the upconverted signal (with LO modulation) to the input signal (without LO modulation) and can be expressed as:

$$L_c = \frac{<I_{up}^2>}{<I_{in}^2>} \qquad (3.22)$$

where $<I_{in}^2>$ is dependent upon the dc-responsivity $R_{Vdc}$ and $<I_{up}^2>$ depends on the mixing responsivity $K_1$ associated with the frequency upconverted signal. Thus, the mean square value of the input signal current can be defined as:

$$<I_{in}^2> = \frac{1}{2}m^2R_{Vdc}^2P_f^2 \qquad (3.23)$$

The mean square value of the upconverted signal current is given by

$$<I_{up}^2> = \frac{1}{8}m^2P_f^2K_1^2 \qquad (3.24)$$

Hence, $L_c$ can be found as a ratio of Eqns. (3.23) and (3.24) and can be expressed as:

$$L_c = \frac{K_1^2}{4R_{Vdc}} \qquad (3.25)$$

Thus it can be seen from Eqn. (3.25) that the OEM conversion loss increases with $K_1$ due to its increase with bias and also because of its inverse relationship with $R_{Vdc}$. The conversion loss as a function of dc bias for varying values of LO voltages is shown in Fig. 3.7.
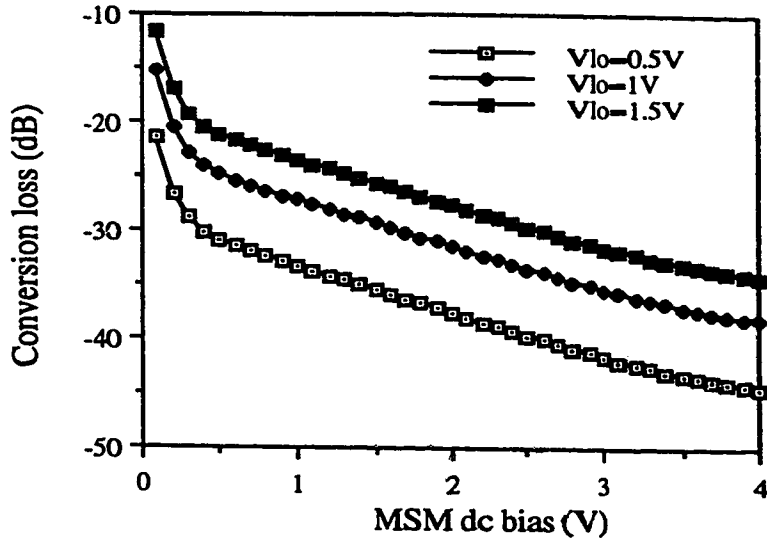
**Fig. 3.7 OEM conversion loss as a function of dc bias**

It can be seen that the conversion loss is quite low at low bias and increases with increasing bias. This is because in the low bias region the upconverted signal level depends strongly on the voltage applied to the MSM, leading to large dynamic responsivity whereas in the high bias region the dynamic responsivity is very low because the dependence of the response on applied voltage is saturated. As the LO amplitude increases, the upconverted signal level increases whereas the input signal is unaffected by changes in $V_{lo}$. Also, $K_1$ in Eqn. (3.25) increases with $V_{lo}$ at fixed bias (but is quite small compared to $R_{Vdc}$) and hence the conversion loss decreases as $V_{lo}$ is increased. To examine this effect, the variation of the loss against $V_{lo}$ is shown in Fig. 3.8 for two different bias regimes, i.e. 0.5V (low bias) and 4V (high bias). The loss decreases with an increase in $V_{lo}$. Thus the mixing process is quite effective in the low bias region with a large LO volt-

age amplitude. A conversion loss of about 22 dB is obtained for the OEM with $V_{dc}$=0.5 V and $V_{lo}$=1.5 V.
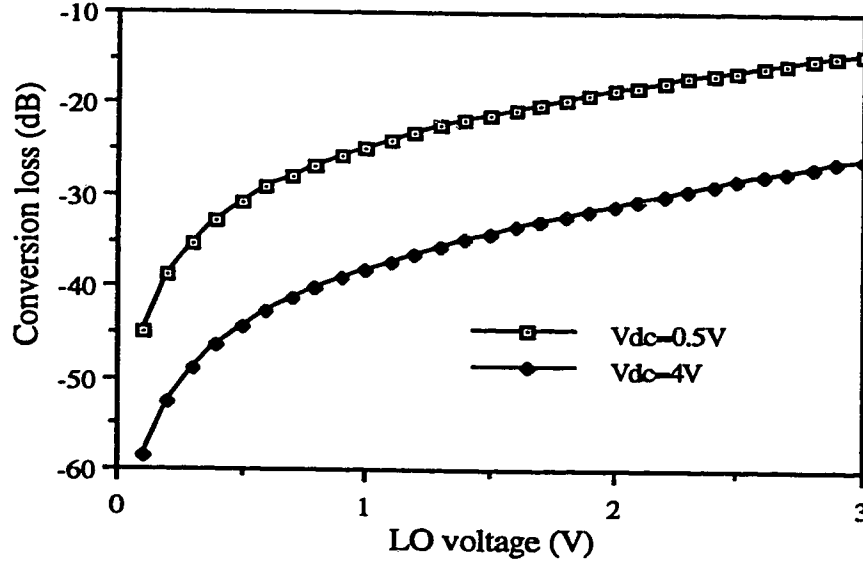


**Fig. 3.8 OEM conversion loss as a function of LO voltage**

## 3.5.2 Carrier-to-Noise ratio

The quality of a directly modulated FO link can be evaluated in terms of $CNR$. Here, the $CNR$ of the upconverted and the input signals is defined as the ratio of the mean square value of the signal and noise currents in the presence and absence of the LO modulation. Thus, the $CNR$ of the upconverted signal in terms of the various noise sources is given by

$$CNR_{up} = \frac{<I^2_{up}>}{<I^2_{th}> + <I^2_{RIN}> + <I^2_{sh}> + <I^2_{im}>} \qquad (3.26)$$

The first term in the denominator of Eqn. (3.26) represents the receiver thermal noise, the

44

second term is the relative intensity noise of the laser diode, the third term is the receiver shot noise, and last term is the degradation due to intermodulation distortion. In order to examine the intermodulation noise effects on the system $CNR$, we consider the carrier-to-intermodulation ratio at the link output, which can be obtained from Eqns. (3.20) and (3.24) as:

$$CIR = \frac{<I_{up}^2>}{<I_{im}^2>} = \frac{8}{9a_3^2 m^4} = \frac{2R_{ld}^2 (I_b - I_c)^4}{9a_3^2 P_{in}^2} \qquad (3.27)$$

Thus it can be seen from Eqn. (3.27) that the $CIR$ decreases with increasing input power and is higher for large bias currents. The numerical result of calculating $CNR_{up}$ as a function of $OMI$ is shown in Fig. 3.9.
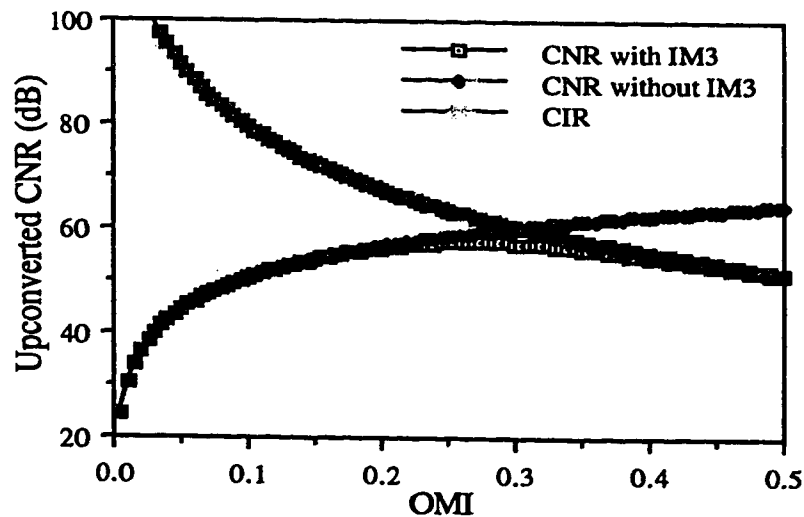


**Fig. 3.9 CNR of the upconverted signal against optical modulation index variations**

It can be seen from Fig. 3.9 that for lower values of $OMI$, where the degradation due to

IMD is negligible, the $CNR_{up}$ is limited by the thermal noise and can be improved as the value of $OMI$ is greater. In contrast, for relatively large values of $OMI$, IMD is dominant, and $CNR_{up}$ is degraded mainly due to IMD. Thus there exists an optimum value of $OMI$ for which the $CNR_{up}$ can be maximized.

The $CNR$ of the input signal in the absence of the LO modulation is defined as

$$CNR_{in} = \frac{<I_{in}^2>}{I_{RIN}^2> + <I_{im}^2>}$$  (3.28)

In Eqn. (3.28) the $RIN$ parameter takes into account the overall noise variations that occur at the transmitter end. The $CNR$ of the input and upconverted signals for a single channel system in a 10 kHz bandwidth as a function of dc bias are shown in Fig. 3.10.
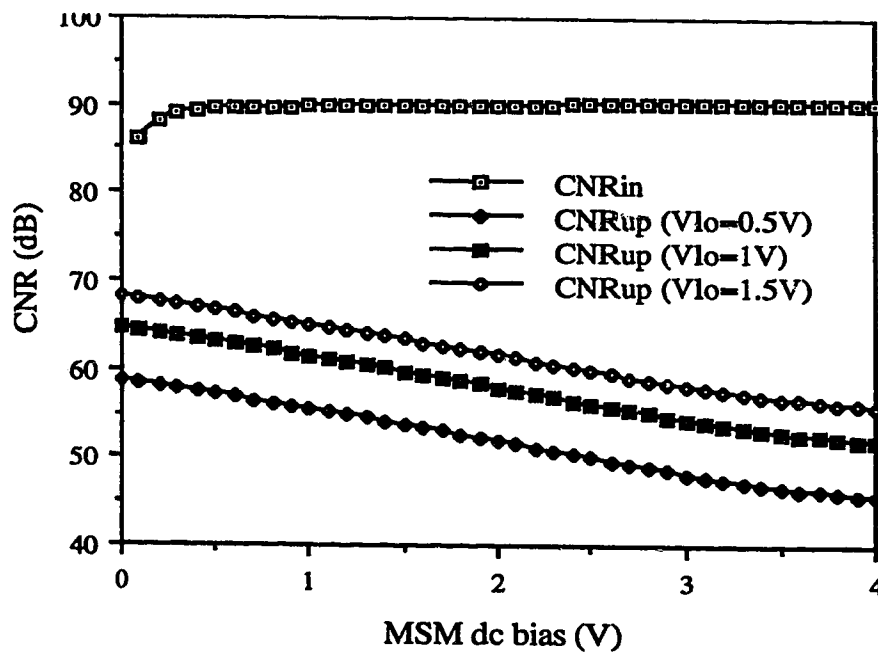
Fig. 3.10 CNR of the input and upconverted signal vs MSM dc bias

It can be seen that the input signal $CNR$ increases with $V_{dc}$ to a certain extent beyond which it saturates for any further increase in the bias. This can be explained in terms of the dc responsivity which increases sharply in the low bias region but saturates when the bias is increasingly high. The upconverted signal $CNR$ is maximum at zero bias because of the lower conversion loss but decreases with an increase in dc bias due to the increasing mixer loss. Also, it can be noted from Eqn. (3.26) that the $CNR_{up}$ is limited by the receiver thermal noise at lower values of $P_f$ and increases as a function of the LO voltage due to the $K_1$ dependence on $V_{lo}$ as explained above. At higher powers, the shot noise and the laser noise become more predominant and thus the $CNR_{up}$ follows linearly with $P_f$. This is shown more explicitly in Fig. 3.11 where the $CNR_{up}$ rises steadily with LO voltage.
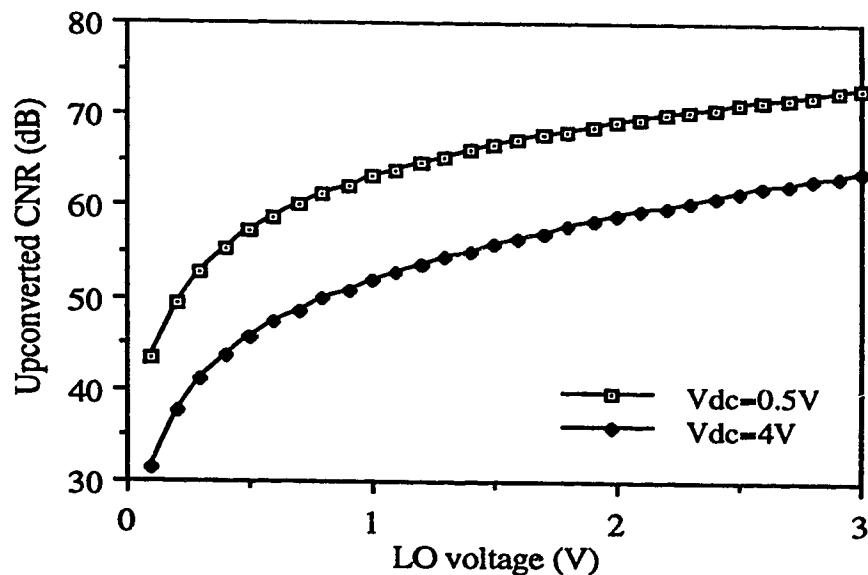


**Fig. 3.11 CNR of the upconverted signal against LO voltage**

Fig. 3.12 shows the $CNR_{up}$ as a function of dc bias for in a two channel system with var
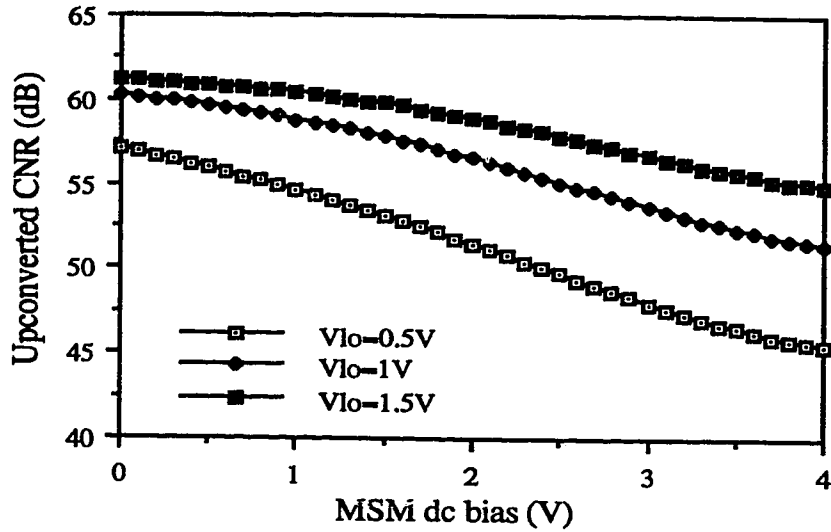
**Fig. 3.12 CNR of the upconverted signal vs bias in a 2-channel SCM system**

iations in the LO voltage. It can be seen that the $CNR_{up}$ in a 2-channel case is maximum at zero bias and decreases slowly with increasing bias. This is due to the dominance of the receiver thermal noise in Eqn. (3.25). As $V_{lo}$ increases, the IM noise increases and tends to be dominant in the low bias region. Thus, for higher values of $V_{lo}$, the $CNR_{up}$ in the low bias region is limited by the IM noise performance of the LD whereas in the high bias region, thermal noise remains to be the dominant source. Also, as explained earlier, the $CNR_{up}$ increases with increasing $V_{lo}$ and saturates beyond 1.5 V. Similar variations of $CNR_{up}$ with LO voltage are shown in Fig. 3.13 for a dc bias of 0.5 V and 4 V. It can be seen from Fig. 3.13 that the $CNR_{up}$ decreases with increasing bias and also saturates accordingly with $V_{lo}$ as explained above. Thus it can be seen from Figs. 3.12 and 3.13 that the $CNR_{up}$ is sensitive to the variations in $V_{dc}$ and $V_{lo}$.

In a 2-channel system affected by IMD, the $CNR_{up}$ increases linearly with $V_{lo}$ due to its thermal noise dominance and then saturates due to the degradation caused by IMD. Thus by proper choice of OMI, $V_{dc}$ and $V_{lo}$, it is possible to obtain values for the $CNR$ that could meet a given system specifications. A $CNR_{up}$ of about 61 dB could be obtained with an *OMI* of 0.27, $V_{dc}$=0.5V and $V_{lo}$=1.5 V respectively. The theoretical results presented here will be supported by experimental investigations in Chapter 4.
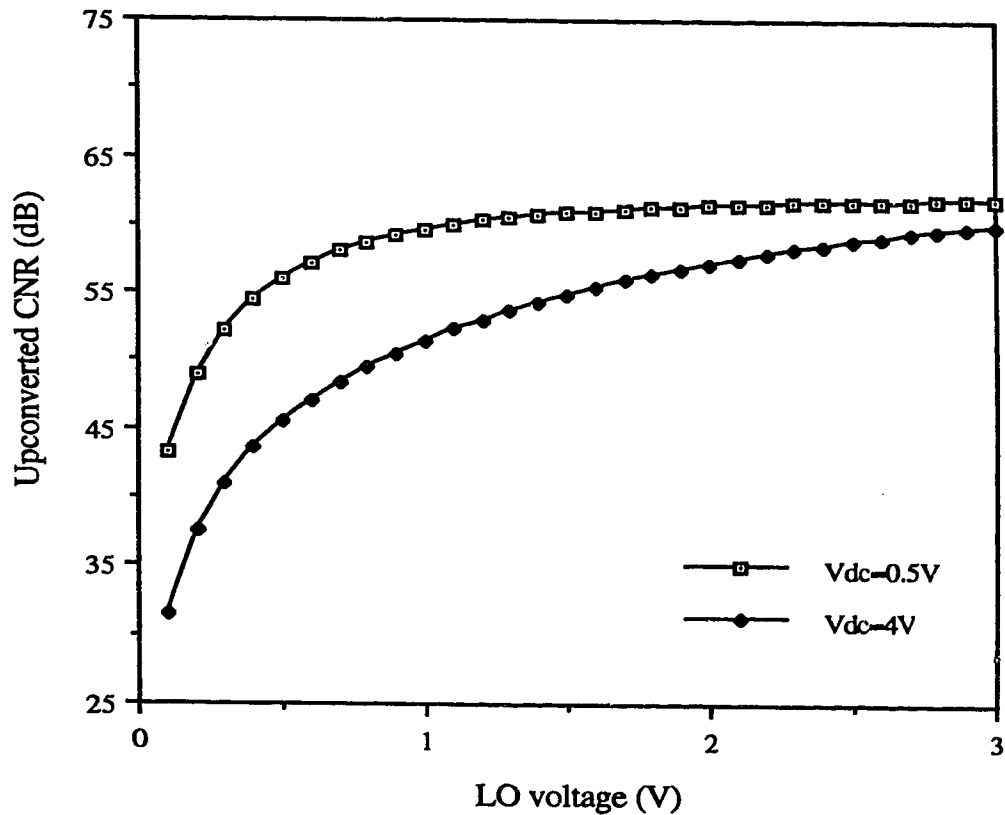


**Fig. 3.13 CNR of the upconverted signal vs LO voltage in a 2-channel SCM system**

### 3.5.3 Noise Figure

Having defined the link $CNR$, the noise figure of the mixer is defined as the ratio of the $CNR$ of the input signal to the detector to the upconverted signal $CNR$ and can be expressed as:

$$F_n = \frac{CNR_{in}}{CNR_{up}} = \frac{1}{4L_c}\left[\frac{\frac{4kTB}{R_b} + 2qK_1P_fB + RINK_1^2P_f^2B + \frac{9}{64}a_3^2m^6K_1^2P_f^2}{RINR_{Vdc}^2P_f^2B + \frac{9}{64}a_3^2m^6R_{Vdc}^2P_f^2}\right] \tag{3.29}$$

As in the case of conversion loss, the noise figure in Eqn. (3.29) is dependent upon the dc-bias, LO amplitude and also the carrier $OMI$.

The noise figure variations as a function of the dc bias, in a single channel and 2-channel SCM system, for varying LO voltages is shown in Fig. 3.14 and Fig. 3.15 respectively. It can be seen that the noise figure increases with increasing bias because of the rise in the input signal $CNR$ and also due to the lowering of the upconverted signal $CNR$. The noise figure variation as a function of $V_{lo}$ is illustrated in Fig. 3.16 and Fig. 3.17 and it decreases with increasing LO voltage due to the increase in the upconverted $CNR$. The saturation effects of noise figure with increasing $V_{lo}$ in the 2-channel case could be attributed to the variations of $CNR_{up}$ as explained earlier.

In order to understand the relationship between OEM noise figure and optical power, the noise figure variations have been obtained as a function of optical power incident on the MSM-PD in a single channel system. With increasing optical power, the noise figure of

the mixer at a fixed $V_{dc}$ was found to decrease continuously as illustrated in Fig. 3.18. In

Fig. 3.19, the noise figure is plotted as a function of optical power at fixed $V_{lo}$. In both

cases the noise figure decreases with increasing power. This is because at low $P_f$, the

noise figure is mainly influenced by the receiver thermal noise in case of upconverted sig-

nal and input signal shot noise whereas at higher values of $P_f$, the shot noise of the upcon-

verted signal and laser noise of the input signal become dominant. Hence it is evident

from Eqn. (3.29) that the OEM noise figure falls off with $P_f$. With $V_{dc}$=0.5 V, $V_{lo}$=1.5 V

and $P_f$=0 dBm, a noise figure of 23 dB could be obtained for the OEM. In a 2-channel

system, the noise figure is obtained as a function of *OMI* as shown in Fig. 3.20 for two dif-

ferent bias regimes, i.e. 0.5V (low bias) and 4V (high bias). It can be seen from Fig. 3.20

that lower values of noise figure can be obtained with lower values of dc bias as explained

above.
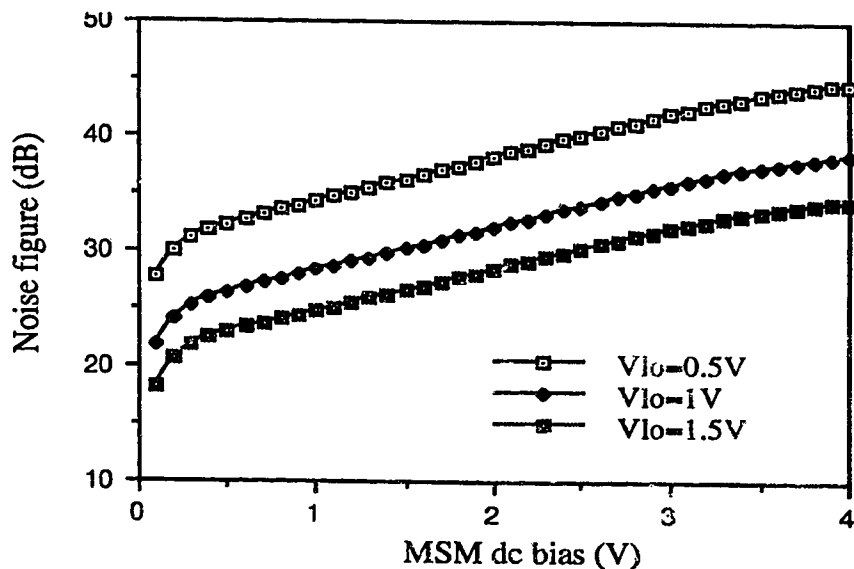


Fig. 3.14 Noise figure of the OEM vs dc bias in a single channel system

51
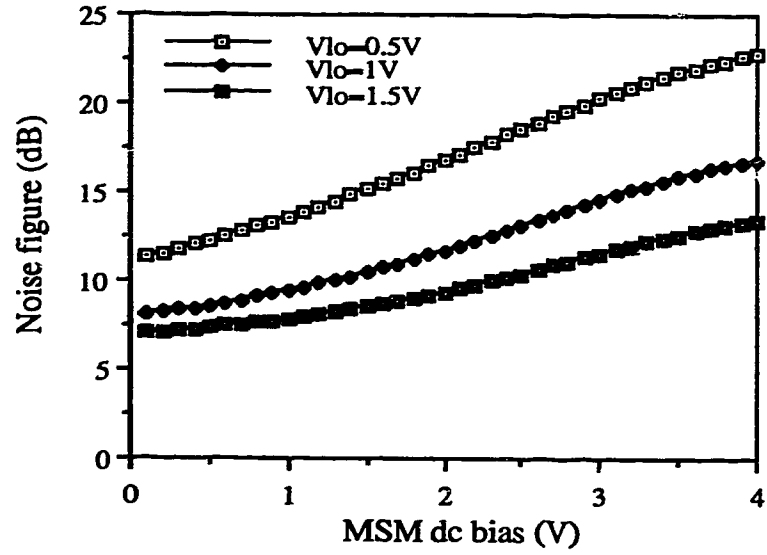
**Fig. 3.15 Noise figure of the OEM vs dc bias in a 2-channel SCM system**
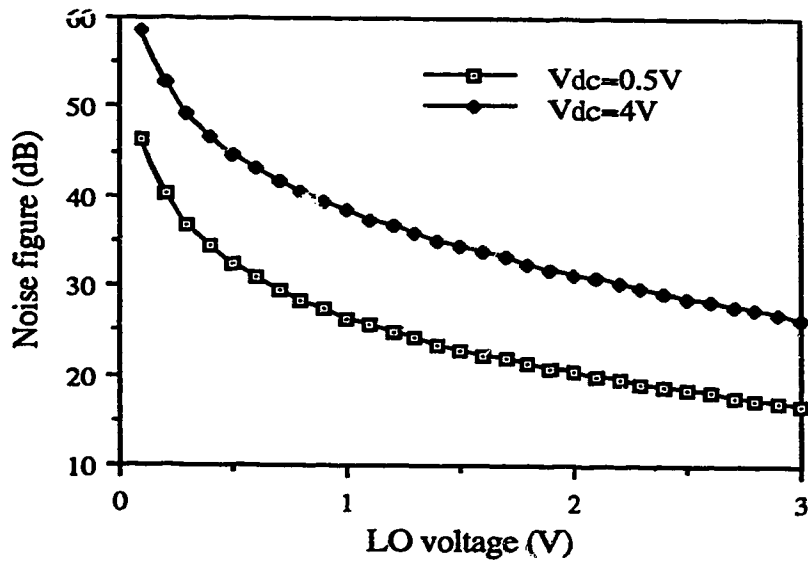


**Fig. 3.16 Noise figure of the OEM vs LO voltage in a single channel system**
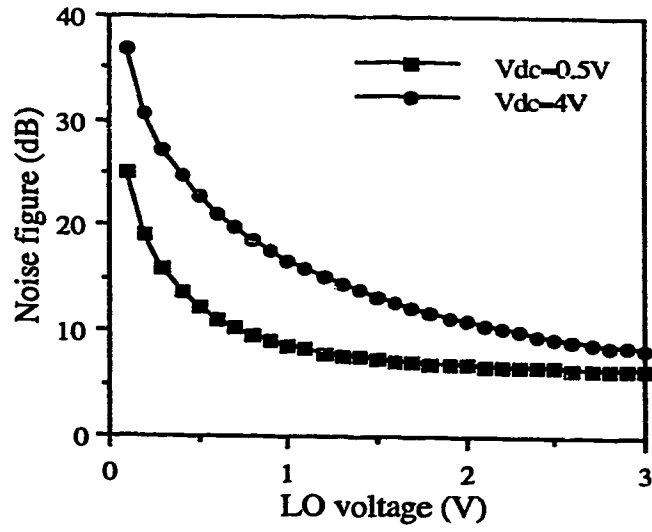
**Fig. 3.17 Noise figure of the OEM vs LO voltage in a 2-channel SCM system**
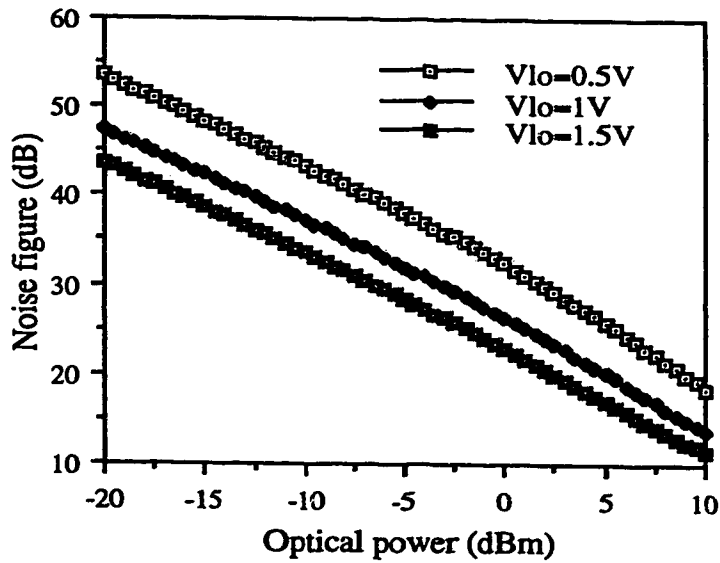


**Fig. 3.18 Noise figure of the OEM vs optical power variations at a bias of 0.5V**
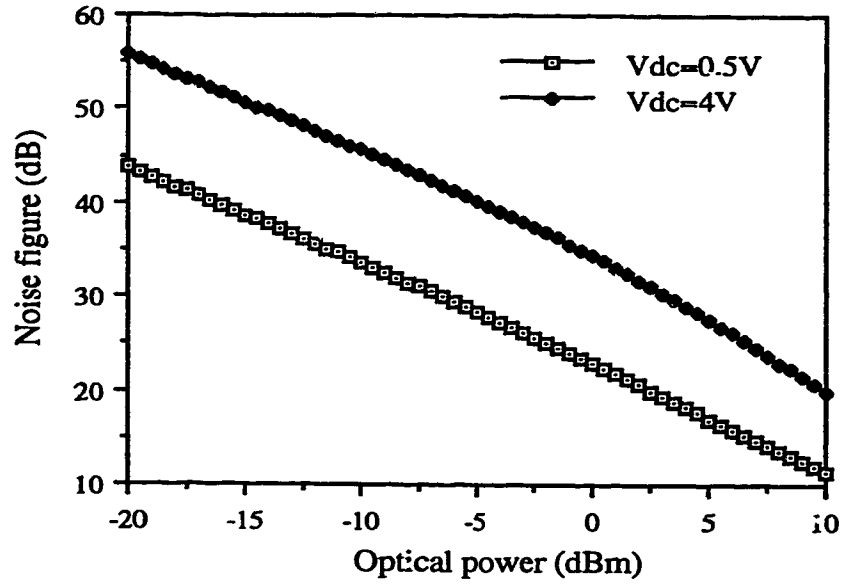
**Fig. 3.19** Noise figure of the OEM vs optical power variations at a LO of 1.5V
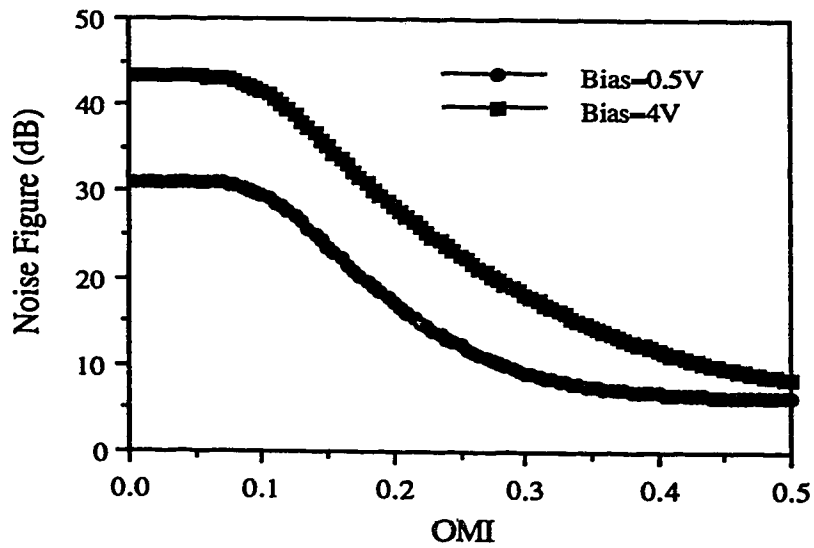


**Fig. 3.20 Noise figure vs OMI in a 2-channel SCM system**

In this case, the noise figure is limited by thermal noise of the upconverted signal at lower values of *OMI* but falls off rapidly due to the IMD noise dominance of the input signal at higher levels of *OMI*. Thus by controlling the *OMI* parameter, it is possible to maintain the OEM noise figure to a much lower value.

Thus it follows that the lower values of the OEM noise figure at relatively higher power levels with low dc bias and high LO voltage amplitude make its operation more effective in radio base stations. The analysis presented above is supplemented with experimental results in the next chapter and the practical limitations of the proposed system are detailed.

# 4. EXPERIMENTAL RESULTS

This chapter presents experimental results on the SCM transmission of radio subcarriers over a fiber optic link. First the laser diode transfer characteristics are obtained in terms of the optical output power as a function of the bias current. The MSM-PD is then characterised in terms of its frequency response and the mixing responsivity. The performance of the optical link using optoelectronic upconversion is evaluated by considering single channel and two-channel SCM radio transmission over the fiber optic link, in terms of the *CNR*.

## 4.1 Laser Diode characteristics

A GaAs-AlGaAs semiconductor laser diode (LD) emitting at a wavelength of 780 nm with a rated power output of 5 mW at an operating temperature of 25 °C was used in this experiment. The laser had a threshold current of about 37 mA. The static nonlinearities inherent in the laser light curve characteristic limits the performance of the LD's modulation capability. In order to obtain a better performance, the laser was operated at a high bias well beyond the threshold in its linear region. By varying the laser bias current, the IM distortion resulting from the above nonlinearity could be maintained within acceptable limits.

## 4.2. MSM-PD characteristics

A monolithic integrated GaAs MSM-PD was used as an OEM in this experiment. The GaAs MSM used in this project was a single element of a 1x8 linear array of MSM detectors. The GaAs MSM array chip, made by Bell-Northern Research (BNR), contains eight $100 \times 100 \ \mu m^2$ MSMs with 1 $\mu m$ wide fingers and 3 $\mu m$ between adjacent fingers, spaced

250 μm apart, with a common connection joining one terminal of each of the MSMs together. Such arrays find potential use in very high speed optoelectronic switching or signal processing. The physical layout of these MSM arrays is depicted in Fig. 4.1 below.
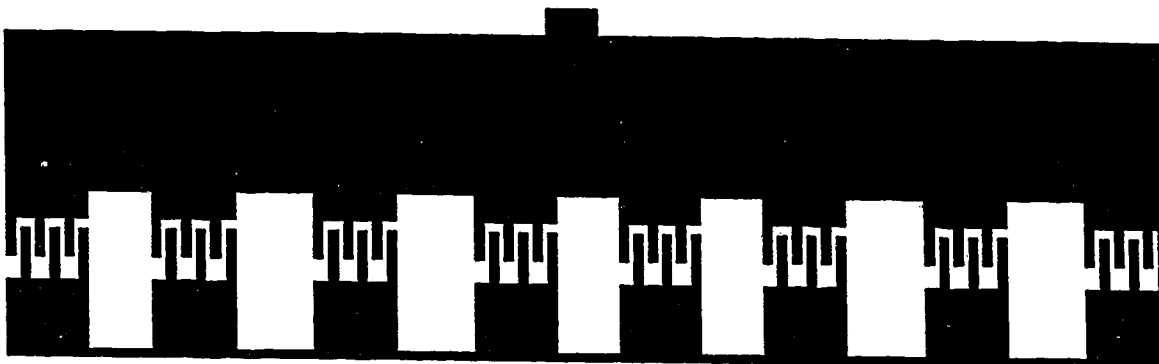


**Fig. 4.1 BNR's 1x8 GaAs MSM array**
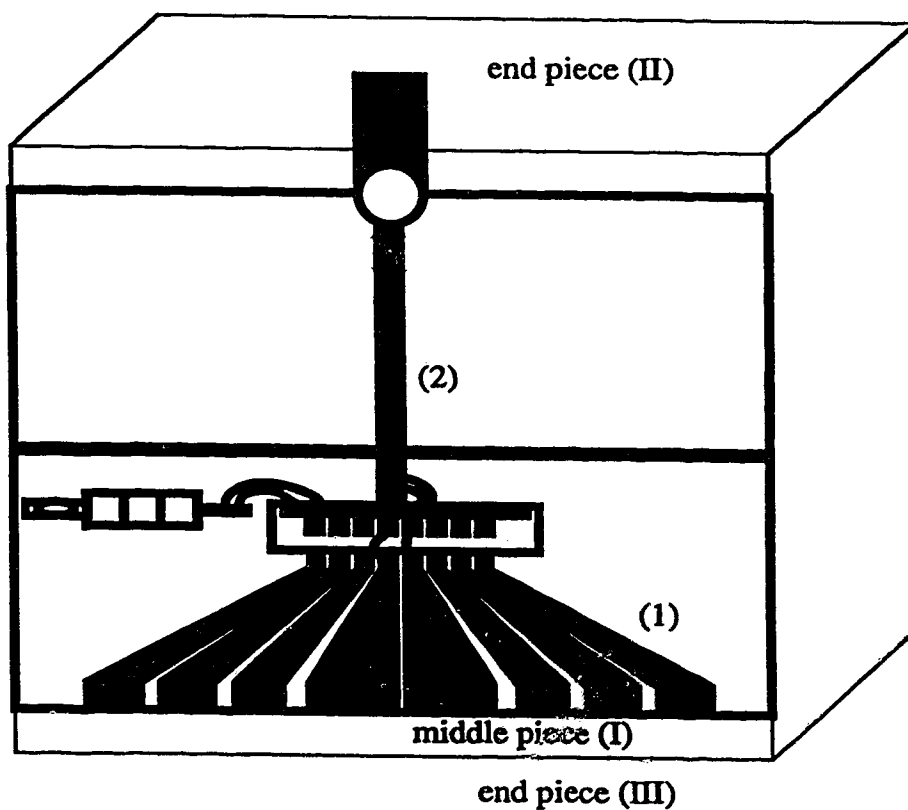


**Fig. 4.2(a) Aluminium package for the MSM-PD transceiver (middle/end pieces)**

from laser

top piece IV

fiber

light

1x8 MSM array
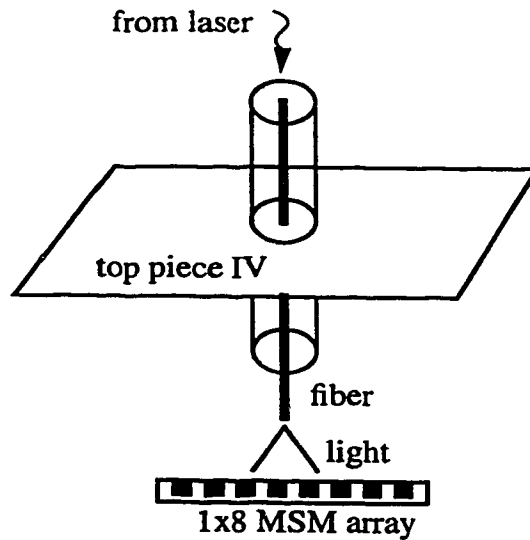
**Fig. 4.2(b) Aluminium package for the MSM-PD transceiver (top piece)**

## 4.2.1 Aluminium Package for the MSM-OEM

An aluminium package was designed for the OEM receiver in order to carry out the test measurements. This package was assembled from four pieces as shown in Fig. 4.2(a) and Fig. 4.2(b). An alumina substrate on which the MSM array is mounted fits on the floor of the large middle piece indicated as I in Fig. 4.2(a). On the alumina substrate there are eight bias lines labelled (1) which lead to the individual MSM pads through gold bond wires.

Two of the 8 detectors in the 1x8 array were used for experimental results. A 50 $\Omega$ microstrip trace on a second substrate labelled (2) is connected to the common MSM strip through two gold bond wires. The two alumina substrates were fixed with screws on the middle piece. Both the ends of the middle piece were connected through conductive epoxy to two gold-plated female SMA connectors that fit into the two end pieces labelled II and

III respectively. Also connected to the common MSM strip is a pair of gold wires leading to a 270Ω resistor which is then grounded through a via hole. This provides a DC path to ground for the MSM bias voltages. The IVth piece that holds the fiber positioner, as shown in Fig. 4.2(b), sits on the top of the middle piece I and all the four pieces when screwed together properly form a rectangular box that is portable and flexible for measurement purposes. This arrangement is shown in Fig. 4.3. Preliminary characterization of the OEM in the test jig was done by measuring its frequency response to a high frequency intensity modulation optical signal. The high frequency responsivity of the MSM-PD was measured as a function of its bias variations. The measured results using the test jig are explained in Sections 4.2.2 and 4.2.3.
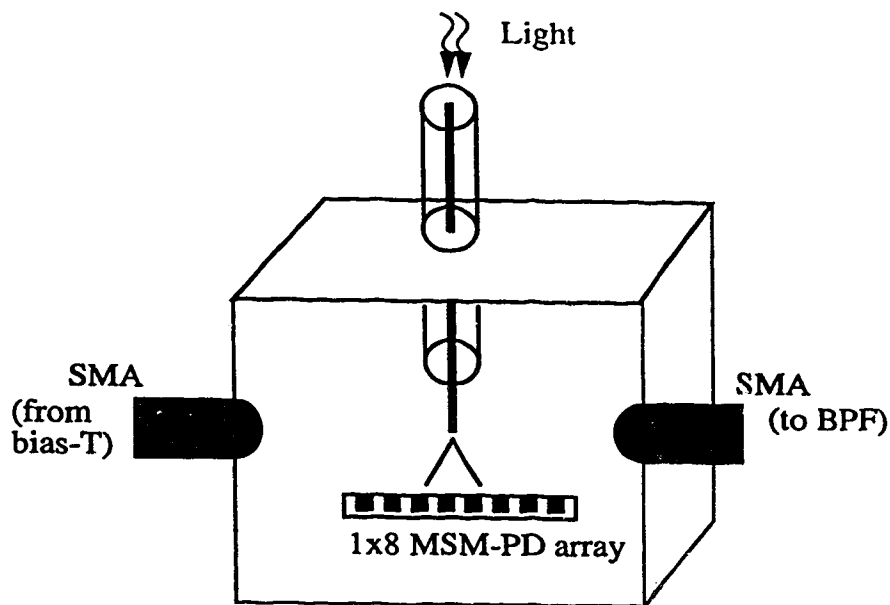
Fig. 4.3 Packaged MSM-PD based OEM for test measurements

## 4.2.2 Frequency Response

Characterization of a device as a function of modulation frequency provides valuable insight into how it will perform in both analog and digital systems. Hence the detector was characterised in terms of its frequency response using the experimental setup at TR Labs [51], by Ray Decorby at Saskatoon. The block diagram of the test facility used to study su .₁ high speed photodetectors is as shown in Fig. 4.4. The results are obtained in the frequency domain with the help of a HP 8510 vector network analyser. The network analyser performs a linear analysis on one or two port systems using a standard microwave scattering parameter model. With its attached test set, it has a frequency range from 45 MHz to 26.5 GHz, although the external optical modulator available has an upper limit of 18 GHz.

```
┌─────────────────────────┬─────────────────────────┐
│    network              │         RF              │
│    analyser             │       source            │
├─────────────────────────┴─────────────────────────┤
│              S parameter test set                  │
└────────────────────────────────────────────────────┘
```

| | |
|---|---|
| amplifier | |

temperature stabilized laser source → electro-optic modulator → MSM-PD / test jig and bias circuitry

─ · — · ─  electrical signal path

∿∿➤  optical signal path
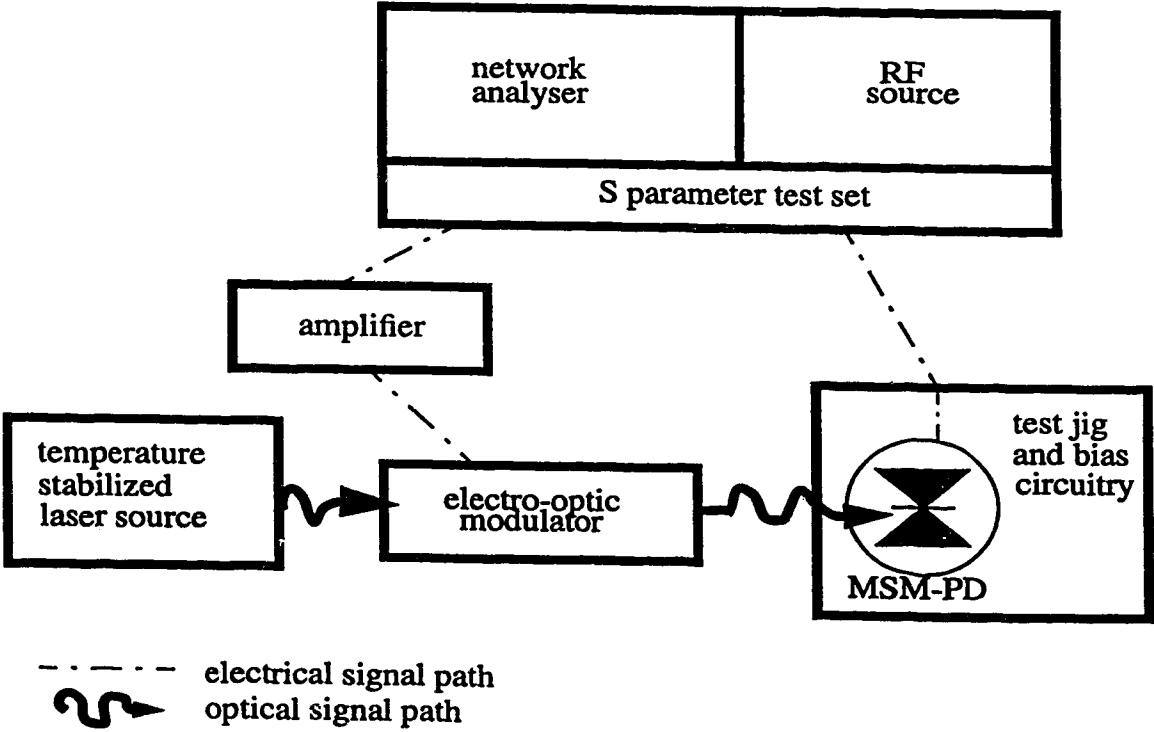
**Fig. 4.4 Block diagram to study the MSM-PD**

The complete test system is shown in Fig. 4.5. Most of the components were mounted on a steel optical breadboard. Light from a temperature stabilized laser source is incident on the Mach-Zehnder electro-optic modulator (EOM) which is suitably biased externally. The power input to the EOM is obtained through an amplified signal from the input port of a network analyser. The intensity modulated output is incident on the MSM-PD and the resulting electrical response is measured at the second port on the network analyser. The optical power incident on the MSM-PD is maintained at approximately 0.5 mW by monit-
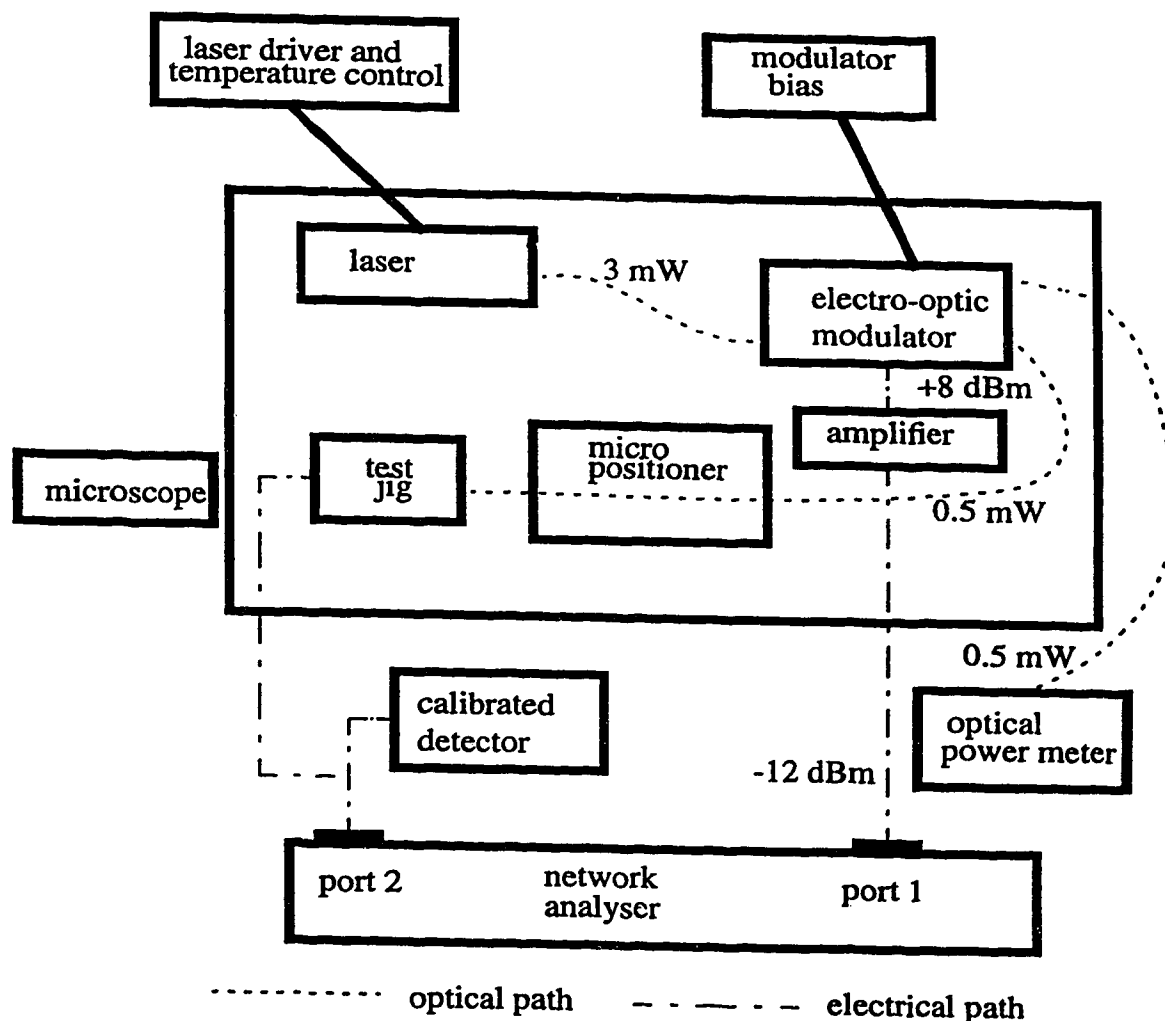


Fig. 4.5 Complete Test System for frequency response measurement

oring the other output of the EOM with the help of an optical power meter. The overall system was calibrated with a commercial wideband detector having a responsivity of 0.13 A/W. In order to obtain a better response characteristic, the detector was suitably biased at a fixed optical power level. The frequency response of the MSM-PD under a dc bias of 5 V and an optical power of 1.8 mW was obtained as shown in Fig. 4.6 and the 3 dB bandwidth is found to be 3 GHz. These results indicate the possibility of mixing at high frequencies using the MSM-PD [8].

## 4.2.3 Responsivity

The responsivity of the MSM-PD as a function of applied bias voltage was obtained experimentally at a fixed optical incident power of 430 $\mu$W. The dc-responsivity characteristics of both the detectors in the 1x8 MSM array is shown in Fig. 4.7.

The mixing responsivity was obtained by modulating the dc bias on the MSM with a 0 dBm electrical LO signal at 1.65 GHz and is shown as a comparison with the dc-responsivity (without LO) in Fig. 4.8. Based on the above results, a polynomial fit was obtained for the responsivity as described in Sec. 3.2. It can be seen from Fig. 4.8 that the mixing responsivity is low for lower values of bias and increases linearly with an increase in the bias up to 1.5 V and attains a saturation with further increase in the bias due to velocity saturation effect. Thus efficient mixing could be obtained by controlling the bias in the linear region and as a consequence, almost all the power in the optical signal is converted to the sum and difference frequencies.

S21 & M1        log MAG
REF 0.0 dB
2       5.0 dB/
∇    -3.1534 dB



START    0.045000000 GHz
STOP    10.000000000 GHz
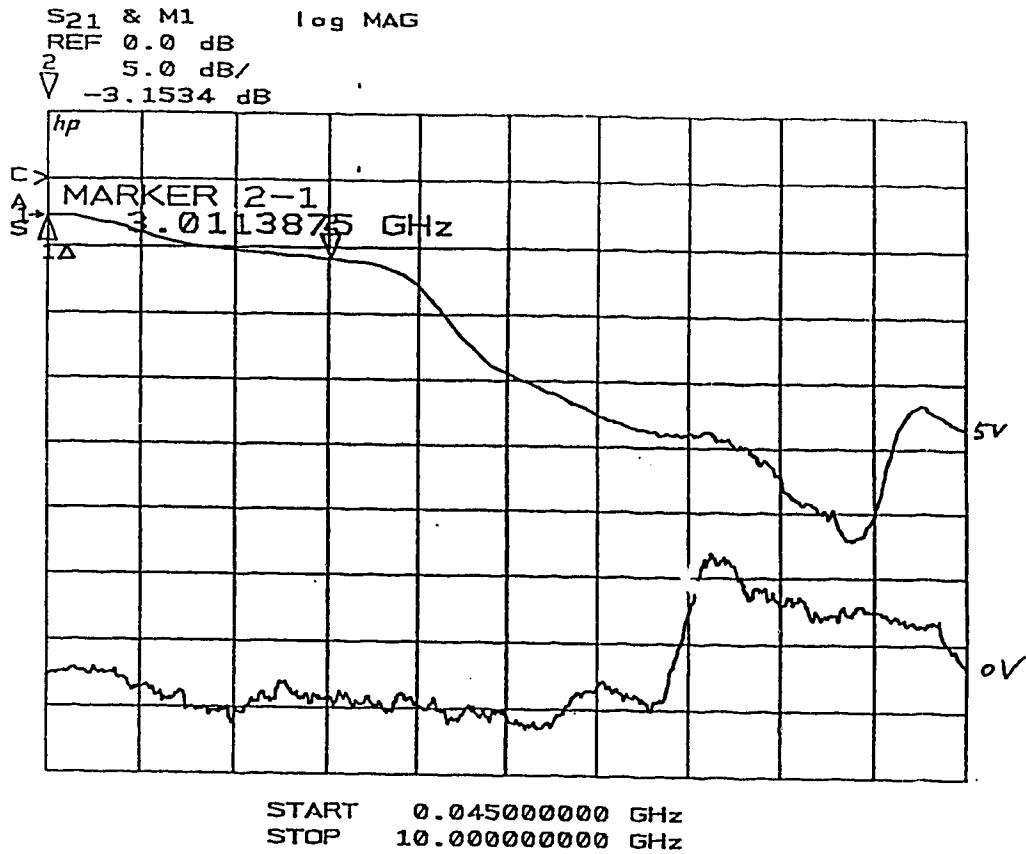
**Fig. 4.6 Measured frequency response of the MSM-PD**
**(MSM dc bias= 5 V, Popt=1.8 mW)**
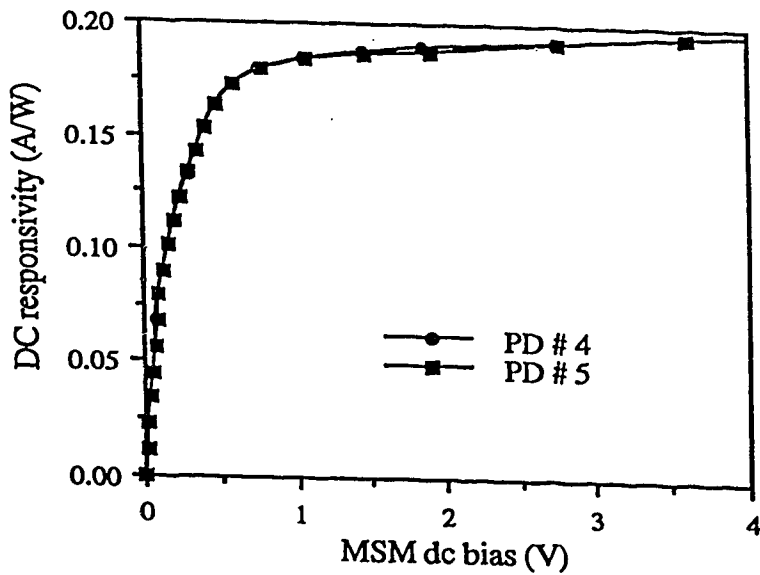


**Fig. 4.7 Measured DC responsivity of the MSM-PD vs bias**

63
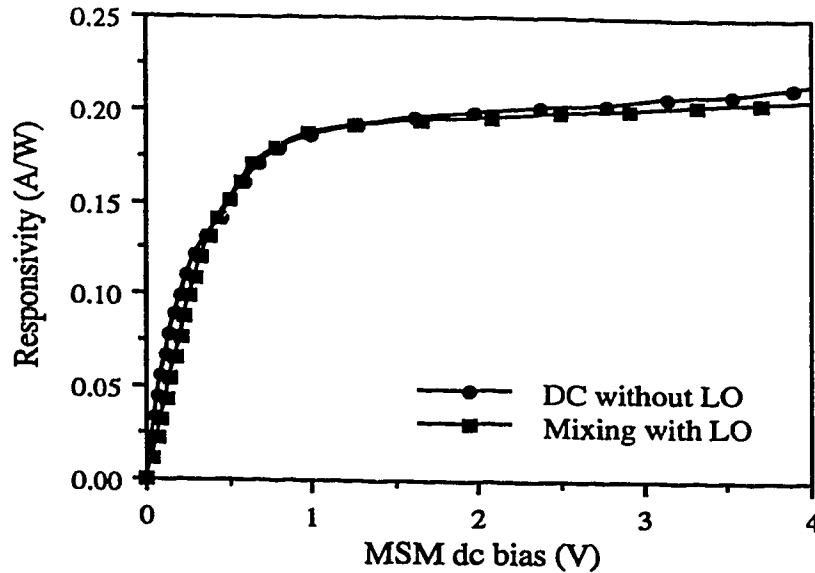
**Fig. 4.8 Responsivity of the MSM-PD vs dc bias
(DC and Mixing comparison)**

## 4.3 Single channel transmission

This section presents the results on the performance of the OEM in a single channel radio subcarrier transmission over a fiber optic link. The experimental setup for this demonstration is shown in Fig. 4.9. The LD in the CS is driven by a 0 dBm input RF signal at 150 MHz from a HP 8642A signal generator. The laser was biased at 44.3 mA and the output power at the fiber end was 430 mW. The intensity modulated optical signal thus generated is transmitted along a short length of multimode fiber to an optical receiver in the BS. The incoming optical signal and a 0 dBm electrical LO signal at 1.65 GHz form the two inputs to the OEM in the BS. The MSM-PD was dc biased to 0 V and the LO signal was obtained from a HP 8753A Network Analyser.

HP 8642A
Signal
Generator

LD

Optical fiber

OEM

A

BPF

B

G1

G2

C

LO (HP 8753A)

Spectrum
Analyser
HP 7000A
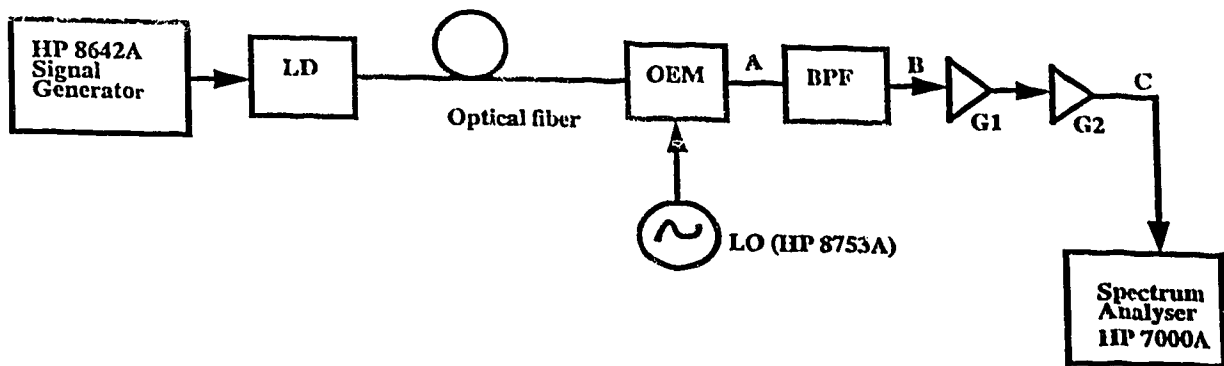
**Fig. 4.9** Directly Modulated fiber optic link based on an OEM

RL -10.00 dBm          MKR #1△FRQ 150.0 MHz

*ATTEN 0 dB                              -14.70 dB
10.00 dB/DIV

MARKER △                                 POS PK

150.0 MHz
-14.70 dB

1

START 1.250 0 GHz          STOP 2.050 0 GHz
*RB 300 kHz    *VB 10.0 kHz    ST 800.0 msec
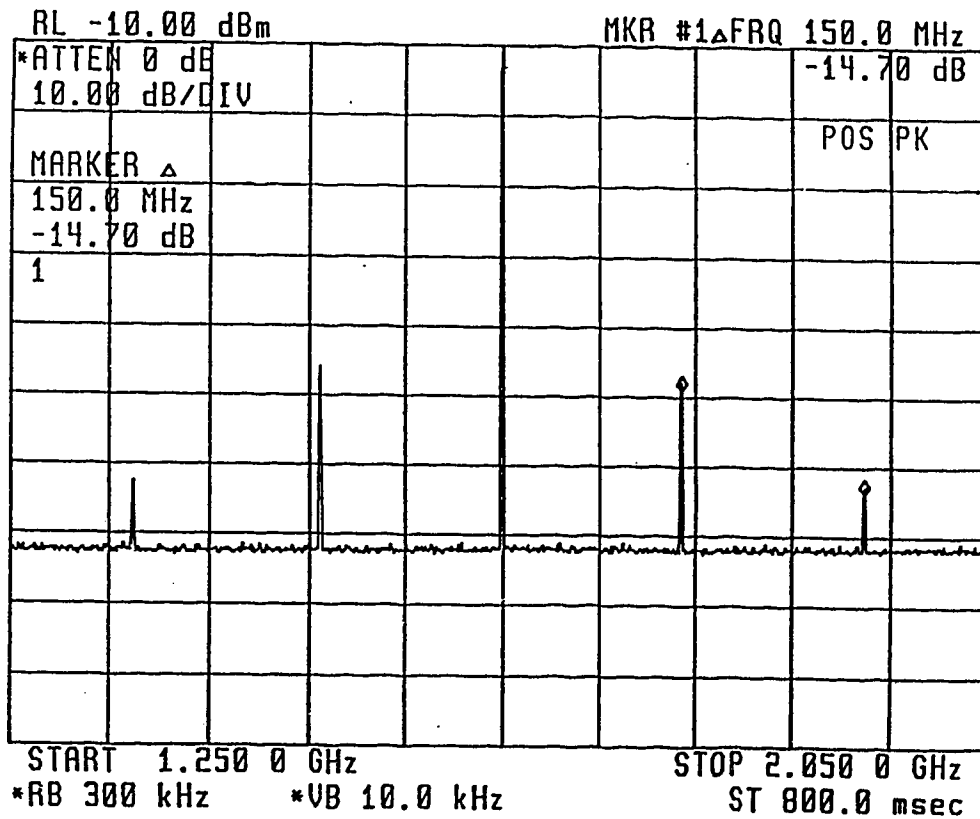
**Fig. 4.10** Measured spectrum of the signals at the OEM output

The frequency spectrum of the measured signals at the OEM output is shown in Fig. 4.10. The spectrum at the OEM output consists of the LO frequency (1.65 GHz), frequency up/down-converted signals (1.8/1.5 GHz), LO harmonics (3.3 GHz, 4.95 GHz, etc.) and associated frequency components. The LO power fed through is much higher than that of the converted frequencies. It can be seen from Fig. 4.10 that the upconverted signal level is about -58 dBm and the signal to noise ratio in a 300 kHz noise bandwidth is about 25 dB. The effect of laser bias current variation on the up/down-converted signals is obtained by plotting the measured values of the signal powers (at Point B in Fig. 4.9) against the incident optical power as shown in Fig. 4.11.
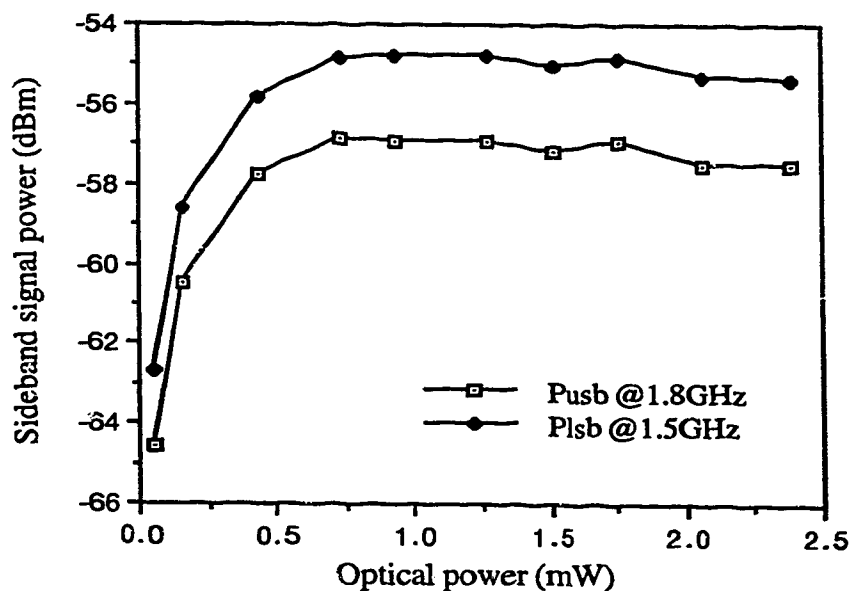


**Fig. 4.11 Measured output sideband signal powers vs incident optical power**

It can be seen from Fig. 4.11 that the frequency converted signal powers increase linearly with the optical power and then attain a maximum value beyond which they drop slowly with any further increase in the optical power due to the MSM being near saturation. Thus,

for a fixed input RF power, the CNR can be maximized by varying the laser bias. A bias current of 50 mA was chosen to maximize the upconverted signal CNR.

## 4.3.1 Effect of RF Input and LO power variations

The up/down-converted signal power increases approximately linearly as a function of RF input power as shown in Fig. 4.12. The maximum RF input power that could be used to drive the laser source was limited by the OMI of the modulating signal. In order to understand the effect of LO signal variations on the OEM output components, the input LO power was continuously varied from -20 dBm to 0 dBm and the corresponding variations in the LO, up/down-converted signals were observed. This variation is shown in Fig. 4.13 and it can be seen that the signal level of the three components increases due to the improvement in conversion loss of the OEM with increasing LO power.

In order to suppress the high power LO feedthrough, its harmonics and other unwanted frequencies and to obtain the desired upconverted signal, a band pass filter with a center frequency at 1.8 GHz and a bandwidth of 50 MHz was used. The spectrum of the filtered and amplified signal at 1.8 GHz just before the BS transmitting antenna is shown in Fig. 4.14. The frequency upconverted signal thus selected was suitably amplified by a cascade of two microwave amplifiers. These amplifiers provided a combined gain of 40 dB with a negligible amount of distortion. The upconverted signal level rises to about -9 dBm and the CNR in this case is about 44 dB. The CNR in this case is also limited by the thermal noise floor and also because of the poor noise performance of the laser diode.
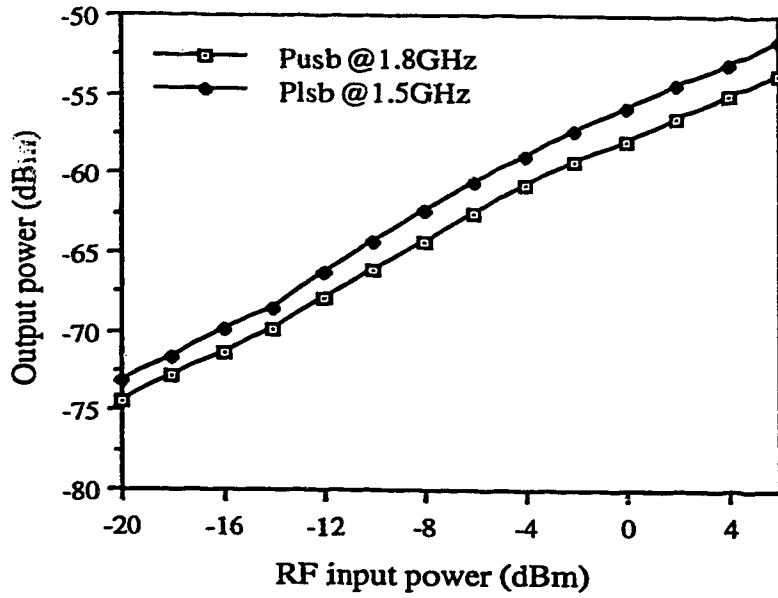
Fig. 4.12 Measured results of link output power vs RF input power
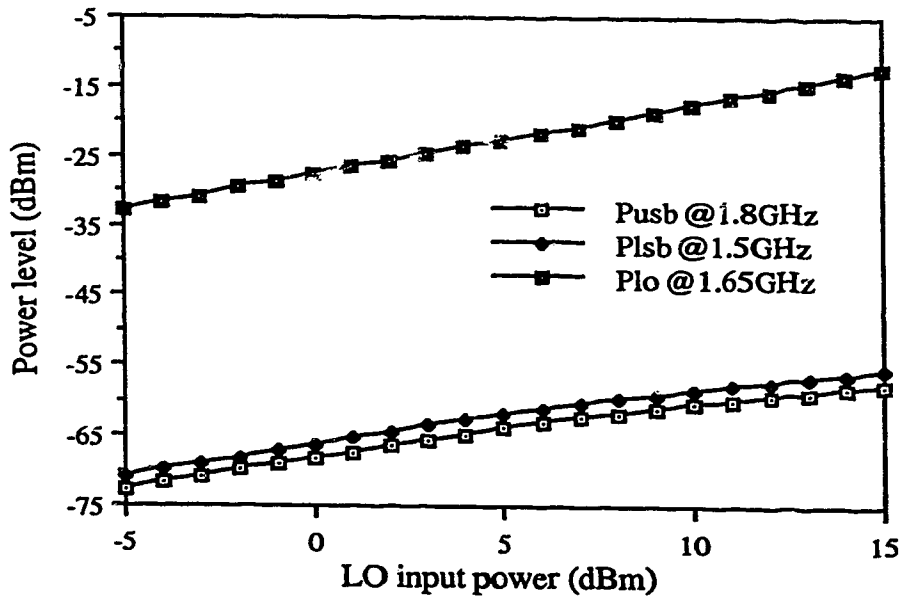


Fig. 4.13 Measured results of LO and sideband power levels vs LO input power

RL 10.00 dBm                          MKR #1 FRQ 1.799 84 GHz
*ATTEN 20 dB                                            -8.83 dBm
10.00 dB/DIV
                                                        POS PK
MARKER
1.799 84 GHz
-8.83 dBm
1

CENTER 1.805 00 GHz                   SPAN 35.00 MHz
*RB 300 kHz      *VB 10.0 kHz         ST 50.00 msec
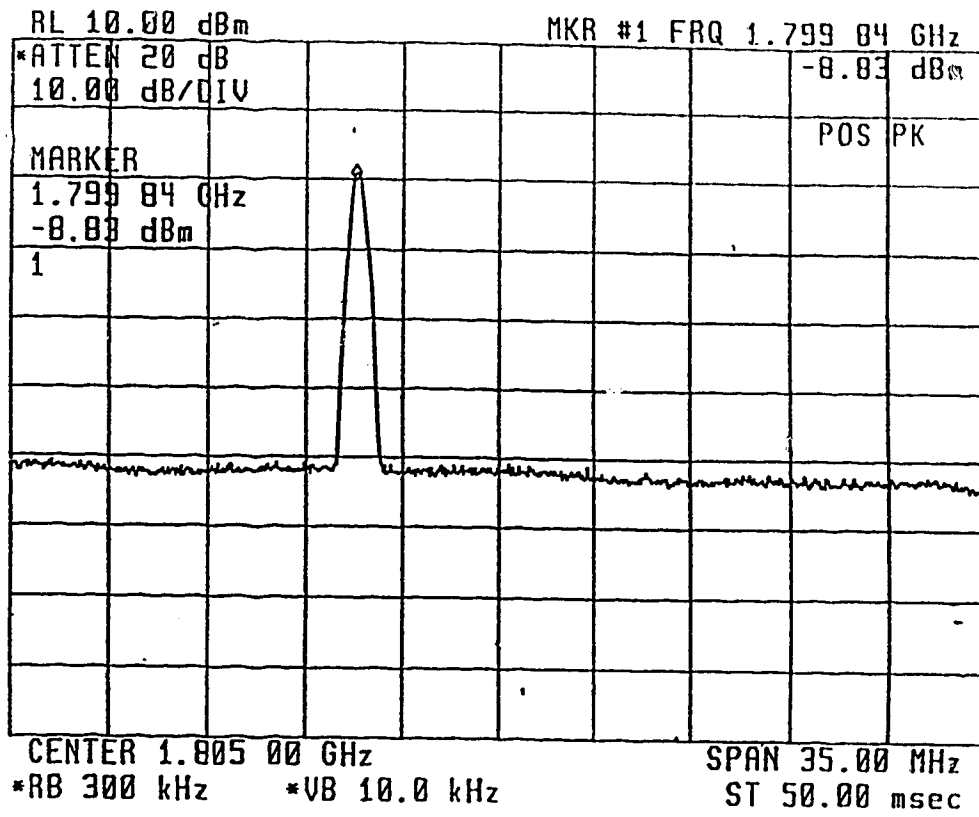
**Fig. 4.14 Spectrum of the upconverted signal at the link output**
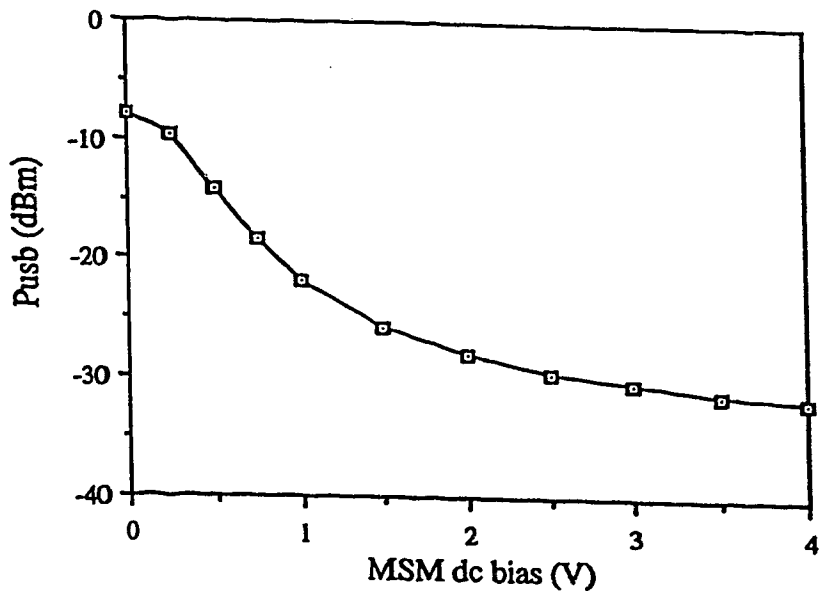
**Fig. 4.15 Measured upconverted signal power as a function of MSM dc bias**

## 4.3.2. Effect of MSM dc bias on output CNR

The upconverted signal was found to be maximum at zero dc bias due to the lower conversion loss of the mixer as shown in Fig. 4.15.

With a gradual increase in the bias, the upconverted signal level was found to decrease sharply in the low bias region because of the large dynamic responsivity of the MSM-PD and then attained a saturation beyond 1.5 V due to the dynamic responsivity being very low. The measured values of the upconverted signal power (Point C in Fig. 4.9) as a function of laser bias current for a MSM dc bias of 0 V and 0.5 V are shown in Fig. 4.16. It can be seen that the signal level increases with increase in the bias current but reduces with an increase in the dc bias. The upconverted signal variations with LO power were measured and are shown in Fig. 4.17 for a bias of 0 V and 0.5 V. It can be seen from Fig. 4.17 that for a 0 dBm input LO power, the signal power at 0.5 V bias is about 12 dB lower than that for a bias of 0 V. The lower values of signal power at 0.5 V bias is due to the lower conversion loss of the OEM with increasing MSM dc bias as explained earlier. It can also be seen that for a 0 V bias, the MSM is near saturation more quickly than that due to an increased bias of 0.5 V. The nonlinearities in the measured results could be attributed to the upconverted signal dependence on the square of the responsivity term $K_1$ as defined by Eqn. (3.23) in Section 3.5.1.

### 4.3.3 Harmonic performance of the link

In order to understand the harmonic behaviour of the OEM link, the bandpass filter had to be removed at the OEM output. The OEM was followed by the cascaded amplifier chain in
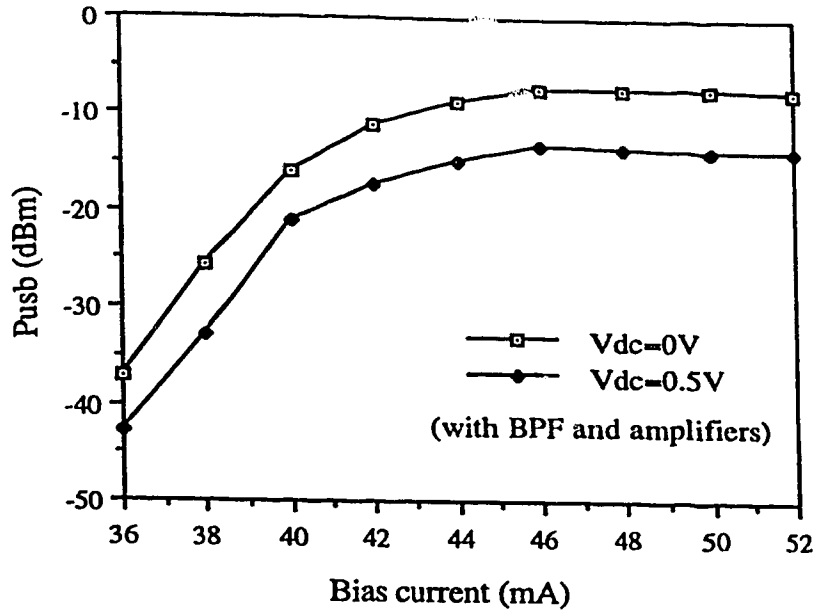
**Fig. 4.16 Measured values of the upconverted signal vs laser bias current**
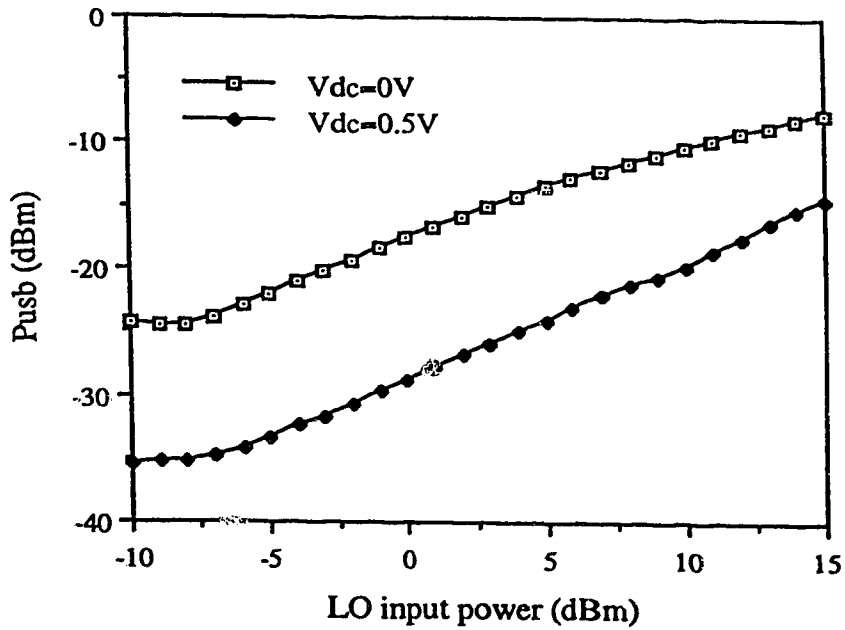


**Fig. 4.17 Measured upconverted signal power vs LO input variations**

order to enhance the harmonic signal powers to a level that could be detected by the Spectrum Analyser at the link output. Initially, the variations of the input and up/down-converted signal power were obtained at the link output as a function of RF input power as shown in Fig. 4.18.

It can be seen that the amplifiers provide uniform gain of about 40 dB without distortion to the variations in the amplitude of the incoming signals. The variation of LO harmonic power levels at the link output as a function of LO input variation is shown in Fig. 4.19. The detected fundamental, second and third harmonic levels of the link at an RF input power level of 0 dBm are 17 dBm, -2 dBm and -20 dBm, respectively. As the detected fundamental frequency level is less than -54 dBm, the suppression ratio of fundamental and second harmonic is greater than 52dB.

## 4.4 SCM (2-channel) transmission

In this section, experimental results obtained from two channel SCM radio transmission over a fiber optic link are discussed. The system configuration in this case is similar to the single channel case except for the addition of a second RF signal source and a power combiner as shown in Fig. 4.20.

Two closely spaced RF input signals of equal amplitude were generated using the two sources, at 150 MHz (HP 8642 A signal generator) and 160 MHz (HP 8753A Network Analyser), and electrically combined in a power combiner. The combined signal was used to intensity modulate the optical output of the LD. The modulated optical signals were
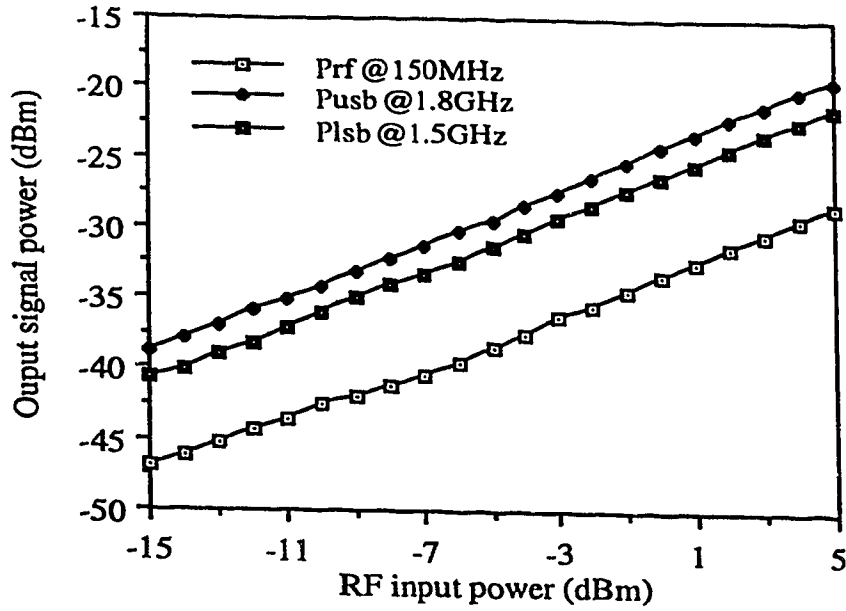
**Fig. 4.18 Measured values of the input and sideband powers vs RF input power**
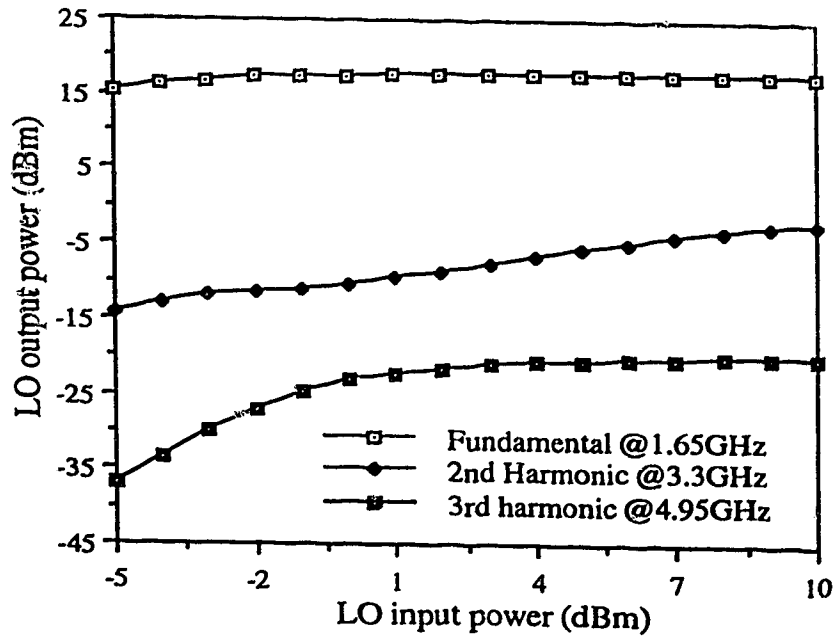


**Fig. 4.19 Measured values of the LO output and its harmonics vs LO input power**
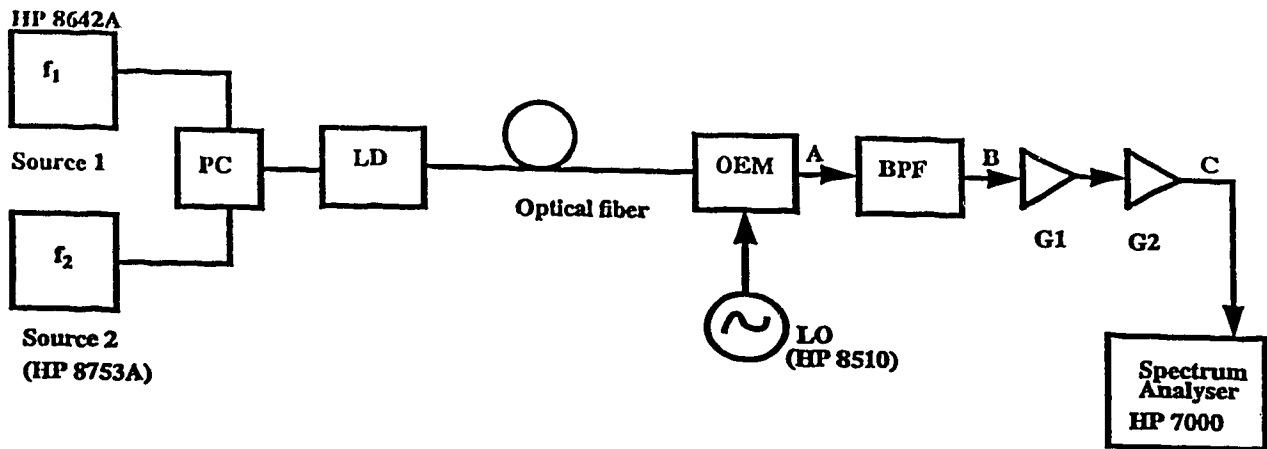
**Fig. 4.20 Schematic of the 2-channel SCM system over fiber optic link**
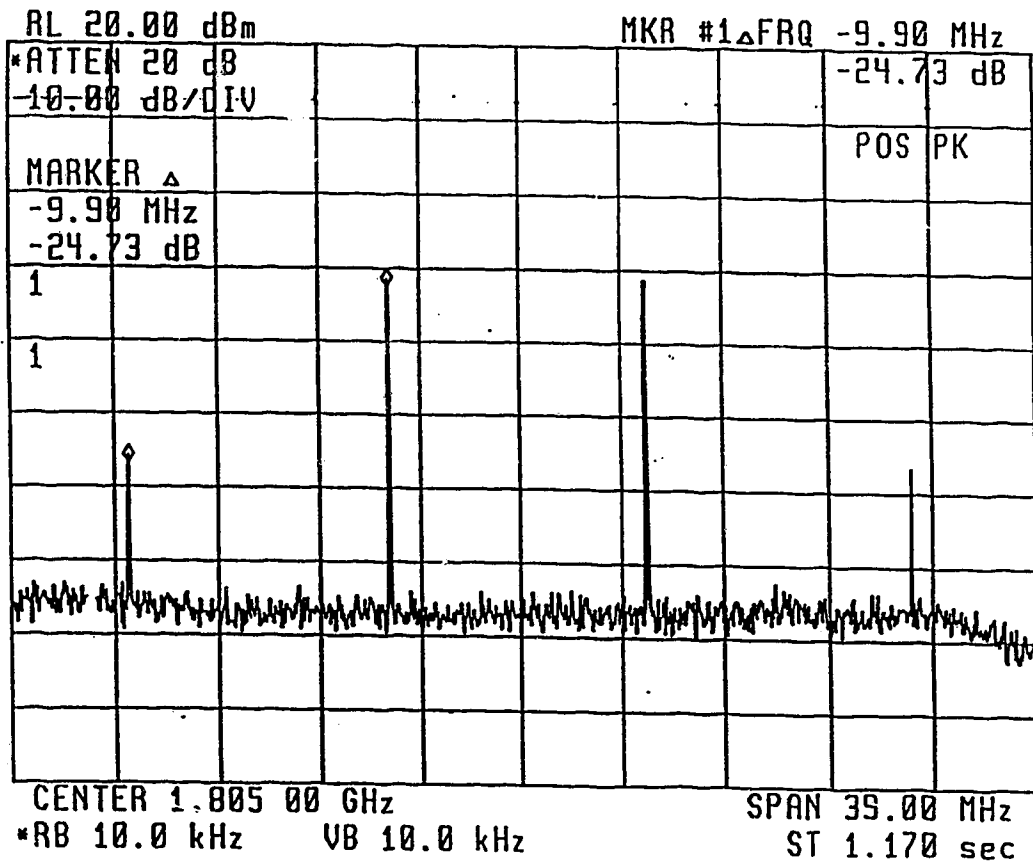


**Fig. 4.21 Spectrum of the upconverted and IM signals in a 2-channel SCM system**
**(laser bias current=44 mA)**

transmitted along a short length of multimode fiber to the optical receiver where they are converted by the OEM into their equivalent electrical signals. When the LD is driven by the SCM signal, third-order IMD noise results at the transmitter end due to the inherent nonlinearities within the LD. The IM components when propagated along the fiber to the optical receiver limit the overall transmission quality of the link and thus the system capacity. These properties will be appropriately discussed in evaluating the link performance.

The incoming optical signal and an electrical LO signal at 1.65 GHz from a HP 8510 Spectrum Analyser form the two inputs to the mixer. The OEM output consists of frequency upconverted signals at 1.8 GHz, 1.81 GHz, down-converted signals at 1.49 GHz, 1.5 GHz, third-order IM components at 1.48 GHz, 1.51 GHz, 1.79 GHz and 1.82 GHz, harmonics of the LO and other frequency components respectively.

A BPF with 50 MHz bandwidth is placed at the front end of the OEM in order to suppress the high power LO and its harmonics and the filtered output consists of the upconverted signals at 1.8 GHz and 1.81 GHz respectively. The third-order IM signals at 1.79 GHz, 1.82 GHz fall within the bandwidth of the BPF and hence appear at the output of the OEM. The upconverted signals are amplified by a cascade of two microwave amplifiers which provide a combined gain of about 40 dB. The upconverted signal is then coupled to a transmitting antenna at a level of about -24 dBm. The spectrum of the upconverted and IM signals measured by a Spectrum Analyser with a 40 MHz span bandwidth at the transmitting antenna input is shown in Fig. 4.21. The laser bias current was 44 mA and the MSM was dc biased to 0 V in order to obtain the maximum power in the upconverted sig-

nal. A 0 dBm LO signal was supplied to modulate the dc bias of the MSM detector.

The spectrum of the upconverted signal applied to the Tx antenna is shown in Fig. 4.21 and can be seen that the CNR in a 10 kHz noise bandwidth is 46 dB and the CIR is 25 dB. The CIR could be further improved to 40 dB by increasing the laser bias current to 49 mA with similar conditions of dc bias and LO power. The IM suppression was much better in this case but increasing the laser bias did not result in a significant change in the upconverted signal power. When the bias was still further increased to 51 mA, there was an improvement in the CIR by about 2 dB. The upconverted signal power increased by about 5 dB and thus the upconverted signal CNR was found to increase to 47 dB. The measured signal spectrum under the same conditions of dc bias and LO power for this case is shown in Fig. 4.22.

In order to estimate the optical link loss, the spectrum of the 0 dBm input modulation signals was measured at the OEM output, with direct detection after transmission over the optical link, as shown in Fig. 4.23. The total link loss when the MSM-PD was dc biased to 0 V, was 80 dB as measured in Fig. 4.23. When the bias was increased slowly upto 1 V, the link loss improved accordingly in a linear fashion and with further increase in the bias beyond 1 V, the loss remained constant. With a bias of about 4 V, the total loss was about 39 dB better than that at 0 V bias and the spectrum of the input signals in this case is shown in Fig. 4.24. This is because of the sharp rise in the input signal CNR in the low bias region and saturation beyond 1 V in agreement with the responsivity of the MSM detector as shown in Fig. 3.12. Thus with an increase in the MSM dc bias from 0 V to 4 V, the total link loss improved to 41 dB. This loss could be attributed significantly to the

RL 20.00 dBm                                          MKR #1∆FRQ 19.05 MHz
•ATTEN 30 dB                                                    42.32 dB
10.00 dB/DIV         ·

MARKER ∆                                                        POS PK
19.05 MHz
42.32 dB
1

1

ˆ                                         ◊

ˆ

CENTER 1.805 00 GHz                            SPAN 40.00 MHz
•RB 10.0 kHz         VB 10.0 kHz               ST 1.200 sec
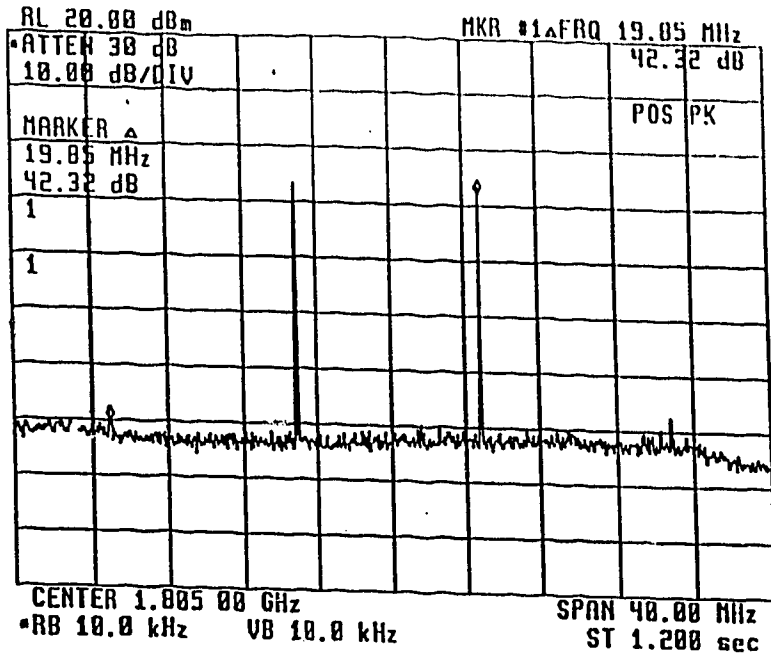
**Fig. 4.22 Spectrum of the upconverted and IM signals in a 2-channel SCM system (laser bias current=51 mA)**

RL -15.00 dBm                                        MKR #1 FRQ 160.10 MHz
•ATTEN 0 dB                                                    -79.77 dBm
10.00 dB/DIV IV

MARKER                                                          POS PK
160.10 MHz
-79.77 dBm
1

1

START    140.00 MHz                            STOP 170.00 MHz
•RB 10.0 kHz         VB 10.0 kHz               ST 900.0 msec
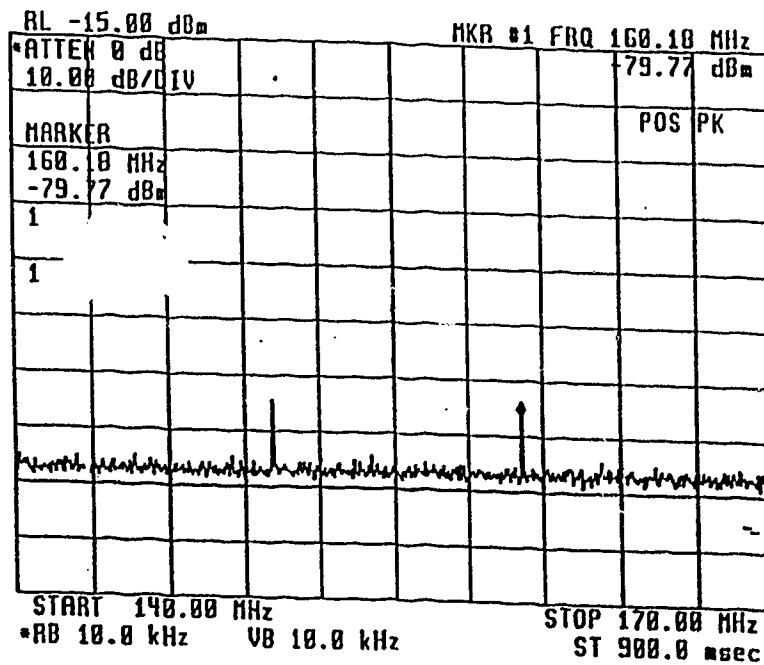
**Fig. 4.23 Spectrum of the input signals upon transmission over the optical link (MSM dc bias=0 V)**

77

```
•ATTEN 0 dB                                      -41.34 dBm
 10.00 dB/DIV        .
                                                 POS PK
 MARKER
 160.16 MHz
 -41.34 dBm
 1

 1
```

CENTER 155.00 MHz                      SPAN 25.00 MHz
•RB 10.0 kHz         VB 10.0 kHz        ST 750.0 msec
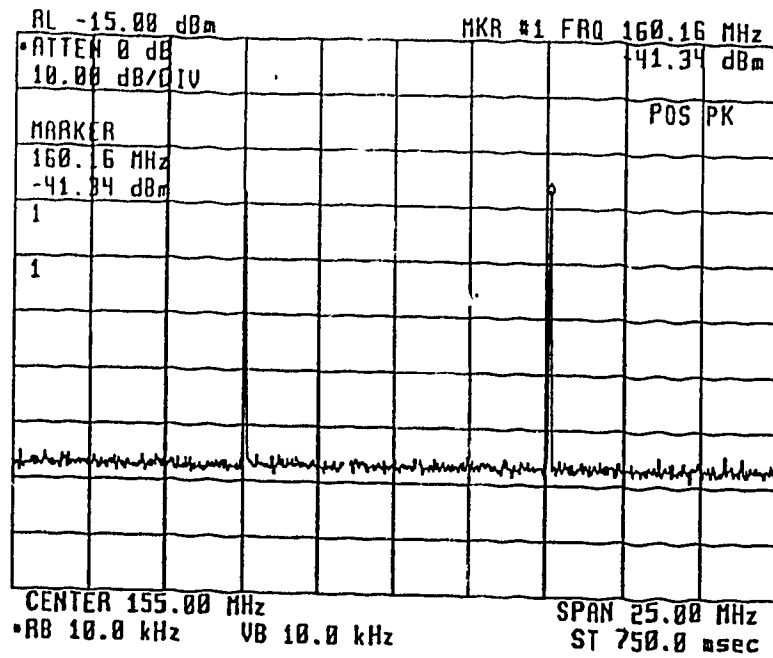
**Fig. 4.24 Spectrum of the input signals upon transmission over the optical link (MSM dc bias=4 V)**
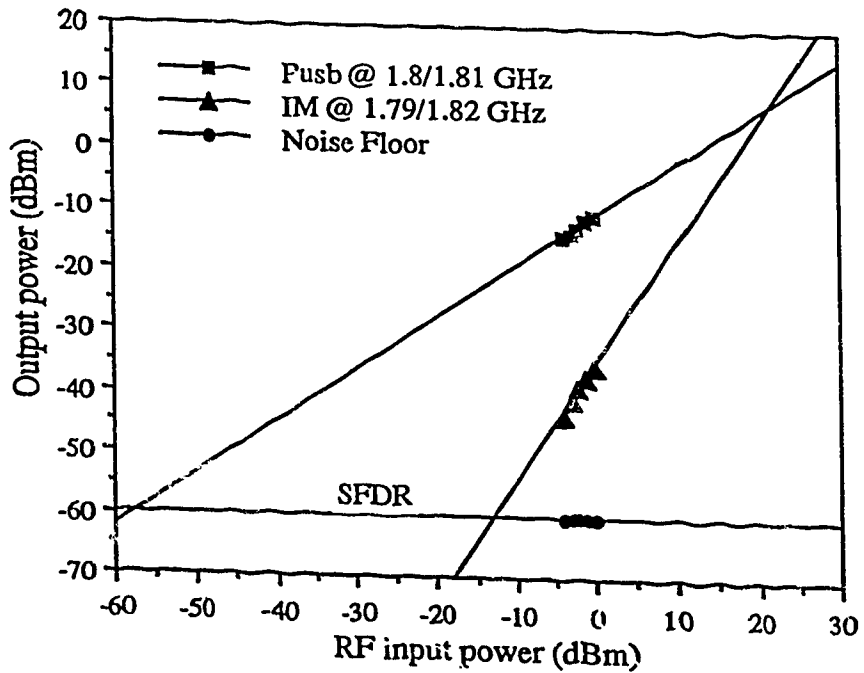


**Fig. 4.25 Measured results of the output and IM power level vs RF input power**

OEM's conversion loss dependence upon MSM bias in accordance with Eqn. (3.24) and also in part due to the optical link and other components. Further improvements in the link loss can be obtained with an increase in the laser bias current.

In the next section, analysis of the OEM is presented based on the measured results, taking into account the variations of RF/LO input power, laser bias and MSM dc bias.

## 4.4.1 Effect of RF input and LO power variation

The measured levels of the upconverted signal at 1.81 GHz and IM signal at 1.82 GHz at the amplifier output (Point C in Fig. 4. 20) are shown as a function of RF input power in Fig. 4.25. They are found to increase linearly with the input power. From Fig. 4.25, it is possible to find out the third-order intercept point which helps to determine the intermodulation or spurious free dynamic range. The measured third-order intercept point was 6 dBm and 1 dB compression point was -12 dBm. The spurious free dynamic range (SFDR), which is defined as the level of IMD suppression achieved when that level equals the link CNR, was found to be about 42 dB.

The dependence of the measured upconverted and IM signal at a laser bias current of 44 mA and dc bias of 0 V, on LO input power, are shown in Fig. 4.26. It can be seen that the IM level for a 0 dBm input LO signal when the MSM-PD is dc biased to 0 V is about 22 dB below the upconverted signal. The upconverted and IM signal levels vary approximately in a linear fashion with change in LO power. The increasing number of hops in the IM signal power could be due to experimental errors. Thus, the upconverted signal to noise ratio could be improved with a higher LO input power. The measured LO output and

sideband signal power variations as a function of LO input power are shown in Fig. 4.27.
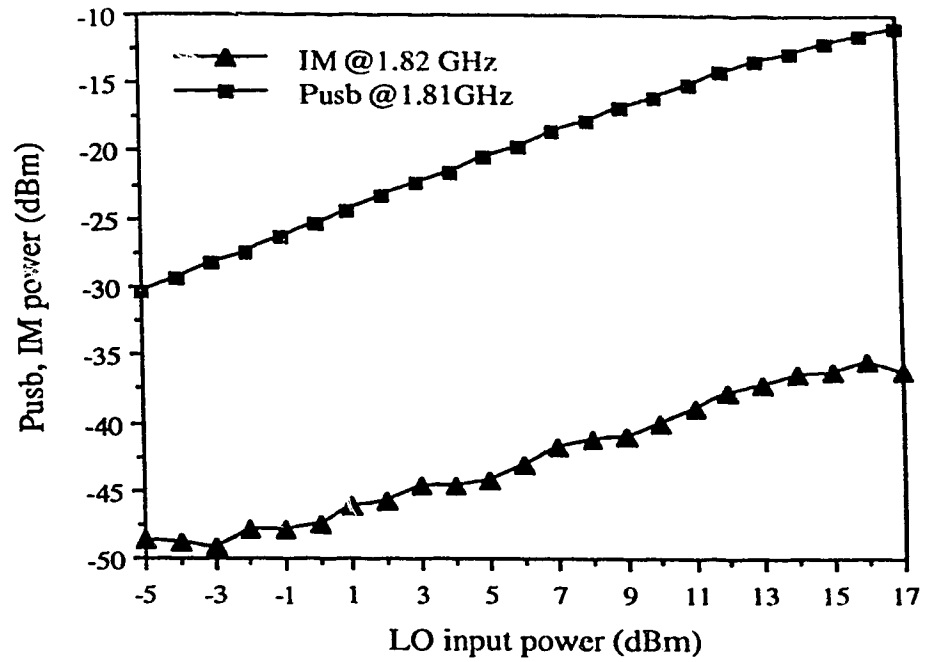


Fig. 4.26 Upconverted and IM signal powers at the link output vs LO input power
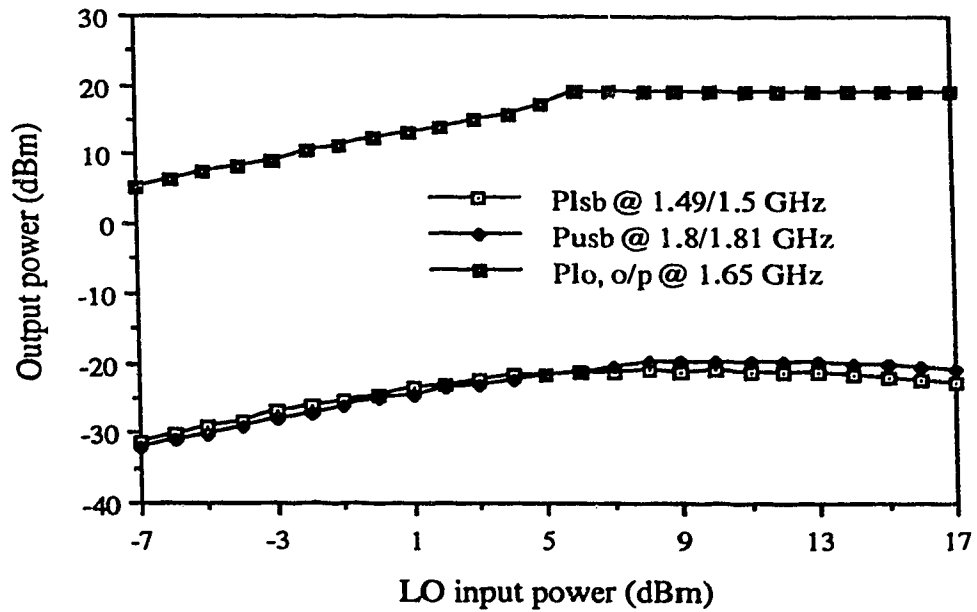


Fig. 4.27 Sideband and LO output power vs LO input variations

In this case the BPF was removed in order to obtain the lower sideband and LO signals and to understand the mixing process. The fundamental detected frequency at 1.65 GHz is 40 dB above the sideband signal level and rises slowly with LO input and then attains a maximum. This is because the high power LO could have driven the amplifiers into saturation and hence any further increase in the LO power does not result in a change in the output power. It can also be seen from Fig. 4.27 that the side band power increases linearly with increasing LO power upto 5 dBm beyond which there is a change in the power levels with the USB reaching saturation faster than the LSB. An input LO power which corresponds to a measured value of 0 dBm on the HP Spectrum Analyser was used for measurements in order to avoid the amplifiers being driven into their saturation region.

## 4.4.2 Effect of laser bias current

The variation of the measured upconverted and IM signal power as a function of laser bias current is shown in Fig. 4.28. From Fig. 4.28 it can be seen that the upconverted signal power increases slowly with increasing bias current and attains a maximum before it decreases again. This is because the system is limited by the IM noise for low bias currents (high OMI) and when the bias is large (low OMI), the thermal noise tends to dominate the system noise floor and hence the upconverted signal power increases with bias current. Also due to the inverse dependence between OMI and laser bias as in Eqn. (3.7), the IM signal power decreases with increasing laser bias current as shown in Fig. 4.28. The ratio of the measured upconverted to IM signal power as a function of laser bias is shown as a comparison with the theoretical results in Fig. 4.29 and they are found to be in close agreement except for some experimental uncertainties.
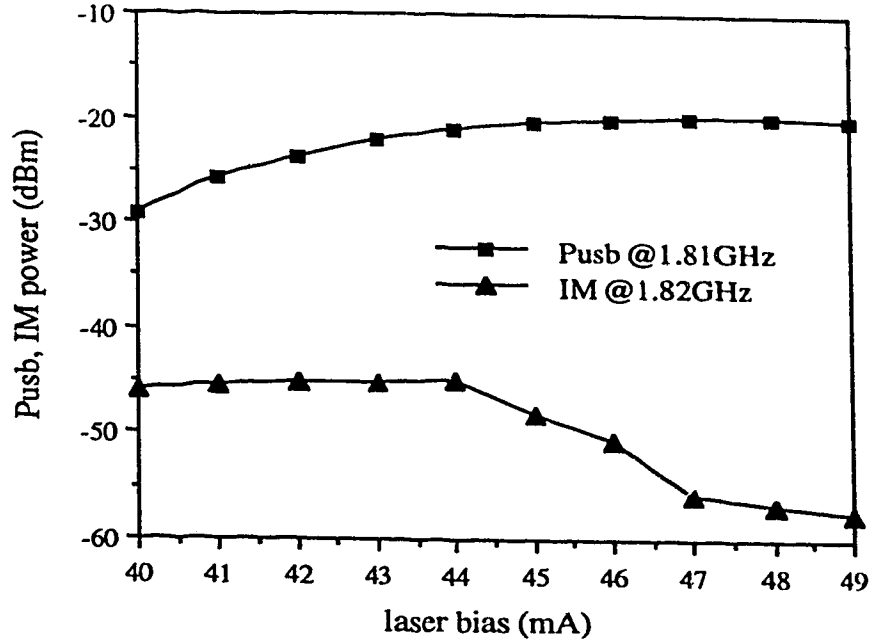
**Fig. 4.28 Measured upconverted and IM signal power vs laser bias current**

### 4.4.3 Effect of MSM dc bias

In order to estimate the input modulating signal powers at the link output, the BPF between the OEM and the amplifier chain in Fig. 4.20 is removed. The variations of input and upconverted signal powers (at point C in Fig. 4.20) were obtained as a function of MSM dc bias in order to calculate the mixer loss. The level of the intensity modulated direct detected optical subcarrier signals upon transmission over the fiber optic link were found to increase with bias in the low bias region and attained a saturation beyond 1 V due to the OEM loss dependence on input signal level.The measured conversion loss of the OEM as a function of dc bias is shown in Fig. 4.30 alongwith the numerical results obtained from Eqn. (3.25). A LO amplitude ($V_{lo}$)of 6 V was chosen in the model to obtain

the best possible agreement with the measured data.

In order to obtain the insertion loss of the BPF, the upconverted and IM signal powers were measured (at point C in Fig. 4.20) by placing the BPF in the link. It was found from the above results that the BPF inserted a link loss of about 3 dB. The measured variations of the upconverted signals (1.8/1.81 GHz), IM signals (1.79/1.82 GHz) and input signals (150/160 MHz) at the link output (Point C) are shown as a function of MSM dc bias along-with the numerical results in Fig. 4.31. The LO amplitude in this case was 6 V. It can be seen from Fig. 4.31 that the numerical results based on the MSM-PD analytical model are in close agreement with the measured data.

It can be seen that both the upconverted and IM signal powers decrease with increasing bias and attain a steady state when the MSM is near saturation. This is due to the OEM conversion loss being low at zero bias and increasing proportionately with increasing bias. This can also be explained in terms of the responsivity $K_1$ as defined in Eqn. (3.10), due to the direct dependence of both the signal variations on $K_1$. It was also found that the upconverted signal power at a dc bias of 0 V was 25 dB above IM3 signal but falls off to about 7 dB at a bias of 4 V. Thus with the OEM being operated under 0 V bias, its possible to obtain better IM suppression and hence the CIR.
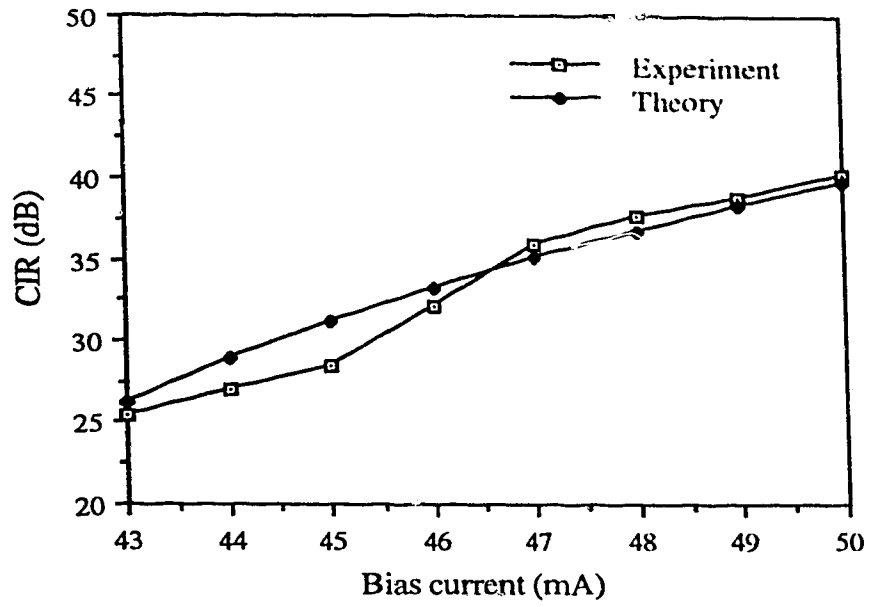
**Fig. 4.29 Measured upconverted to IM signal power ratio vs laser bias current**
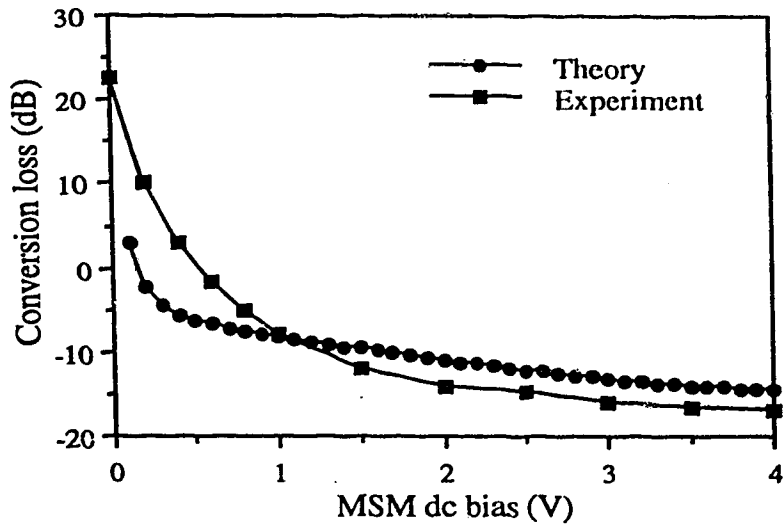


**Fig. 4.30 Comparison of OEM conversion loss vs MSM dc bias**
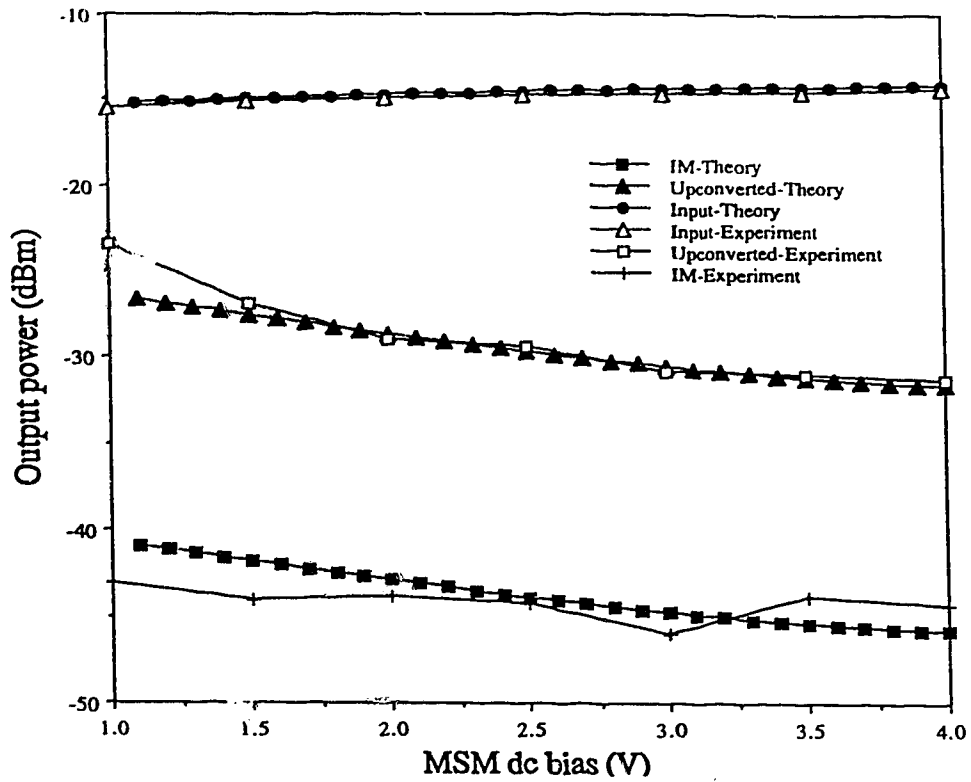
Fig. 4.31 Measured input, upconverted and IM signal powers vs MSM dc bias
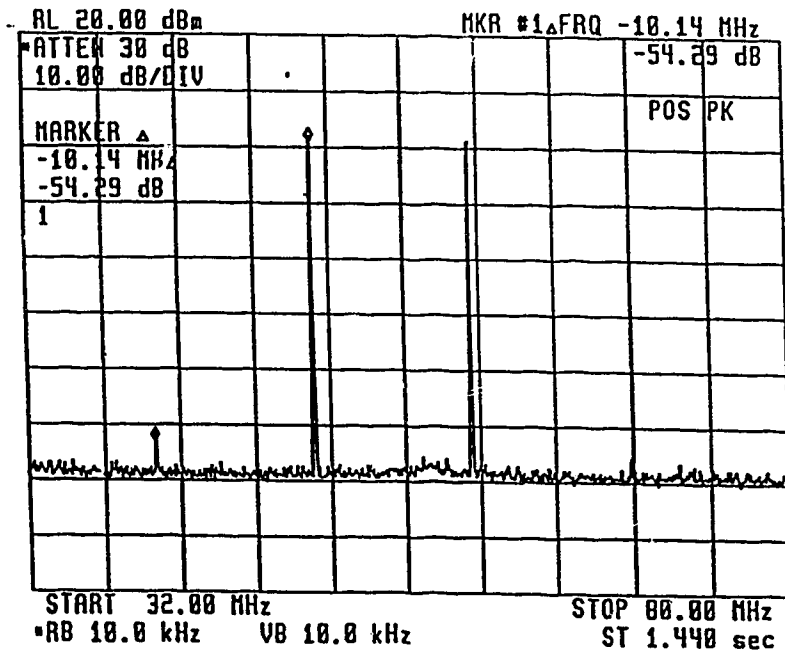


Fig. 4.32 Measured spectrum at the link output in a low frequency SCM system

85

## 4.5 Low frequency SCM transmission

The above experiment was repeated with subcarrier frequencies at 50 MHz and 60 MHz and with a LO at 1.75 GHz respectively. This was carried out to estimate the link CNR and IM noise performance of the LD. The measured spectrum of the signals at the link output (Point C in Fig. 4.20) for a laser bias of 52 mA, MSM dc bias of 0.22 V and 0 dBm LO power is shown in Fig. 4.32. The best CNR and CIR that could be obtained with a bias current of 56 mA were 62 dB and 54 dB respectively. This improvements in the CNR and CIR were obtained due to the better IM performance of the LD at low input modulation frequencies.

## 4.6 Digital transmission over the hybrid fiber-radio link

This section presents results on the performance of OEM in the transmission of low bit rate digital signals over the hybrid fiber-radio link, using $\frac{\pi}{4}$-DQPSK modulation scheme using the impulse response identification system (IRIS). These measurements were carried out at TR Labs, Calgary where the IRIS system was available [52].

The block diagram of the hybrid optical/RF transmitter is shown in Fig. 4.33. This transmitter configuration replaces the electronic RF modulator in the IRIS system by the optical link that consists of the LD, fiber, OEM and LO. As shown in the set up, the LD in the CS was modulated at a bias current of 50 mA, with a 0 dBm input $\frac{\pi}{4}$-DQPSK signal at 500 MHz. The DQPSK signal was generated by injecting a pseudorandom binary sequence (PRBS) from an arbitrary function generator (AFG) into the RF modulator (HP 8780A

Vector Signal Generator).

The intensity modulated optical signal was transmitted over a short length of fiber to the OEM where it was simultaneously detected and upconverted to the desired electrical frequency of 1.85 GHz using an input electrical LO signal at 1.35 GHz. The OEM was dc biased to 0 V and the LO had a power input of 0 dBm. The upconverted signal was selected by filtering the undesired frequencies using a BPF with its center frequency at 1.85 GHz and a bandwidth of 400 MHz. Then the upconverted signal was amplified by a cascade of two microwave amplifiers which provided a combined gain of about 50 dB. In order to suppress unwanted reflections that could affect the system performance, an isolator was placed between the amplifiers. Thus the upconverted signal could be used for radiation in the BS.

The IRIS radio receiver schematic is shown in Fig. 4.34. The signals from the MS or PS are captured by the BS receiving antenna. An identical BPF as in the transmitter was used at the receiver front end in order to reduce the interference that results from a variety of factors including radio fading, delay spread etc. The filtered signal was amplified by a cascade of two low noise amplifiers with a total gain of about 45 dB before being fed into the input of the microwave downconverter. An electrical LO signal at 1.65 GHz was used as the other input to convert the incoming high frequency signal into a 200 MHz IF signal. The IF signal was demodulated using a Vector Modulation Analyser and fed into a 500 MHz Oscilloscope. By proper sampling, the X-Y dual trace on the Oscilloscope was used to observe the demodulated DQPSK constellations.

The performance of the OEM was tested in back-to-back configuration and also by consid-

ering radio channel transmission in an indoor environment.

## 4.6.1 Back-to-Back (B-B) transmission

In this configuration the transmitter and the receiver are connected together at the antenna

ports with cables. The DQPSK constellations were tested with a 10 Mb/s base-band prob-

ing signal for a variety of 4, 8 and 10 bit maximal length PRBSs of fundamental length 511

bits. The demodulated constellation for a 4-bit sequence upon transmission over the B-B

link is shown in Fig. 4.35. The constellation is quite clear with almost no symbol errors.

The slight smearing in the constellation was due to the microwave downconverter being

overdriven by the LO signal at 1.65 GHz. Also, imperfections in the quadrature modulator

and demodulator components might have resulted in the rotation of the phase vector on an

elliptic trajectory. By adjusting the fiber positioner that couples light into the MSM-PD

through the OEM package, it was possible to control the instability in the constellation.

Also it can be seen that the B-B link does not exhibit any significant nonlinearities that

affect the constellation.

The spectrum of the DQPSK modulated signal at the laser input and upon transmission

over the fiber optic link is shown in Fig. 4.36 and Fig. 4.37. The CNR of the upconverted

signal at 1.85 GHz was about 24 dB which was very good for DQPSK signal transmission.

With a 5 dB reduction in the RF input signal power, the CNR reduced by about 4 dB. The

absence of link nonlinearities is quite evident from the measured spectrum.

## 4.6.2 RF Channel transmission

The system description is similar to that in the B-B case except that the radio channel is

taken into consideration. In this case, the upconverted signal is radiated in the BS by a transmitting antenna into the free space. The received signals are captured by a receiving antenna which is identical to the transmitting antenna. The signal suffers fading and other radio propagation losses. The received signal is filtered and suitably amplified before it is down-converted with a microwave converter. Further demodulation is carried out using an IF demodulator and the resultant complex signal is sampled to observe its constellation on the oscilloscope. The demodulated constellation for propagation through a 3 m radio channel is shown in Fig. 4.38. Again it can be seen that the constellation is free from symbol errors and the demodulated signal can be decoded to get back the original sequence. The spectrum of the DQPSK received signal after 3 m radio channel transmission is shown in Fig. 4.39 and it can be seen that the peak signal level is about -11 dBm. Though the received signal suffers a loss due to the EMI, multipath fading and delay spread etc., by using a passive filter and suitable amplification stages at the receiver front-end, it is possible to measure the received signal spectrum as shown in Fig. 4.39.

Also, the spectrum of the DQPSK modulated signal at the laser transmitter for a 8 bit PRBS with a 100 Mb/s base-band signal is shown in Fig. 4.40. The spectrum of the signal after transmission over the FO link at the input of the transmitting antenna is shown in Fig. 4.41 and the received spectrum after propagation through a 3 m radio channel is shown in Fig. 4.42. The distortions in the measured spectrum in Fig. 4.42 could be attributed due to the radio fading losses and also due to the instability of the antenna arrangement in the indoor environment. It can be seen from the above illustrations that the DQPSK signal preserves its characteristics upon transmission through the hybrid fiber-radio system.

For data rates equal to or above 100 Mb/s, the B-B configuration yielded good results in terms of the demodulated constellations. Figs. 4.43 and 4.44 show the input and demodulated constellation for a 8-bit sequence in this configuration. The radio channel performance was satisfactory in terms of the observed demodulated constellations. The symbol errors increased considerably and this could be mainly attributed to the losses in the radio link due to severe multipath fading.

Thus the hybrid fiber-radio system based on an OEM yields acceptable results for baseband digital transmission rates upto 100 Mb/s. The optoelectronic devices in the link do not introduce noticeable non-linearities in the transmission of signals as evidenced by their spectra discussed above.
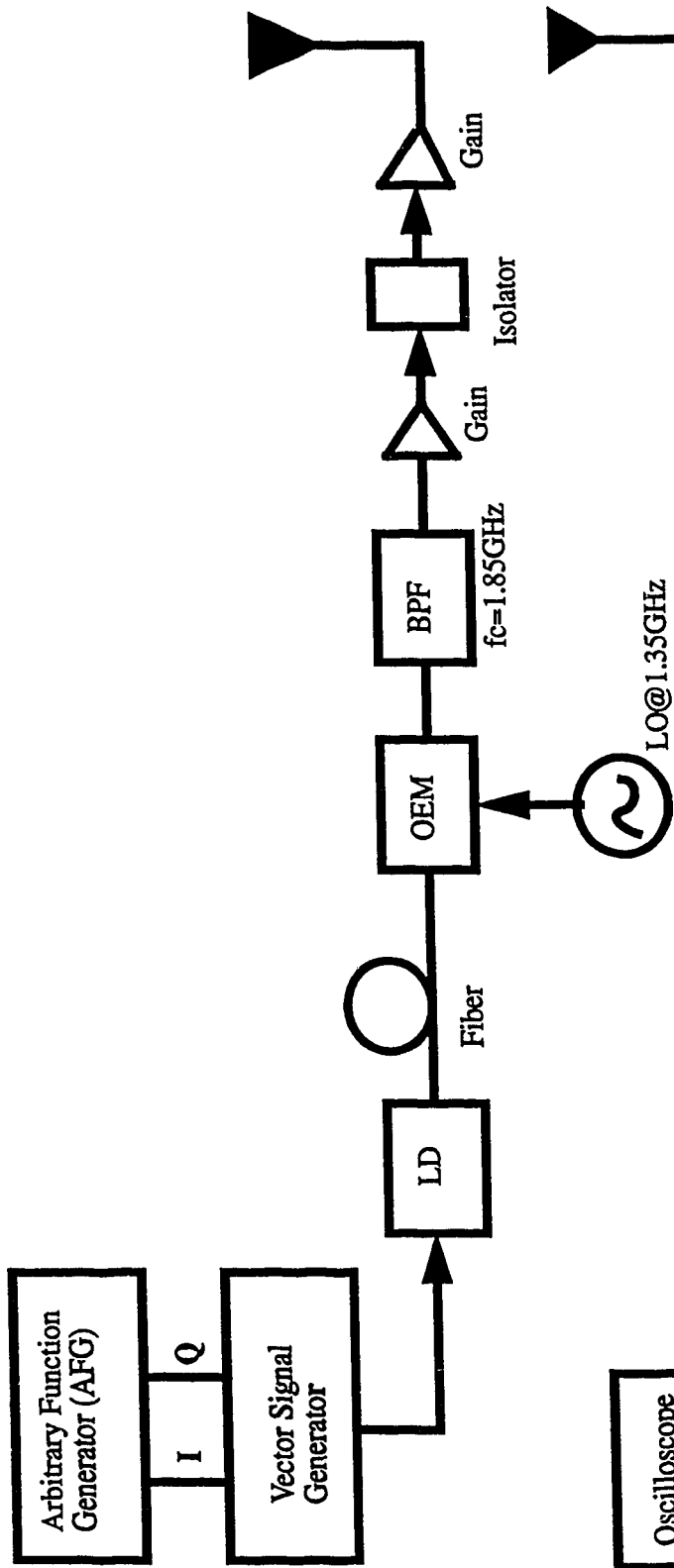
**Fig. 4.33 Hybrid optical/RF transmitter based on OEM**
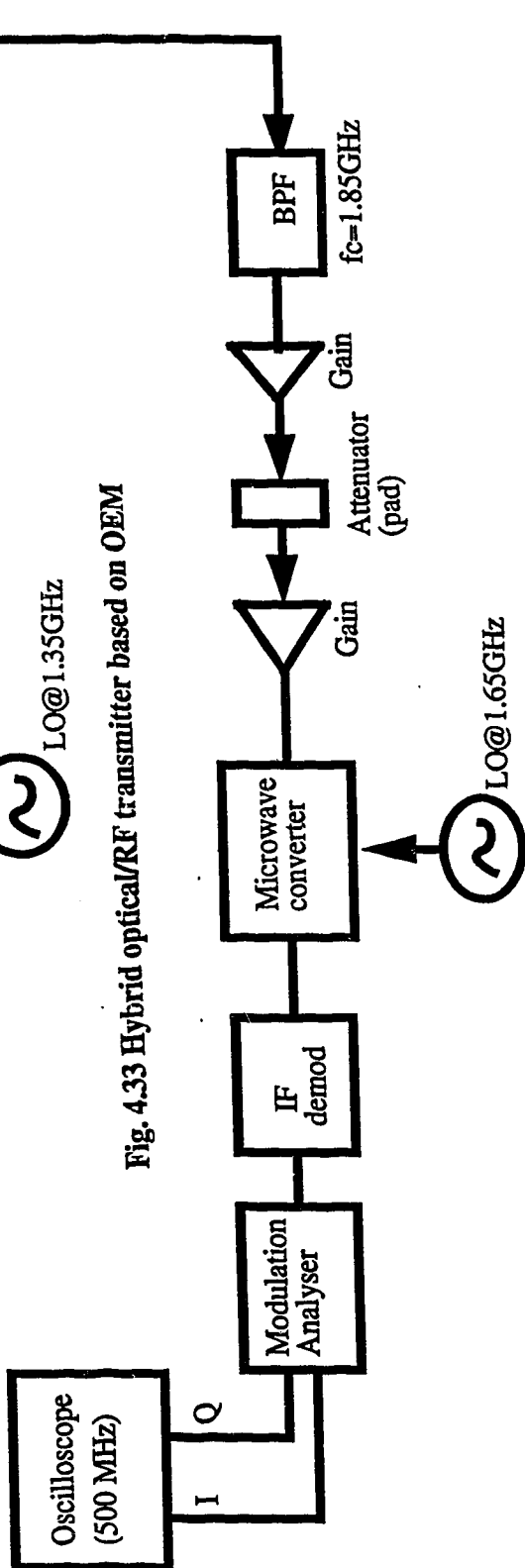


**Fig. 4.34 Block diagram of the IRIS receiver**
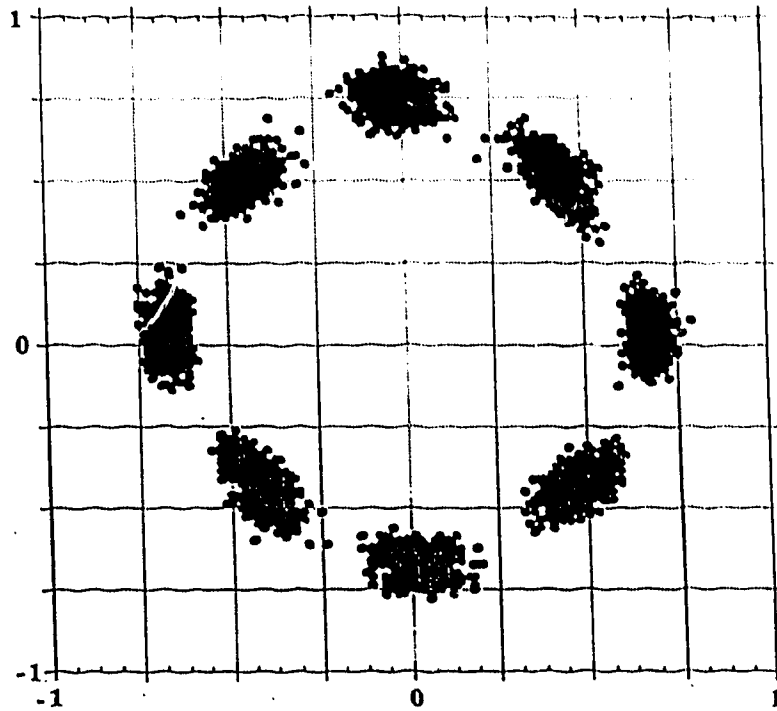
**Fig. 4. 35** Measured π/4-DQPSK demodulated signal constellation at 10Mb/s in a back-to-back configuration
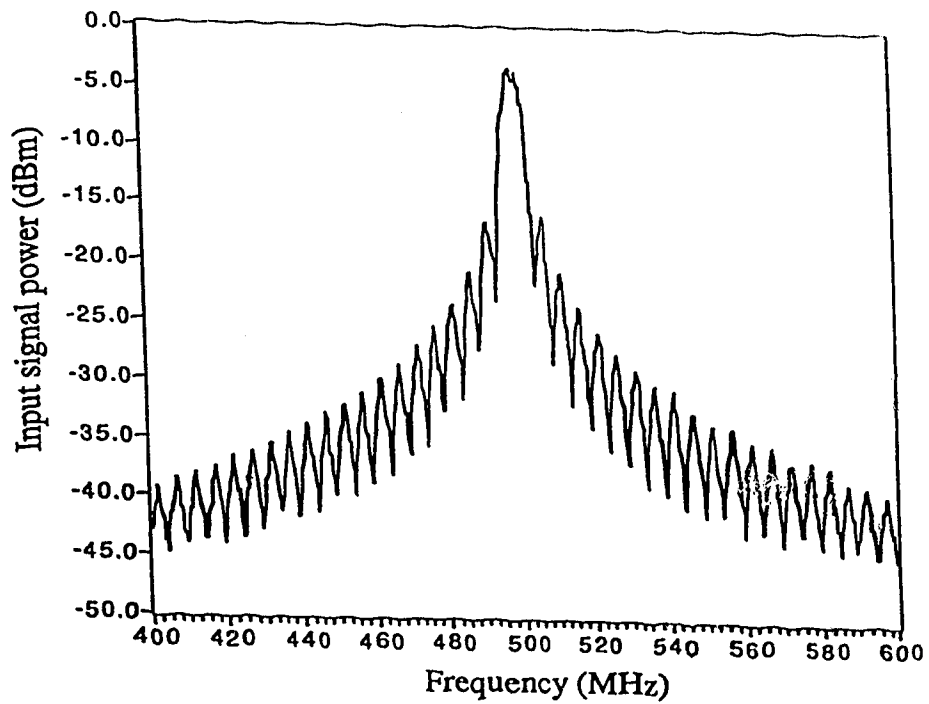


**Fig. 4.36** Measured spectrum of the DQPSK signal at the input of laser diode (4 bit sequence, data rate=10 Mb/s)
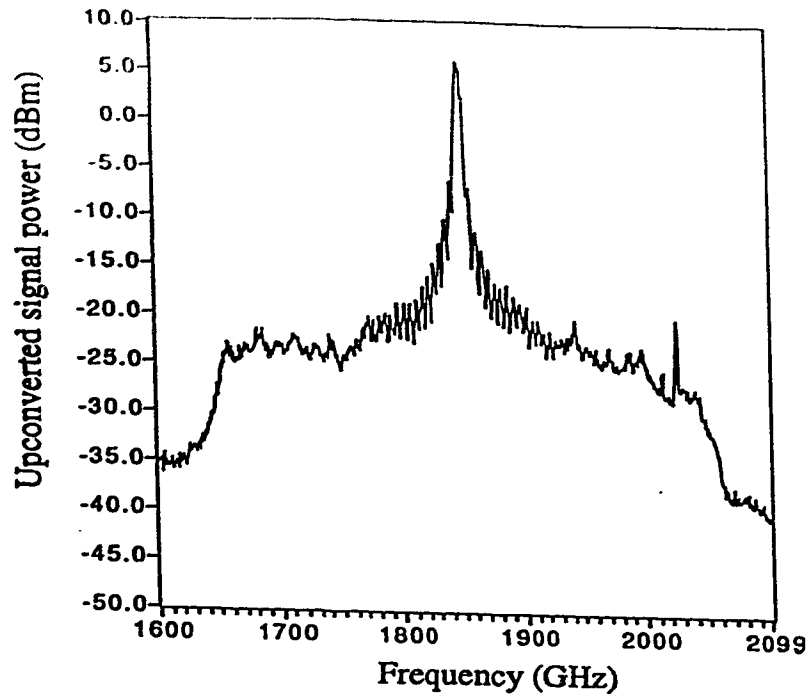
**Fig. 4.37 Measured spectrum of the upconverted signal at the input of Tx antenna**
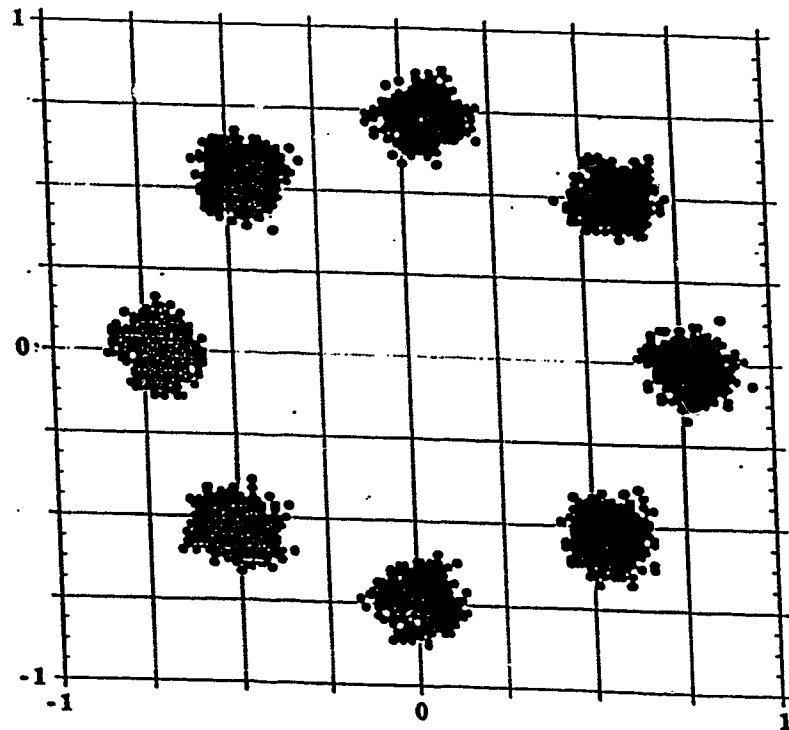


**Fig. 4.38 Measured π/4-DQPSK demodulated signal constellation at 10Mb/s in a 3 m RF propagation channel**
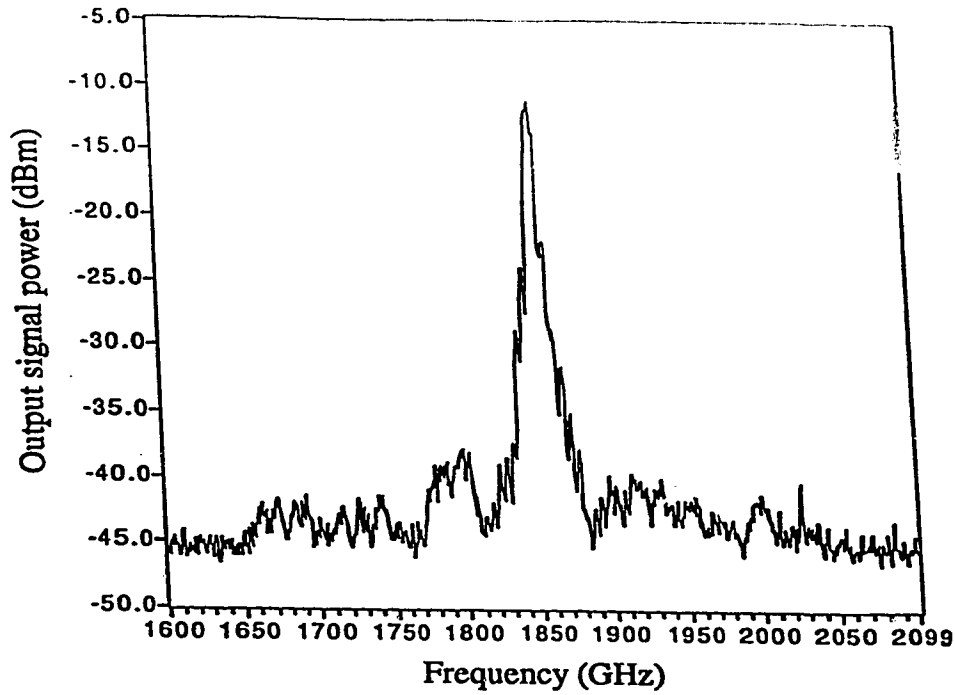
**Fig. 4.39 Measured spectrum of the upconverted signal at the output of Rx antenna**
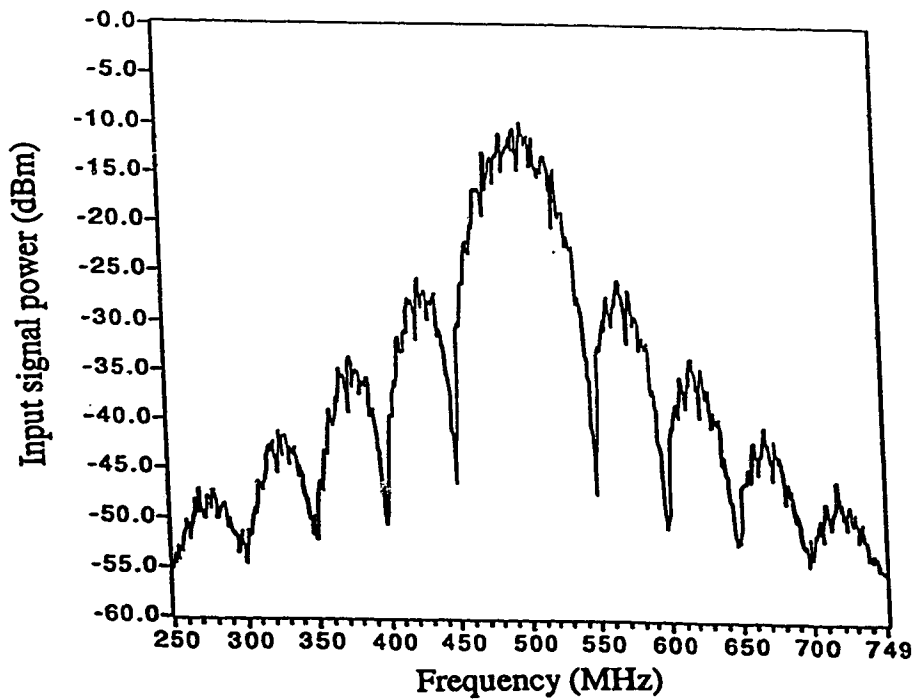


**Fig. 4.40 Measured spectrum of the DQPSK signal at the input of laser diode
(8 bit sequence, data rate=100 Mb/s)**
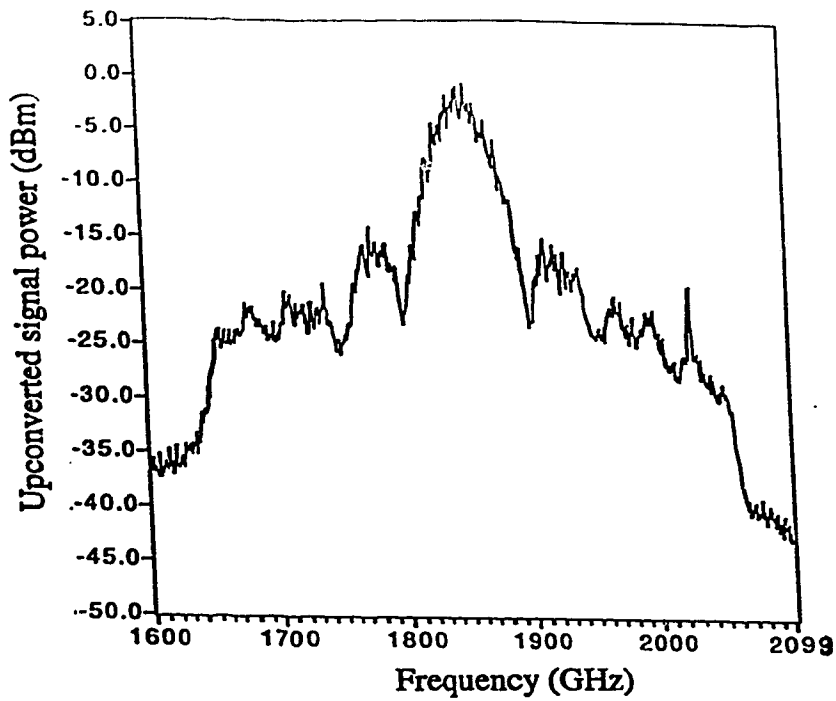
**Fig. 4.41 Measured spectrum of the upconverted signal at the input of Tx antenna**
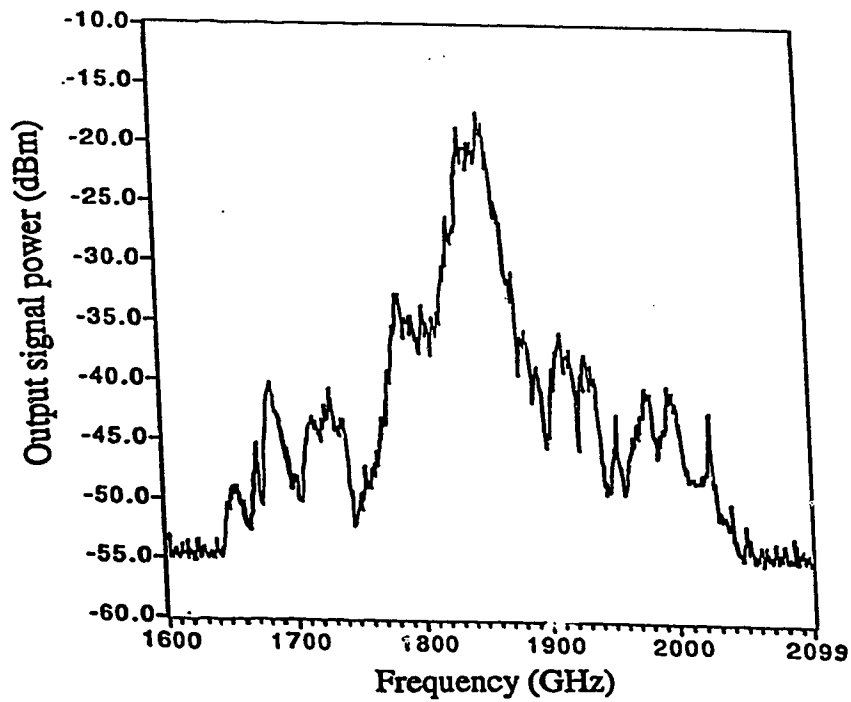


**Fig. 4.42 Measured spectrum of the upconverted signal at the output of Rx antenna
(3 m RF propagation channel)**
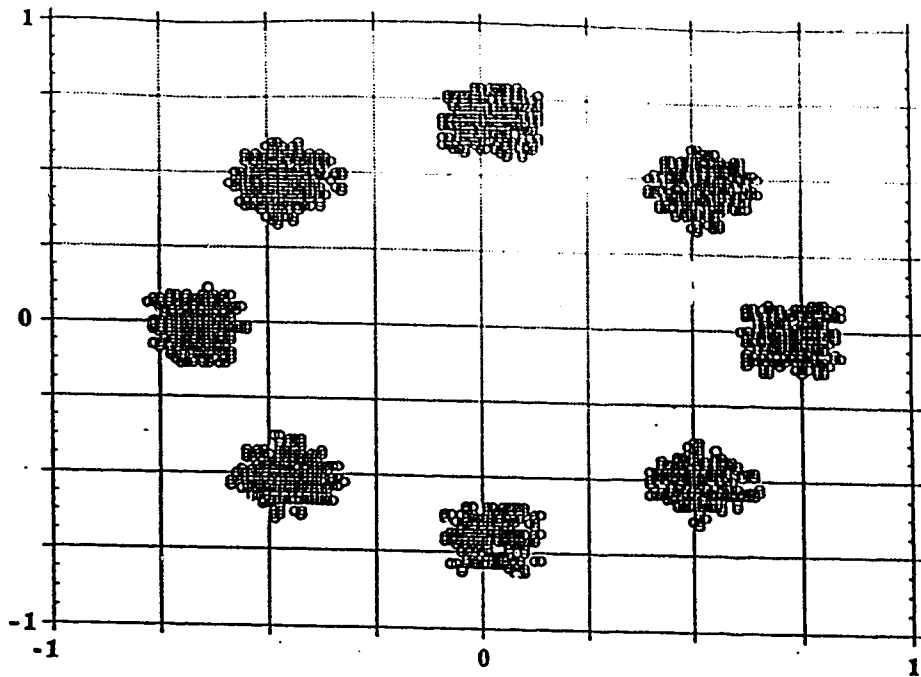
**Fig. 4.43** Measured π/4-DQPSK input signal constellation at 100 Mb/s
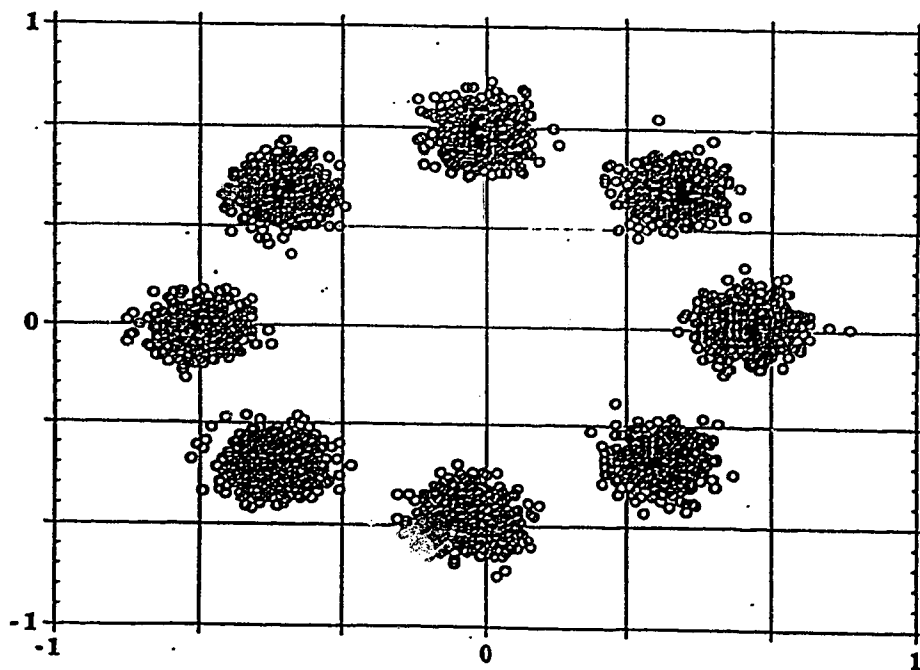


**Fig. 4.44** Measured demodulated signal constellation at 100 Mb/s

# 5. CONCLUSIONS

Microcellular radio communication systems using optical fiber feeders may offer the benefit of concentrating expensive RF components at a central station, and delivering RF signals to inexpensive multiple remote antennas. One of the key issues in implementing these systems is the networking of a large number of compact and cost-effective remote antennas to a local exchange. A large number of Micro-BSs that communicate with the PS/MS, can thus be connected with a fiber feeder to the CS thereby enhancing the capacity of the microcell system. This architecture has the advantages of higher reliability and easier maintenance due to its topological simplicity.

The difficulty of generating and transmitting high frequency optical signals is avoided in this work by mixing an information signal sent optically with a LO signal generated at the antenna. Using the detector as a mixing device considerably reduces the hardware required at the Micro-BSs as simultaneous photodetection and frequency conversion is made possible with the MSM-PD based OEM.

The high-speed properties of MSM-PD were studied by frequency response measurements which indicated a 3-dB bandwidth of about 3 GHz when the detector was properly biased. The detector was arranged in a suitably designed aluminium package for flexible test measurements. Thus the high-speed property of the photodetector could be used to perform mixing in the high frequency region. The dc responsivity of the MSM-PD was obtained experimentally with a 780 nm GaAs-AlGaAs semiconductor LD when the measured incident optical power was 430 μW. The detector had a responsivity of about 0.2 A/

W at a bias of 4 V. The mixing responsivity was obtained by modulating the dc bias with a locally generated high-frequency signal. The optoelectronic mixing process could be achieved because the responsivity of the MSM-PD was controlled by an applied voltage. Based on the experimental results, an analytical function was obtained for the dc-responsivity of the MSM-PD by a third-order polynomial fit. The model was found to be in close agreement with the experimental results.

Based on the mathematical model, the OEM properties were described in terms of its conversion loss (CL) and noise figure (NF). Analytical expressions were obtained for the CL in terms of the upconverted and input signals in the presence and absence of the LO modulation of the bias. The NF was defined in terms of the link input and upconverted CNR and a simplified analytical expression was obtained in terms of the CL.

The CL was strongly dependent on the MSM dc-bias and LO voltage amplitude. From the OEM analysis, the mixing process was found to be effective in the low bias region with a large LO voltage amplitude. A theoretical CL of about 22 dB was obtained with a dc bias of 0.5 V and an LO voltage of 1.5 V. The dependence of the input and upconverted signal powers on MSM dc bias was experimentally measured and the loss characteristic was found to be fairly close to that predicted by the theoretical model.

The overall link quality was described in terms of the CNR. The input and upconverted/ output signal CNR in a single channel and 2-channel SCM system were obtained by taking into account the various noise sources that influence the link performance. To examine the IM noise effects on the multichannel system CNR, a parameter called the CIR was defined in terms of the laser bias current and RF drive power. The CIR was found to increase with

increasing laser bias current due to the better suppression of IM noise. A 40 dB *CIR* was obtained at a bias of 50 mA as compared to 25 dB with a bias of 43 mA, when the LD was directly modulated with an electrically power combined signal with frequencies at 150 MHz and 160 MHz respectively. Further improvements in the *CIR* of about 55 dB, with identical bias, were obtained with low frequency modulation of the LD. The values obtained above were found to be in close agreement with the theory. Thus the frequency dependent IMD from the LD was found to be a dominant noise source in limiting the output signal *CNR*.

The output *CNR* was analysed with a variation in the system parameters and was found to be strongly dependent on the *OMI*, dc bias and LO voltage. The *CNR* variations were optimized with respect to *OMI*. For higher values of LO voltage, the output *CNR* in the low bias region was mainly influenced by the IM noise of the LD, whereas in the high bias region, receiver thermal noise was the dominant source. A theoretical *CNR* of about 48 dB could be obtained with an *OMI* of 0.27, dc bias of 0 V and an LO voltage of 0.15 V. This is identical to the experimental value obtained with a laser bias current of 50 mA, dc bias of 0 V and a LO power level of 0 dBm. The exact comparison between theory and experiment could not be made as the LO voltage parameter used in the model couldn't be directly related with the LO power used in the experiments. This could be attributed to the variable impedance of the MSM-PD as seen by the LO generator in its high frequency operation.

The SCM system was used to transport 2 closely spaced radio carriers (150 MHz and 160 MHz) over the optical link and the resultant signal was upconverted to 1.8 GHz using the

OEM. Higher values of *CNR* could be obtained with a better suppression of the IM noise effects. It was also seen that by modulating the LD with a low frequency subcarrier multiplexed signal (50 MHz and 60 MHz), a *CNR* of 62 dB and *CIR* of 54 dB could be obtained. A comparison of the theoretical and experimental results in the *CIR* evaluation were also found to yield good agreement. Thus the LD and MSM-PD mathematical models were fairly accurate in estimating the system performance criteria.

Numerical results based on the analytical expression for the OEM NF were obtained in terms of the MSM dc bias, LO voltage and *OMI*. In a single channel case, the NF was independent of *OMI* and was found to increase with dc bias due to the rise in the input signal *CNR*. The NF decreased with an increase in the LO voltage due to the rise in the output signal *CNR*. In a 2-channel SCM case, the NF was mainly influenced by the IM noise and could be maintained at a low value by controlling the *OMI* parameter. Thus effective operation of the OEM was obtained by a controlled variation of the various system parameters. Low CL and NF could be obtained at lower dc bias, high LO voltage at relatively higher power levels. The analysis and experimental investigations yielded fairly close results and thus the functional properties of the OEM could be utilized effectively in a variety of system designs.

The OEM's mixing properties were also tested in a hybrid fiber-radio link that was used for the transmission of low bit rate digital signals using $\pi/4$-DQPSK modulation. The performance of the OEM was tested for 10 Mb/s and 100 Mb/s digital signal transmission in back-to-back configuration and also by considering radio channel transmission in an indoor environment. The overall link quality was characterised in terms of the transmitted

constellation in both the cases and the hybrid link gave good results. Due to the instability of the antenna locations, some symbol errors were found in the demodulated constellations. It was also found that the linearity of the link was not affected by the introduction of the optoelectronic devices as confirmed by the measured spectra.

The following topics could be explored for future research in this field:

1. A more rigorous analysis could be carried out to estimate the optical link performance by taking into account the laser phase noise and interstage mismatch at the transmitter (LD) and receiver (PD) end. On the radio channel side, the Rayleigh Fading, Delay Spread losses could be considered in evaluating the overall link *CNR*. A more detailed power budget for this link could be proposed based on the exact system requirements for a practical case.

2. The laser transmitter nonlinearities could be compensated by designing a predistorting circuit at its input end. This would improve the IMD performance of the LD and thus improve the link *CNR* and *CIR*. Alternatively, a highly linearized source could be used at the expense of the system cost in the downlink. In the uplink from PS/MS to CS, the input level of the LD could be controlled with an AGC amplifier in order to extend the link dynamic range.

3. The MSM-PD based OEM could be integrated with the LO, band pass filter and amplifier chain in a MMIC package to realize a Micro-BS for portability and field trials.

4. The system performance could be tested with alternative modulation schemes including multilevel QAM, FM double modulation for improved voice quality transmission.

5. Diversity techniques could be explored to reduce the power level at the Micro-BSs due to fading, delay spread etc.

# BIBLIOGRAPHY

[1] T. Hattori, H. Sekiguchi, K. Kohiyama, and H. Yamamoto, "Personal communication-concept and architecture," in *Proc. ICC'90*, pp. 1351-1357, Jun. 1990.

[2] L. J. Greenstein *et al*, "Microcells in personal communication systems," *IEEE Communications Magazine*, vol. 30, pp. 76-88, Dec. 1992.

[3] T. E. Darcie, S. O'Brien, G. Raybon, and C. A. Burrus, "Subcarrier multiplexing for multiple access lightwave network," *J. Lightwave Technol.*, vol. 5, no. 8, pp. 1103-1110, 1987

[4] H. Ogawa, D. Polifko, and S. Banba, "Millimetre wave fiber optics system for personal radio communication," *IEEE Trans. Microwave Theory Tech.*, vol. 40, no. 12, pp. 2285-2293, 1992

[5] M. Shibutani *et al*, "Optical fiber feeder for microcellular mobile communication system," *IEEE J. Selected Areas in Communications*, pp. 1118, Sept. 1993.

[6] D. Tang, "Fiber-optic antenna remoting for multisector cellular cell sites," Conf. Record, *ICC*, paper 304. 1, Jun. 1992.

[7] R. Ohomoto *et al*, "Microcellular systems based on subcarrier transmission with a spectrum delivery switch," *IEEE J. Selected Areas in Communications*, Sept. 1993.

[8] D. K. W. Lam and R. I. MacDonald, "GaAs optoelectronic mixer operation at 4.5 GHz," *IEEE Trans. Electron Devices*, vol. 31, no. 12, pp. 1766-1768, 1984

[9] S. Malone, A. Paolella, P. R. Herczfeld, and T. Berceli, "MMIC compatible lightwave and microwave mixing techniques," in *IEEE Microwave Theory Tech.-S Int. Microwave Symp.*, pp. 757-760, 1992

[10] E. Suematsu and N. Imai, "Signal to noise performance of a fiber optic subcarrier link using an HBT optoelectronic upconverter," in *IEEE Microwave Theory Tech.-S Int. Microwave Symp.*, pp. 1501-1504, 1994

[11] Q. Z. Liu and R. I. MacDonald, "Controlled nonlinearity monolithic integrated optoelectronic mixing receiver," *IEEE Photon. Technol. Lett.*, vol. 5, no. 12, pp. 1403-1406, 1993

[12] Q. Z. Liu, R. I. MacDonald and R. Davies, " A simple and cost-effective fiber optic microwave link with monolithic integrated optoelectronic mixing receiver," in *Proc. of 6th Int. Conf. on Wireless Commun.*, pp. 250-256, 1994

[13] R. S. Tucker and I. P. Kaminow, "High frequency characteristics of directly modu-

lated InGaAs ridge waveguides and buried heterostructure lasers," *J. Lightwave Technol.*, vol. 2, pp. 385-393, 1984.

[14] T. Sueta and M. Izutsu, "Integrated optic devices for microwave applications," *IEEE Trans. Microwave Theory & Tech.*, vol. 38, pp. 477-481, 1990.

[15] I. Koffman, P. R. Herczfeld, and A. S. Daryoush, "High speed fiber optic links for short-haul microwave applications," *IEEE MTT-S Int. Microwave Symp. Dig.*, pp. 983-986, 1988

[16] A. S. Daryoush *et al.*, "Comparison of indirect optical injection-locking techniques of multiple X-band oscillator," *IEEE Trans. Microwave Theory & Tech.*, vol. 34, pp. 1363-1369, 1986.

[17] A. S. Daryoush, "Optical synchronization of millimeter-wave oscillator for distributed architectures," *IEEE Trans. Microwave Theory & Techn.*, vol. 38, pp. 467-476, 1990.

[18] H. Ogawa and Y. Kamiya, "Fiber optic microwave transmission using harmonic laser mixing, optoelectronic mixing and optically pumped mising," *IEEE Trans. Microwave Theory Tech.*, vol. 39, no. 12, pp. 2045-2051, 1991

[19] D. Polifko and H. Ogawa, "Fiber opticlink for microwave/millimeter wave transmission," *MWE'91 Microwave Workshop Dig.*, pp. 127-130, 1991

[20] D. Polifko and H. Ogawa, "Fiber optic link architectural comparison for millemeter wave transmision," *Proc. SPIE.*, vol. 1701, Optical Technology for Microwave Applications VI, pp. 228-239, 1992.

[21] H. Ogawa and H. Kamitsuna, "Fiber optic microwave links using balanced laser harmonic generation, and balanced/image cancellation laser mixing," *IEEE Trans. Microwave Theory Tech.*, vol. 40, pp. 2278-2284, 1992.

[22] H. Ogawa *et al.*, "Fiber optic microwave subcarrier transmission links using laser diodes as receiver mixer," *IEICE Trans. Electronics,* vol. E76-C, pp. 251-256, 1993.

[23] H. Kamitsuna and H. Ogawa, "Fiber optic microwave links using balanced/image cancellation photodiode mixing," *IEICE Trans. Electronics,* vol. E76-C, pp. 2264-270, 1993.

[24] D. Polifko and H. Ogawa, "Comparison of traveling wave external modulator microwave mixers," *IEICE Trans. Electronics,* vol. E76-C, pp. 257-263, 1993.

[25] T. Horimatsu and M. Sasaki, "OEIC technology and its application to subscriber loops," *J. Lightwave Technol.*, vol. 7, pp. 1612-1621, 1989.

[26] M. Dagenais *et al.*, "Application and challenges of OEIC technology: A report on the

1989 Hilton Head Workshop," *J. Lightwave Technol.*, vol. 8, pp. 846-861, 1990.

[27] K. B. Bhasin and D. J. Connolly, "Advances in gallium arsenide monolithic micro-wave integrated-circuit technology for space communication systems," *IEEE Trans. Microwave Theory Tech.*, vol. 34, pp. 994-1001, 1986.

[28] K. A. Dallabetta *et al.*, "MMIC compatible photodetector design & characterization," *Proc. SPIE, vol. 1371, High frequency analog fiber optic systems*, pp. 116-127, 1990.

[29] K. B. Bhasin *et al.*, "Detection of radio-frequency modulated optical signals by two and three terminal microwave devices," *Proc. SPIE, vol. 789, Optical technology for microwave application III*, pp. 60-66, 1987

[30] D. G. Parker *et al.*, "110 GHz high-efficiency photodiodes fabricated from Indium Tin Oxide/GaAs," *Electron. Lett.*, vol. 23, pp. 527-528, 1987.

[31] J. E. Bowers and C. A. Burrus, "Ultrawide-band long-wavelength p-i-n photodetec-tor," *J. Lightwave Technol.*, vol. 5, pp. 1339-1350, 1987.

[32] A. J. Seeds and B. Lenoir, "Avalanche diode harmonic optoelectronic mixer," *IEE Proc.*, vol. 133, Pt. J, no. 6, pp. 353-357, 1986

[33] S. J. Wojtczuk and J. M. Ballantyne, "Impedance properties and broad-band operation of GaAs photoconductive detectors," *J. Lightwave Technol.*, vol. 5, pp. 320-324, 1987.

[34] J. B. D. Soole and H. Schumacher, "InGaAs metal-semiconductor-metal photodetec-tors for long wavelength optical communications," *IEEE J. Quantum Electron.*, vol. 27, pp. 737-752, 1991.

[35] P. C. Claspy and K. B. Bhasin, "Optical detectors for GaAs MMIC integration: Tech-nology assessment," *Proc. SPIE, vol. 1102, Optical technology for microwave application IV*, pp. 53-60, 1989.

[36] S. J. Wojtczuk *et al.*, "Comparison study of easily integrable photodetectors," *J. Lightwave Technol.*, vol. 5, pp. 1365-1370, 1987.

[37] B. J. Van Zeghbroeck *et al.*, "105-GHz bandwidth metal-semiconductor-metal photo-diode," *IEEE Electron. Dev. Lett.*, vol. 9, pp. 527-529, 1988.

[38] S. Y. Wang and D. M. Bloom, "100 GHz bandwidth planar GaAs Schottky photodi-ode," *Electron. Lett.*, vol. 19, pp. 554-555, 1983.

[39] J. P. Noad *et al.*, "FET photodetectors: A combined study using optical and electron-bam stimulation," *IEEE Trans. on Electron. Devices*, vol. 29, pp. 1792-1797, 1982.

[40] A. A. de salles and M. A. Romero, "AlGaAs/GaAs HEMT's under optical illumina-

tion," *IEEE Trans. Microwave Theory Tech.*, vol. 39, pp. 2010-2017, 1991.

[41] J. K. Twynam *et al.*, "High-performance carbon-doped base GaAs/AlGaAs hetero-junction bipolar transistor grown by MOCVD," *Electron. Lett.*, vol. 27, pp. 141-142, 1991.

[42] Q. Z. Liu, R. Davies, and R. I. MacDonald, "Experimental investigation of fiber optic microwave link with monolithic integrated optoelectronic mixing receiver," *IEEE Trans. Microwave Theory Tech.*, vol. 43, no. 9, pp. 2357-2360, 1995.

[43] V. Hurm *et al*, "8.2 GHz bandwidth monolithic integrated optoelectronic receiver using MSM-photodiode & 0.5mm recessed gate AlGaAs/GaAs HEMTs," *Electronics Lett.*, vol. 27, no. 9, pp. 734-735, 1991.

[44] J. S. Wang, C. G. Shih, W. H. Chang, J. R. Middleton, P. J. Apostolakis,and M. Feng,"11 GHz bandiwdth optical integrated receiver using GaAs MESFET and MSM technology," *IEEE Photon. Techno. Lett.*, vol. 5, no. 3, pp. 316-318, 1993.

[45] J. Lipson, L. C. Upadhyayula, S. Huang, C. B. Roxlo, E. J. Flynn, P. M. Nitzsche, C. J. McGrath, G. L. Fenderson, and M. S. Schaefer, "High-fidelity lightwave transmission of multiple AM-VSB NTSC signals," *IEEE Trans. Microwave Theory Tech.*, vol. 38, no. 5, pp. 483-492, 1990.

[46] H. Mizuguti, T. Okuno, S. Komaki, and N. Morinaga, "Performance analysis of a fiber optic link for microcellular mobile communication systems," *IEICE Trans. Electron.*, vol. E76-C, no. 2, pp. 271-278, 1993

[47] M. De La Chapelle and H.P. Hsu, "Characetrization of fiber-optic links for microwave signal transmission," *SPIE Proc. on Optical technology for microwave applications III*, vol. 789, pp. 32-39, 1987

[48] J. H. Jacobi, "IMD still unclear after 20 years," *Microwaves & RF*, vol. 25, no. 11, pp. 119-126, 1986

[49] R. I. MacDonald and B. E. Swekla, "Frequency domain optical reflectometer using a GaAs optoelectronic mixer," *Appl. Opt.*, vol. 29, no. 31, pp. 4578-4582, 1990

[50] Q. Z. Liu and R. I. MacDonald, "Sensitivity analysis of integrated InGaAs MSM-PD's and HEMT optoelectronic receiver array," *IEEE Trans. on Electron. Devices*, vol. 42, no. 7, pp. 1221-1226, 1995

[51] Ray Decorby, M.Sc thesis, TR Labs, University of Saskatchewan, 1994

[52] B. Davies, "Using IRIS system, TR Labs Calgary", September 1995

## Table 1: Nonlinear Constants

| Nonlinear Laser Constants | Value | Units |
|---|---|---|
| $a_1$ | 1 | $A^{-1}$ |
| $a_2$ | 0.1 | $A^{-2}$ |
| $a_3$ | 0.01 | $A^{-3}$ |
| Nonlinear Responsivity Constants | | |
| $A_0$ | 0.15998 | $A/W$ |
| $A_1$ | 0.022412 | $A/WV$ |
| $A_2$ | -0.003998 | $A/WV^2$ |
| $A_3$ | 0.0002998 | $A/WV^3$ |
| $\alpha$ | 4.2 | $1/V$ |

## Table 2: System Parameters

| Parameter | Symbol | Value |
|---|---|---|
| Bandwidth | $B$ | 10 kHz |
| Received Optical Power | $P_\alpha$ | 0 dBm |
| Bias Resistance | $R_b$ | 270 $\Omega$ |
| Optical Modulation Index | $m$ | 0.27 |
| Bias Voltage | $V_{dc}$ | 0 to 4V |
| Local Oscillator Amplitude | $V_{lo}$ | 0 to 3V |
| Relative Intensity Noise Factor | $RIN$ | -150 dB/Hz |

# Appendix A

## Expression for optical power output

The optical power output $P(t)$ is given by

$$P(t) = P_0 \{1 + a_1 I + a_2 I^2 + a_3 I^3\}$$

where

$$I = m_1 \cos(\omega_1 t) + m_2 \cos(\omega_2 t)$$

The second term in Eqn. (A.1) can be expanded as follows:

$$a_2 [m_1 \cos(\omega_1 t) + m_2 \cos(\omega_2 t)]^2$$

$$= a_2 \left[ m_1^2 \cos(\omega_1 t)^2 + m_2^2 \cos(\omega_2 t)^2 + 2m_1 m_2 \cos(\omega_1 t) \cos(\omega_2 t) \right]$$

$$= a_2 \left\{ m_1^2 \left[ \frac{1 + \cos(2\omega_1 t)}{2} \right] + m_2^2 \left[ \frac{1 + \cos(2\omega_2 t)}{2} \right] + 2m_1 m_2 \left[ \frac{\cos(\omega_1 \pm \omega_2)t}{2} \right] \right\}$$

$$= a_2 \left\{ \frac{m_1^2 + m_2^2}{2} + \frac{m_1^2 \cos(2\omega_1 t) + m_2^2 \cos(2\omega_2 t)}{2} + m_1 m_2 \cos(\omega_1 + \omega_2)t \right\}$$

$$+ a_2 m_1 m_2 \cos(\omega_1 - \omega_2)t$$

Similarly, the third term in Eqn. (A.1) can be expanded as follows:

$$a_3 [m_1 \cos(\omega_1 t) + m_2 \cos(\omega_2 t)]^3$$

$$= a_3 \left[ m_1^3 \cos(\omega_1 t)^3 + m_2^3 \cos(\omega_2 t)^3 + 3m_1^2 \cos(\omega_1 t)^2 m_2 \cos(\omega_2 t) \right]$$

$$+ 3a_3 m_1 m_2^2 \cos(\omega_1 t) \cos(\omega_2 t)^2$$

$$= a_3 \left[ m_1^3 \left[ \frac{\cos(3\omega_1 t) + 3\cos(\omega_1 t)}{4} \right] + m_2^3 \left[ \frac{\cos(3\omega_2 t) + 3\cos(\omega_2 t)}{4} \right] \right]$$

$$+ \frac{3m_1^2 m_2}{4} [2\cos(\omega_2 t) + 2\cos(\omega_2 t)\cos(2\omega_1 t)]$$

$$+ \frac{3m_2^2 m_1}{4} \left[ 2\cos(\omega_1 t) + 2\cos(\omega_1 t)\cos(2\omega_2 t) \right] \Bigg]$$

$$= a_3 \Bigg[ m_1^3 \{ \frac{\cos(3\omega_1 t) + 3\cos(\omega_1 t)}{4} \} + m_2^3 \{ \frac{\cos(3\omega_2 t) + 3\cos(\omega_2 t)}{4} \}$$

$$+ \frac{3m_1^2 m_2}{2} \cos(\omega_2 t) + \frac{3m_1 m_2^2}{2} \cos(\omega_1 t) + \frac{3m_1^2 m_2}{4} \cos(2\omega_1 + \omega_2) t$$

$$+ \frac{3m_1^2 m_2}{4} \cos(2\omega_1 - \omega_2) t + \frac{3m_1 m_2^2}{4} \cos(2\omega_2 t + \omega_1) t + \frac{3m_1 m_2^2}{4} \cos(2\omega_2 - \omega_1) t \Bigg]$$

Thus the final expression for $P(t)$ is as follows:

$$P(t) = P_0 \Bigg( 1 + m_1 \cos(\omega_1 t) + m_2 \cos(\omega_2 t) + a_2 \left[ \frac{m_1^2 + m_2^2}{2} \right]$$

$$+ a_2 \left\{ \frac{m_1^2 \cos(2\omega_1 t) + m_2^2 \cos(2\omega_2 t)}{2} + m_1 m_2 \cos(\omega_1 + \omega_2) t + m_1 m_2 \cos(\omega_1 - \omega_2) t \right\}$$

$$+ a_3 \left( \frac{3 \left[ m_1^3 \cos(\omega_1 t) + m_2^3 \cos(\omega_2 t) \right]}{4} + \frac{m_1^3 \cos(3\omega_1 t) + m_2^3 \cos(3\omega_2 t)}{4} \right.$$

$$+ \frac{3}{2} m_1^2 m_2 \cos(\omega_2 t) + \frac{3}{4} m_1^2 m_2 \left[ \cos(2\omega_1 + \omega_2) t + \cos(2\omega_1 - \omega_2) t \right]$$

$$\left. + \frac{3}{2} m_2^2 m_1 \cos(\omega_1 t) + \frac{3}{4} m_2^2 m_1 \left[ \cos((2\omega_2 + \omega_1) t + \cos(2\omega_2 - \omega_1) t) \right] \right) \Bigg) \qquad \text{(A.2)}$$

Assuming identical modulation indices, $m_1 = m_2 = m$, the laser diode third-order transfer function can be obtained from Eqn. (A.2) as

$$IM_3 = 10\log \left[ \frac{<I_{im}^2>}{<I_f^2>} \right]$$

where $<I_{im}^2> = \frac{9}{32} a_3^2 P_0^2 m^6$, $<I_f^2> = \frac{1}{2} m^2 P_0^2 \left[ 1 + \frac{3}{4} a_3 m^2 \right]^2$

Thus, $IM_3$ can be simplified and expressed as $IM_3 = 10\log \left[ \frac{9 m^4 a_3^2}{16 \left( 1 + \frac{3}{4} a_3 m^2 \right)^2} \right]$

108

## Appendix B

## Expression for Responsivity $R$

The responsivity of the MSM is given by

$$R = \sum_{n=0}^{N} A_n [V_{dc} + V_{lo} \cos(\omega_{lo} t)]^n Tanh[\alpha(V_{dc} + V_{lo} \cos(\omega_{lo} t))]$$

(B.1)

The hyperbolic function *Tanh* can be assumed to be unity for analysis purposes. Let $N=3$, then the responsivity becomes: 3

$$R = A_0 + A_1 [V_{dc} + V_{lo} \cos(\omega_{lo} t)] + A_2 [V_{dc} + V_{lo} \cos(\omega_{lo} t)]^2$$
$$+ A_3 [V_{lo} + V_{lo} \cos(\omega_{lo} t)]^3$$

(B.2)

Consider the second term in Eqn. (B.2):

$$[V_{dc} + V_{lo} \cos(\omega_{lo} t)]^2$$

$$= V_{dc}^2 + 2V_{dc}V_{lo} \cos(\omega_{lo} t) + V_{lo}^2 \cos(\omega_{lo} t)^2$$

$$= V_{dc}^2 + 2V_{dc}V_{lo} \cos(\omega_{lo} t) + V_{lo}^2 \left[ \frac{1 + \cos(2\omega_{lo} t)}{2} \right]$$

$$= V_{dc}^2 + \frac{V_{lo}^2}{2} + 2V_{dc}V_{lo} \cos(\omega_{lo} t) + \frac{V_{lo}^2}{2} \cos(2(\omega_{lo} t))$$

Similarly, the third term in Eqn. (A.1) can be expanded as follows:

$$[V_{dc} + V_{lo} \cos(\omega_{lo} t)]^3$$

$$= V_{dc}^3 + 3V_{dc}^2 V_{lo} \cos(\omega_{lo} t) + 3V_{dc}V_{lo}^2 \cos(\omega_{lo} t)^2 + V_{lo}^3 \cos(\omega_{lo} t)^3$$

$$= V_{dc}^3 + 3V_{dc}^2 V_{lo} \cos{(\omega_{lo}t)} + 3V_{dc}V_{lo}^2 \left[ \frac{1 + \cos{(2(\omega_{lo}t))}}{2} \right]$$

$$+ V_{lo}^3 \left[ \frac{3\cos{(\omega_{lo}t)} + \cos{(3(\omega_{lo}t))}}{4} \right]$$

$$= V_{dc}^3 + \frac{3V_{dc}V_{lo}^2}{2} + \left( 3V_{dc}^2 V_{lo} + \frac{3V_{lo}^3}{4} \right) \cos{(\omega_{lo}t)}$$

$$+ \frac{3V_{dc}V_{lo}^2}{2} \cos{(2\omega_{lo}t)} + \frac{V_{lo}^3}{4} \cos{(3\omega_{lo}t)}$$

Thus the final expression for $R$ is as follows:

$$R = A_0 + A_1 V_{dc} + A_2 \left( V_{dc}^2 + \frac{V_{lo}^2}{2} \right) + A_3 \left( V_{dc}^3 + \frac{3V_{dc}V_{lo}^2}{2} \right)$$

$$+ \left[ A_1 V_{lo} + 2A_2 V_{dc} V_{lo} + A_3 \left( 3V_{dc}^2 V_{lo} + \frac{3V_{lo}^3}{4} \right) \right] \cos{(\omega_{lo}t)}$$

$$+ \left[ A_2 \frac{V_{lo}^2}{2} + A_3 \frac{3V_{dc}V_{lo}^2}{2} \right] \cos{(2\omega_{lo}t)} + \frac{A_3 V_{lo}^3}{4} \cos{(3\omega_{lo}t)}$$

Rearranging the above terms in order, the final expression for responsivity can be written as follows:

$$R = K_0 + K_1 \cos{(\omega_{lo}t)} + K_2 \cos{(2\omega_{lo}t)} + K_3 \cos{(3\omega_{lo}t)}$$

where the coefficients $K_n$ ($n$=0,1,2,3) are given in terms of $A_n$ ($n$=0,1,2,3) as follows:

$$K_0 = A_3 V_{dc}^3 + A_2 V_{dc}^2 + \left( A_1 + \frac{3}{2} A_3 V_{lo}^2 \right) V_{dc} + A_0 + \frac{A_2 V_{LO}^2}{2}$$

$$K_1 = 3A_3 V_{lo} V_{dc}^2 + 2A_2 V_{lo} V_{dc} + \frac{3}{4} A_3 V_{lo}^3 + A_1 V_{lo}$$

$$K_2 = \frac{3}{2} A_3 V_{lo}^2 V_{dc} + \frac{1}{2} A_2 V_{lo}^2, \quad K_3 = \frac{1}{4} A_3 V_{lo}^3$$